The Optical Polarization Variability of the Blazar PKS 2155–304

Nicolette W. Peceur
Astronomy Department
University of Cape Town

A thesis submitted for the degree of
Doctor of Philosophy

August 2023

Supervisor
Prof. R. Taylor

Co-Supervisor
Prof. R. C. Kraan-Korteweg

I, Nicolette Peceur, know the meaning of plagiarism, and declare that all of the work in the thesis, save for that which is properly acknowledged, is my own. The thesis has been submitted to the Turnitin module and I confirm that my supervisor has seen my report and any concerns revealed by such have been resolved with my supervisor.

Signature: _____ Date: _____

I confirm that I have been granted permission by the University of Cape Town's Doctoral Degrees Board to include the following publication(s) in my PhD thesis, and where co-authorships are involved, my co-authors have agreed that I may include the publication(s):

1. **N. W. Pekeur**, A. R. Taylor, S. B. Potter, R.C. Kraan-Korteweg, "Evidence for quasi-periodic oscillations in the optical polarization of the blazar PKS 2155–304", Monthly Notices of the Royal Astronomical Society: Letters, 2016 Oct Vol. 462, Issue 1, pL80–L83

2. **N. W. Peceur**, A. R. Taylor, R. C. Kraan-Korteweg, "The optical polarization of the blazar PKS 2155–304 during an optical flare in 2010", Monthly Notices of the Royal Astronomical Society, 2020 Jun Vol. 495, Issue 2, p2162–2169

3. **N. W. Peceur**, A. R. Taylor, R. C. Kraan-Korteweg, "A multiwavelength view of the long-term behaviour of PKS 2155–304", In preparation.

Signature: Signed by candidate Date: 01-12-2023

Student Name: Nicolette Peceur Student Number: PKRNIC001

For my grandfather,
Nicholas Jacobus Peceur
1937 – 2010

"If you can't run, you walk, and if you can't walk, you crawl, and if you can't do that... you find someone to carry you."

— The Message, Firefly

Acknowledgements

I would like to express my deepest gratitude to the following individuals and organizations who have contributed to the completion of my doctoral journey:

My Supervisors, Prof. Russ Taylor and Prof. Renée Kraan-Korteweg, for their unwavering support, guidance, and invaluable expertise throughout the entire research process. Thank you for your insightful feedback, constructive criticism, and thoughtful suggestions. Your mentorship and encouragement have been instrumental in shaping the direction of my work and enhancing my research skills. Your expertise and commitment to academic excellence have significantly enriched the quality of this thesis. Furthermore, thank you for your understanding and support through the more difficult times of this journey.

I extend my sincere appreciation to Dr. Stephen Potter, Prof. Paula Chadwick, Dr. Michael Daniel, Prof. Markus Botccher and the late Prof. Okkie de Jager who provided their expertise and guidance and contributed their insights to my research study. Their willingness to share their knowledge and experiences have been invaluable.

I am grateful to the faculty members and researchers at the Astronomy department at the University of Cape Town (UCT), the South African Astronomical Observatory (SAAO), the Physics Department at Durham University (DU) and the Centre for Space Research at North West University (NWU) for creating a stimulating intellectual environment. Their passion for knowledge and their dedication to advancing research in the field have been a constant source of inspiration.

My colleagues and fellow graduate students, especially Narges Hatamkhani, for their camaraderie, discussions, and support throughout this challenging journey. Our collaborations, exchange of ideas, and shared experiences have played a crucial role in shaping my research and personal growth.

I am grateful to the UCT Science Faculty, the Inter-university Institute for Data Intensive Astronomy and the Centre for Space Research (NWU) for their financial support, which enabled me to pursue my doctoral studies. Their investment in my research has been instrumental in realizing the goals of this thesis.

My family and friends, especially my husband Albert, for their unwavering love, encouragement, and belief in my abilities. Their continuous support, patience, and understanding have been the pillars of strength that carried me through the challenges of this academic endeavor.

Lastly, I would like to express my heartfelt gratitude to all those individuals who, in one way or another, have provided assistance, encouragement, and motivation during this journey. Your contributions, no matter how small, have made a significant impact on my research and personal development.

Abstract

Blazars are some of the most energetic and variable objects in the universe. Blazar emission has been detected across the electromagnetic spectrum and exhibits variability on a wide range of timescales, from minutes to years. The observed emission is Doppler boosted and dominated by non-thermal radiation driven by the magnetic field of a relativistic jet. PKS 2155–304 is an archetypal blazar, located in the southern hemisphere. The source is bright and highly variable, displaying both active and quiescent states. In this thesis I make use of optical polarization and multiwavelength observations across roughly 5.5 years to probe the source variability on short (intra-day to daily), intermediate (days to months) and long timescales (months to years). The polarization, as a direct observable of the jet's magnetic field, can help gain insight into the physical processes that underlie the observed emission, while contemporaneous multiwavelength observations can assist in distinguishing between different emission models.

I investigated the short term variability of PKS 2155–304 by using optical polarization measurements recorded over a 3 day period during a period of enhanced gamma-ray activity. The observations revealed, for the first time, evidence of quasi-periodic oscillations in the optical polarization of a blazar. A periodogram analysis of the polarized flux revealed the existence of two periodic components at ~ 13 minutes and ~ 30 minutes. The oscillations can be explained by turbulence behind a relativistic shock traversing a jet containing quasi-helical structures in magnetic field or electron density.

To study the intermediate timescale brightness variations of the source I analysed its optical polarization and $BVRJ$ multiband light curves during a prominent optical flare in 2010. The flare evolved over roughly 4 months with a flux doubling time of ~ 11 days. A comparison of the polarization angle and photometric flux revealed the existence of two distinct states at low and high flux. Below 18 mJy, no clear relationship is seen between the polarization angle and flux, while there is a positive correlation above 18 mJy. I performed a photopolarimetric analysis of the high flux state, which showed that it can be attributed to a variable component with a power-law radiation spectrum of index -1.12 and a polarization degree of 13.3%. I then applied a shock-in-jet model to the observations, which showed that the observed variability can be attributed to a nearly edge-on shock. Within the

shock-in-jet model, I derived estimates for the magnetic field (0.06 G), Doppler factor (22.3) and viewing angle of the jet (2.6°).

Lastly, I performed an investigation of the long term variability of the blazar by analysing roughly 5.5 years of radio, optical, optical polarization, $X-$ray and $\gamma-$ray measurements. Using a correlation analysis, I found that the optical, $X-$ray and high energy light curves were consistent with zero lag, while the radio light curve lagged behind the higher energy emission by $\sim$ 46 days. The lag between the radio and higher energy light curves is consistent with opacity effects due to synchrotron emission. The nearly zero lag between the synchrotron (optical and $X-$ray) and Inverse Compton (high energy) emission components indicates that the same electron population is responsible for the emission. When computing the temporal structure functions of the multiband light curves, I found that the multiwavelength emission can be described by a power-law spectral density function, with an index of –1.5 for the radio, –1.3 for the optical, –0.6 for $X-$rays and –1.0 at high energies. A break timescale is present for the optical and $X-$ray band, below which the structure function is characterised by white noise. The structure functions also indicate the existence of periodic outbursts roughly every 1.8 years. My analysis of the multiband photometric fluxes showed that the optical emission is well-described by a variable component with a power-law radiation spectrum of index -1.13, consistent with synchrotron emission. For a power law electron distribution, the optically thin synchrotron emission implies an energy spectrum with an index of -3.26 for the electrons. Finally, the long term optical polarization supports the existence of a constant polarization component with a polarization degree of 3.4% and a polarization angle of 76°.

The results of my analysis indicate that the emission from PKS 2155–304 is composed of two components, a persistent component with low polarization degree and a magnetic field that lies roughly parallel to the direction of the jet, and a variable component with a constant power-law radiation spectral index and high polarization degree. The variable emission component is consistent with a relativistic shock propagating in the jet on timescales from day to months, where intraday quasi-periodic oscillations can arise due to turbulence behind the shock. The structure function analysis of the long term behaviour indicates that there is power in the variable component on all time scales down to the break in white noise. However, the variable component undergoes major outbursts roughly every 1.8 years. The constant power-law observed for the variable emission over roughly 5.5 years means that the particles have the same energetics. The nearly zero lag across the different energy bands indicates that the same particle population underlies the low and high energy emission, consistent with Synchrotron Self Compton models.

Contents

List of Figures

1 Introduction

PKS 2155–304 is a nearby, bright southern blazar of the BL Lac class. Blazars are some of the most energetic active galactic nuclei (AGN). As is typical for these objects, PKS 2155–304 is known to be highly variable, exhibiting both active and quiescent states. Most notable is the detection of two exceptional gamma-ray flares by the High Energy Stereoscopic System on timescales of just a few minutes. With its extreme properties, PKS 2155–304 is an ideal candidate to study blazars in more detail to understand the physical processes that result in these extreme properties. In this thesis I make use of optical polarization and multiwavelength observations spanning roughly 5.5 years to probe the source variability on a variety of timescales in an effort to learn about the source physics.

In the first chapter, I will present an overview of the blazar object group, including its parent class. I will describe the radiation mechanisms believed to dominate the jets of these objects and the emission models that are currently favoured. A historical overview of the blazar PKS 2155–304 is presented followed by a description of the work put forward in this thesis.

1.1 Active Galactic Nuclei

The object of this study, PKS 2155–304, belongs to a class of extragalactic objects known as active galactic nuclei. Active galactic nuclei or AGN are the compact and highly luminous cores of otherwise normal galaxies and are among the brightest sources in the universe. AGN emission has been detected across the entire electromagnetic spectrum and is believed to be driven by the accretion of matter onto a supermassive black hole located at the center of the host galaxy.

Within the model of AGN unification proposed by Urry & Padovani (1995a) an AGN consists of:

i. a *Supermassive Black Hole (SMBH)* of mass $10^6 - 10^{10} M_\odot$, forming the central engine, where $M_\odot$ symbolizes one solar mass.

ii. an *Accretion Disk*, extending out to 1 pc from the central engine. The accretion disk has a thermal energy spectrum, with the emission peaking at far ultraviolet frequencies.

iii. the *Broad Line Region (BLR)*, which comprises small, dense, high velocity gas clouds excited by the radiation from the accretion disk and orbiting the central engine at speeds $\sim 10^4$ km s^{-1}.

iv. a *Torus* of obscuring material located beyond the BLR, extending up to 100 pc from the central engine and accretion disk. The torus absorbs the emission from the central region and re-emits the energy at infrared frequencies.

v. the *Narrow Line Region (NLR)*, which comprises lower velocity ($< 10^3$ km s^{-1}) and lower density gas clouds, located outside the torus.

vi. a *Jet* composed of a collimated relativistic outflow of particles flowing from the central engine, generally oriented perpendicular to the accretion disk.

An illustration of the physical attributes of AGN within this framework is presented in Fig. 1.1.

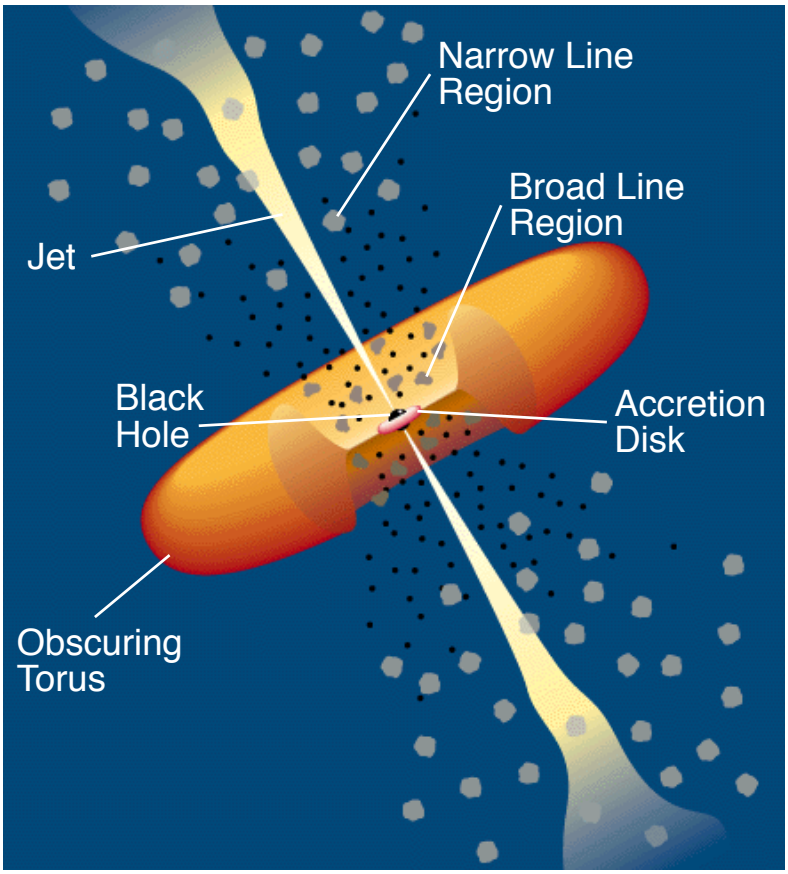

Figure 1.1: Schematic of the components of an active galactic nucleus (AGN) from Urry & Padovani 1995a.

1.2 Blazars

Since AGN are not isotropic, the observed properties vary with the viewing angle of the observer. Radio emission is detected in roughly 15–20% of AGN (Abdo et al., 2010; Kellermann et al., 2016). An AGN can be classified as radio-loud (*Radio-loud Quasars*, *Radio Galaxies* and *Blazars*) or radio-quiet (*Seyfert Galaxies* and *Radio-quiet Quasars*) based on the ratio of the radio luminosity to the optical luminosity (Kellermann et al., 1989, 2016). Blazars are typically a subset of radio-loud AGN where the relativistic jet is directed close towards the observer's line-of-sight, resulting in strong Doppler boosting of the jet radiation. The observed emission is thus dominated by the jet and is characterised by intense and rapid variability across the electromagnetic spectrum, as well as the detection of polarization at radio and optical wavelengths. Historically, blazars have been further grouped as

either BL Lacertae objects (BL Lacs) or flat spectrum radio quasars (FSRQs) based on the characteristics of their optical spectra. FSRQs are brighter, characterised by broad emission lines at optical wavelengths (from which the redshift can be determined) and are found at larger redshifts than BL Lacs (Fossati et al., 1998). BL Lacs, in contrast, are found at much lower redshifts (typically a redshift $z \leq 1$), generally do not exhibit emission lines and are less luminous. The optical continuum emission of blazars is featureless, while the broadband spectral energy distribution (SED) is characterized by the presence of two broad peaks. The low-energy peak is located at optical/UV– to soft X-ray energies, while the high–energy peak is located at hard X–ray to $\gamma-$ray energies. The continuum emission of blazars is non-thermal in nature and is attributed to the interaction of energetic particles in the jet with magnetic fields, photon fields and the ambient medium of the AGN. An example of the SED of PKS 2155–304 is shown in Fig. 1.2.

BL Lacs and FSRQs are further divided based on the location of the first broad feature's (synchrotron peak) peak frequency ($\nu_{\rm sy}$) (Abdo et al., 2010). The classification scheme divides blazars into three sub-classes: high-energy peaked blazars (HBLs; $\nu_{\rm sy} > 10^{15}$ Hz), intermediate-energy peaked blazars (IBLs; $10^{14} < \nu_{\rm sy} < 10^{15}$ Hz), and low-energy peaked blazars (LBLs; $\nu_{\rm sy} < 10^{14}$ Hz). BL Lac objects display all three characteristic behaviors, whereas FSRQs predominantly belong to the LBL sub-category.

The jets of blazars are made up of collimated outflows of plasma travelling at relativistic speeds that transport energy, momentum and angular momentum from the central black hole to distances located up to one Megaparsec or more away (Rees, 1971; Blandford & Rees, 1974). How the jet is created, the physical make-up of the jet plasma and the mechanisms behind its acceleration and collimation over such large distances is not yet certain. However, it is generally believed that jets are formed as a result of rotating plasma in the accretion disk creating a poloidal magnetic field. This forces the plasma above and below the accretion disk to co-rotate with it (e.g., McKinney 2006; Meier et al. 2001). The particles are accelerated outwards if one of the components of the centrifugal force is aligned with the direction of the

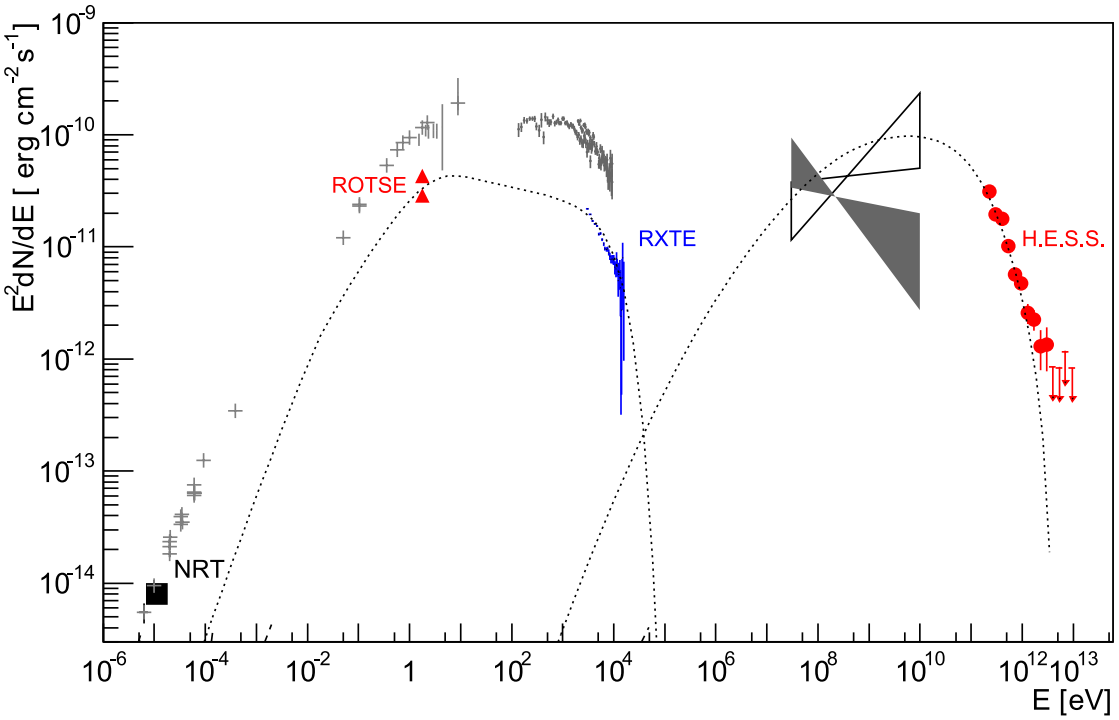

Figure 1.2: Average SED of PKS 2155–304 during a multi-wavelength campaign from Oct. to Nov. 2003 (H.E.S.S. Collaboration et al., 2005a). The measurements were performed by the Rossi X-ray Timing Explorer (RXTE) $X-$ray satellite (blue), the Robotic Optical Transient Search Experiment (ROTSE) optical telescope (red triangles), the Nancay radio telescope (NRT, black square) and the very high energy (VHE) telescope H.E.S.S. (High Energy Stereoscopic System, red circles). Non simultaneous data are given by the grey symbols. Equal y-values denote equal energy output per decade of energy. The energy is given on the x-axis. The dotted line represents the Synchrotron Self-Compton model described in H.E.S.S. Collaboration et al. 2005b.

magnetic field lines. The twisted magnetic field propagates outward as Poynting flux in the polar directions, eventually becoming a jet that consists of a focused relativistic plasma flow (e.g., Vlahakis & Königl 2004; Meier & Nakamura 2006). Within this region, the magnetic field should retain a helical pattern. Beyond the acceleration and collimation zone, the magnetic field may become turbulent.

High-resolution radio images have shown that blazar jets are inhomogeneous and are made up of denser areas known as knots. These knots propagate in the jet at apparent speeds exceeding the speed of light (Piner & Edwards, 2004; Giroletti et al., 2004), in a process known as superluminal motion. Since blazars are viewed looking almost straight down the AGN jet toward the central engine they present a unique geometric perspective: Doppler boosting greatly enhances

the observed intensity of the jet emission and the observed variability on short and long time scales means that regions on a range of physical scales, down to the core of the jet, can be probed. Therefore, blazars, with their extreme observational properties, present an opportunity to learn about AGN emission mechanisms under the most extreme physical conditions.

1.3 Radiation mechanisms

The emission processes of blazars are dominated by the magnetic field of the jet. The photon production mechanisms believed to be responsible for the observed emission are described below. For a comprehensive discussion of the non-thermal emission processes in relativistic AGN jets please refer to Chapter 3 in Böttcher et al. 2012 and references therein.

1.3.1 Synchrotron radiation

Synchrotron radiation is emitted when a charged particle of mass m, charge q and energy $E = \gamma mc^2$, is accelerated at relativistic speed $v = \beta c$ in an ordered magnetic field of strength B. The velocity of the particle consists of a constant component in the direction of the magnetic field and circular motion, with gyration frequency $\nu_g = \dfrac{qB}{2\pi m}$, around the magnetic field line. The particle therefore moves along a spiral path with constant pitch angle ψ. The effect of moving relativistically results in the emitted light being beamed into a narrow cone of angle $\dfrac{1}{\gamma}$ in the direction of the particle's motion, where $\gamma = \dfrac{1}{\sqrt{1-\beta^2}}$ is the Lorentz factor, while the gyration frequency increases by a factor γ^2, yielding $\nu_c = \gamma^2 \nu_g$ in the co-moving frame of the particle, where ν_c is known as the critical frequency.

The total energy lost by the particle due to synchrotron radiation is:

$$\frac{dE}{dt} = -\frac{16\pi c}{3}\left(\frac{q^2}{mc^2}\right)^2 u_B \beta^2 \gamma^2 \sin^2\psi, \tag{1.1}$$

where $u_B = B^2/(8\pi)$ is the energy density in the magnetic field. For particles with an isotropic distribution of pitch angles, the mean energy loss rate is:

$$\frac{dE}{dt} = -\frac{32\pi c}{9}\left(\frac{q^2}{mc^2}\right)^2 u_B \beta^2 \gamma^2. \tag{1.2}$$

Equation 1.2 demonstrates that for a given charge synchrotron emission is more efficient for lighter particles e.g, electrons are more efficient at radiating synchrotron emission than protons.

The cooling time of particles emitting synchrotron radiation is:

$$t_{\rm sync} = \frac{E}{dE/dt} = -\frac{9}{32\pi c}\left(\frac{m^4 c^6}{q^4}\right)\frac{1}{u_B \beta^2 E}. \tag{1.3}$$

More energetic particles have shorter synchrotron lifetimes.

Polarization

Synchrotron radiation is linearly polarized for aligned magnetic fields. The polarization degree p is defined as:

$$p = \frac{I_\perp - I_\parallel}{I_\perp + I_\parallel}, \tag{1.4}$$

where $I_\perp$ and $I_\parallel$ is the power emitted orthogonal and parallel to the instantaneous direction of motion of the particle. The polarization angle, θ, is defined by the position angle of the electric field vector and is orthogonal to the direction of the magnetic field. The polarization therefore serves as a direct measure of the magnetic field structure in the emission region.

1.3.2 Inverse-Compton radiation

Inverse-Compton radiation is the increase in energy of low energy photons by interacting with high energy electrons through Compton scattering. The likelihood and strength of this interaction is determined by the Klein-Nishina cross-section:

$$\sigma_{\rm KN} = \frac{3}{8}\sigma_T \frac{1}{x}\left[\frac{1}{2} + \frac{4}{x} - \frac{1}{2(2x+1)^2} + \left(1 - \frac{2(x+1)}{x^2}\right)\ln(2x+1)\right], \tag{1.5}$$

where $x = \frac{h\nu}{m_e c^2}$ is the photon energy in the rest frame of the electron, in units of the electron rest mass energy and $\sigma_T = \frac{8\pi}{3}\left(\frac{e^2}{4\pi\epsilon_0 m_e c^2}\right)^2$ is the Thomson cross-section, with e and m_e the charge and mass of the electron, respectively. For $x \ll 1$, the Klein-Nishina cross-section approaches the Thomson value, while for $x \gg 1$, the cross-section decreases as $\sigma_{\rm KN} \sim \frac{1}{x}$.

The energy loss rate of a relativistic electron moving with momentum p in an isotropic radiation field with energy density $u_{\rm ph}$ in the Thomson regime is:

$$\frac{dE}{dt} = \frac{4}{3} c \sigma_T u_{\rm ph} \left(\frac{p}{m_e c}\right)^2, \tag{1.6}$$

yielding a cooling time:

$$t_{\rm IC} = \frac{3}{4 c \sigma_T u_{\rm ph}} \frac{m_e^2 c^2}{E}. \tag{1.7}$$

Therefore, similarly to synchrotron cooling, more energetic electrons cool faster. In the Klein-Nishina regime, the energy loss rate of the electrons increases logarithmically with electron energy, resulting in an approximately linear increase of the cooling time with energy (see Chapter 3 in Aharonian 2004).

1.3.3 Pion decay

Neutral pions are created when relativistic protons interact with either ambient protons or ambient photons.

$$\begin{aligned} p + p &\rightarrow \pi^{0,\pm} + 2N \\ p + \gamma &\rightarrow p + \pi^0 \end{aligned} \tag{1.8}$$

After a mean life time of 10^{-16} s, the decay of neutral pions results in the emission of two $\gamma-$ray s of energy 70 MeV in the rest frame of the particle:

$$\pi^0 \rightarrow 2\gamma + e^+ + e^- \tag{1.9}$$

1.3.4 Pair production

Pair production occurs when a very high energy photon interacts with a low energy photon, resulting in their annihilation and the creation of an electron-positron pair:

$$\gamma\gamma \rightarrow e^{+}e^{-} \tag{1.10}$$

Pair production is extensive at the location of VHE emission when the ambient photon fields are dense. This mechanism is also responsible for gamma-rays being absorbed by the Extragalactic Background Light.

1.4 Emission models

As shown in Fig. 1.2 the spectral energy distribution of blazars consists of two broad peaks and is modelled by injecting relativistic particles into an emission region. Particles inside the emission region interact through the photon production mechanisms described in the previous Section (1.3). At high energies, a distinction between *Leptonic* and *Hadronic* models is made, determined by the nature of the radiating particles.

1.4.1 Leptonic

In leptonic models, electrons are accelerated by magnetic fields inside the emission zone. The synchrotron emitting electrons give rise to the low-energy peak in the SED, while Inverse Compton emission from the same particle population produce the high-energy SED component. The seed photons for the Inverse Compton scattering process can either originate from synchrotron emission from the same electron population, known as *Synchrotron Self-Compton* (SSC) emission, or from external photon fields (*External Compton*, EC emission). Photons originating from outside of the emission region can come from, for example, the accretion disk (Sikora et al., 1994), Broad Line Region (Ghisellini & Madau, 1996) or obscuring torus (Sikora et al., 2002) of the AGN, or be produced in different regions within the blazar jet (Ghisellini et al., 2005). Since the same particle population underlies

both the synchrotron and inverse Compton processes (SSC and EC), correlations between the low and high energy emission components of the SED are expected.

1.4.2 Hadronic

In hadronic models, the high-energy peak of the blazar SED is identified with the emission of very high energy protons. For highly magnetized regions ($B \sim 30\text{G}-100$ G, Aharonian 2000; Mücke & Protheroe 2001a; Mücke et al. 2003), direct production of gamma-rays through proton synchrotron emission is possible. Secondary gamma-rays can be produced through pion decay (Pohl & Schlickeiser, 2000; Mannheim, 1993). Similar to leptonic models, the low energy peak of the SED is a product of synchrotron emission from relativistic electrons. The electron population is either accelerated in conjunction with the protons that produce the high energy SED peak, or generated as secondary particles when the VHE protons interact via pion decay. The synchrotron emission component is therefore related to the protons responsible for the high-energy emission. Hence, correlations between the low- and high-energy emission are predicted for hadronic models as well. Nevertheless, leptonic blazar emission models are generally favoured, as both the synchrotron and Inverse Compton mechanisms are suppressed for protons. The less massive electrons are also associated with faster acceleration and cooling times, which is more compatible with the variability timescales seen during blazar flares (Aharonian, 2000). For the case of the IceCube neutrino event coincident with the flaring blazar TXS 0506+056, a physically consistent picture is only achievable through a hybrid lepto-hadronic scenario, where the γ–rays are produced by external inverse-Compton processes and the high-energy neutrinos through a radiatively subdominant hadronic component (Keivani et al., 2018).

1.5 Blazar properties

Blazars are known for displaying significant variability throughout the entire electromagnetic spectrum, spanning time scales that range from minutes to years (Böttcher & Reimer, 2004; Albert et al., 2007; Arlen et al., 2013; Kaur et al., 2017;

Abdalla et al., 2019; Kamaram et al., 2023; Roy et al., 2023). Light curves spanning from radio frequencies to gamma-rays can display intricate characteristics, exhibiting a number of flares and subflares, as well as states of low activity (Krawczynski et al., 2004; Raiteri et al., 2006; H. E. S. S. Collaboration et al., 2011; Chatterjee et al., 2012; Carnerero et al., 2015; Prince et al., 2022). Variability in blazars belongs to three broad categories: variations occurring on timescales of less than a day to a few days are referred to as intranight or intraday to short term variations (e.g., Rector & Perlman 2003; Albert et al. 2007; Kaur et al. 2017; Fang et al. 2022)[1]; variations occurring on timescales of a few days to months are defined as short-term to intermediate variability; and variations occurring on timescales of a few months to years are known as long-term variability (e.g., Raiteri et al. 2005, 2006; Andruchow et al. 2011; Gupta et al. 2017).

Searches for flux correlations between different energy bands demonstrate inconsistent behaviour. Correlated variability has been observed in some blazars (e.g., Aleksić et al. 2015b; Sandrinelli et al. 2017; Prince et al. 2021; Zhang et al. 2021; MAGIC Collaboration et al. 2023), while uncorrelated variability has also been observed (e.g., Acciari et al. 2011a; Aleksić et al. 2015a; Siejkowski & Wierzcholska 2017; MAGIC Collaboration et al. 2020a). The lack of correlated variability and the existence of so-called orphan flares (where there is no counterpart at other wavelengths) (Krawczynski et al., 2004; Błażejowski et al., 2005) are all challenges for blazar emission models.

Evidence for the existence of periodic flux variations have been observed and confirmed for at least one blazar, OJ287 (Sillanpaa et al., 1988; Kidger et al., 1992; Sillanpaa et al., 1996; Valtonen et al., 2006). The periodicity is thought to be due to binary supermassive black holes at the centre of the AGN. The periodic or quasi-periodic oscillations of the blazar's emission is attributed to the orbital movement and Lense-Thirring precession of the dominant accretion disk or the jet (Dey et al., 2019). However, in their study, Covino et al. 2019 did not find conclusive evidence of periodicities in any of the 10 blazars they examined.

[1]For short term radio variations, interstellar scintillation may contribute to the variability (Koay et al., 2019).

Observational studies of polarization in blazars have revealed several important characteristics that provide insights into the physics of these objects, including: a high polarization degree that can be more than 30 per cent (e.g. Patiño-Álvarez et al. 2018; Singh et al. 2020), which is indicative of a strong and ordered magnetic field in the blazar jet; highly variable polarization, especially during flaring periods (e.g. Ikejiri et al. 2011; Fraija et al. 2017; Rajput et al. 2022) and large rotations of the polarization angle (Marscher et al., 2010; Larionov et al., 2013; Blinov et al., 2015, 2018), which was attributed to motion along spiral paths. When examining the relationship between the polarization and total flux, no consistent correlated behaviour has been observed. Studies have shown both correlated, anti-correlated and uncorrelated behaviour between the total flux and the polarization degree (e.g. Hagen-Thorn et al. 2002; Hagen-Thorn et al. 2008; Sorcia et al. 2013; Gaur et al. 2014; Rajput et al. 2019; Pasierb et al. 2020; Pandey et al. 2022).

The spectral energy distribution models of blazars aim to describe the observed emission across the electromagnetic spectrum, from radio waves to gamma-rays. Blazars are classified into FSRQs and BL Lacs, and their SED models reflect their distinct properties. The SED models for FSRQs can involve external Compton emission from the accretion disk and broad line region (e.g. Böttcher et al. 2007; Sahayanathan & Godambe 2012; Schutte et al. 2022), while for BL Lacs synchrotron self Compton emission provides a successful model in many cases (e.g. Acciari et al. 2011b; Aleksić et al. 2012, 2015a; Ahnen et al. 2017; Priya et al. 2022).

While one-zone SSC models have proven effective in reproducing the spectral energy distributions of blazars, they may not consistently account for the observed SEDs during flaring events, or for FSRQs and low energy peaked BL Lacs (Abdo et al., 2010). More complicated models incorporating several SSC components, external Compton emission or hadronic processes are necessary to explain the SEDs of these objects (e.g. Böttcher et al. 2013; Aleksić et al. 2015d; Kushwaha et al. 2018; MAGIC Collaboration et al. 2020b, 2023).

Comprehensive multiwavelength studies on a substantial number of blazars are essential to achieve a thorough understanding of blazar emission processes, as

highlighted by the observational characteristics of these objects. Here, we begin by focusing on the study of a single prototypical blazar, which demonstrates all properties of the blazar class.

1.6 The blazar PKS 2155–304

PKS 2155–304 is a nearby, bright southern blazar. PKS 2155–304 is a typical blazar, displaying intense and rapid variability across its broadband emission and polarized emission at radio and optical wavelengths. The source was discovered as one of the brightest extragalactic $X-$ray sources in the sky in 1979 by the HEOA $X-$ray telescope. Since its discovery the source has been extensively monitored across the whole electromagnetic spectrum (Smith et al., 1992; Urry et al., 1993; H.E.S.S. Collaboration et al., 2005a; Foschini et al., 2008; H.E.S.S. Collaboration et al., 2012, 2014; Abdalla et al., 2020) and followed by numerous long term monitoring campaigns e.g., the Fermi Gamma-ray Space Telescope, the Swift X–ray telescope, the Small and Moderate Aperture Research Telescope System and the F-GAMMA radio observation programme. Monitoring of the blazar revealed that it exhibits both active and quiescent states. The H.E.S.S. telescope recorded two exceptional gamma-ray flares in July and August 2006, when the source displayed a VHE flux 10 times the average, with brightness variations occurring on a timescale of just a few minutes (H.E.S.S. Collaboration et al., 2007).

Simultaneous observations from optical to TeV energies during a quiescent state have shown that the time-averaged spectral energy distribution of the source can be described by a one-zone SSC model (H.E.S.S. Collaboration et al., 2009b), while simultaneous optical, $X-$ray and very high energy observations of the SED during the high state in 2006 showed that a multizone SSC model was needed to explain the emission during the active state (H.E.S.S. Collaboration et al., 2009a). In contrast, long-term observations of the source emission which include low and high states showed that the SED is well described by one-zone SSC emission models (Chevalier et al., 2019; Rajput et al., 2021).

A search for correlated flux variability resulted in the observation of a relationship between the optical and VHE flux during the low state in 2008 (H.E.S.S. Collaboration et al., 2009b). Strongly correlated behaviour between the $X-$ray and VHE flux was detected during the second exceptional VHE flare in 2006 (H.E.S.S. Collaboration et al., 2009a). A correlated UV, optical, $X-$ray and gamma-ray flare was also seen in 2015, while an orphan optical/UV flare was observed in 2016 (Wierzcholska et al., 2019). Long-term multiwavelength light curves of the source revealed correlated flux variations in the IR, optical, and high energy (HE) gamma-ray band (Rajput et al., 2021).

Light curve variations are characterised by a power-law power spectral density function on timescales ranging from days to over ten years (Kastendieck et al., 2011; H.E.S.S. Collaboration et al., 2017). At optical bands the variability power follows a power law above a break frequency and white noise below it. Periodic variability has also been observed for PKS 2155–304. Long time-scale periodic amplitude variations have been reported with cycles of 4 and 7 yrs (Fan & Lin, 2000) and 315 d (Sandrinelli et al., 2014), while a ~ 4.6 h periodicity was detected at X-ray energies (Lachowicz et al., 2009). At high energies, a quasi-periodic oscillation (QPO) of 1.74 yrs has been reported (Zhang et al., 2017). However, recent studies found no firm evidence for year-long QPOs at gamma-ray and optical energies (Covino et al., 2020; Ait Benkhali et al., 2020).

The only direct means of imaging the parsec scale morphology of blazars is through radio imaging with Very Long Baseline Interferometry. Multi-epoch radio images of PKS 2155–304 mapped with the Very Long Baseline Array (Piner & Edwards, 2004; Piner et al., 2008, 2010) revealed the presence of a compact jet component located to the southeast of the radio core at a position angle from $150°-160°$. Linearly polarized radio emission, corresponding to a polarization degree between 3% and 8%, was detected from the core with polarization angle of 131°.

Although radio imaging can provide a direct means of viewing blazar jets, the optical polarization serves as a tool to investigate the magnetic field of the jet on timescales relevant to the high energy emission. Historically, the optical polarization

of PKS 2155–304 varies between 2% and 8% , while the polarization angle was found to vary between 100° and 140° (Tommasi et al., 2001; Dominici et al., 2008; Barres de Almeida et al., 2010). However, a study of the optical polarization variability spanning 25 years found a systematic decrease for the polarization angle over a timescale of $\gtrsim$10 years, which might indicate global geometric changes in the direction of the relativistic jet. The study also detected variations in the polarized flux on timescales ranging from a few minutes to a few years. Past studies have also shown that the optical polarization changes more rapidly than the total brightness, on timescales similar to the higher energy emission. While contemporaneous photometric and polarimetric observations generally show no correlation between the polarized flux and the total flux, large changes in the polarization degree appear to correlate with epochs of high total flux (Dominici et al., 2008). A study of the polarization during 6 days of observation in September 2008, when the source was in a low state, showed that it can be described by a two component model consisting of a constant and variable polarization component (Barres de Almeida et al., 2010). The constant component was identified with a polarization degree of 4% and a polarization angle of 130°.

1.7 This thesis

While the generally accepted picture of blazar emission involves the injection of relativistic particles into an emission region with a magnetic field, a consistent physical model for the quiescent and active emission has not yet emerged. For example, there is no consensus on the number of SSC emitting regions required to explain the quiescent or active emission. The criteria differentiating the quiescent or active emission is also not well defined.

PKS 2155–304 is known to be variable across a large range of wavelengths and timescales, with the blazar being one of the few blazars for which periodic behaviour has been reported. However, there is currently no coherent physical interpretation connecting these behaviours.

In recent years, there have been many multiwavelength observation campaigns tracking the variable emission of PKS 2155–304 on long term basis. Much of the data is publicly available and this thesis is motivated by the availability of such a comprehensive multiwavelength data set that also includes polarization. This is because the polarization is a direct probe of the jet's magnetic field and geometry, the driver of the observed emission, and can help gain valuable insight into the emission region. The goal of this work is to present a side by side analysis of the multi-wavelength and polarization data and to use the polarimetry to constrain or model the physical mechanisms responsible for the variable and quiescent emission in order to put together as comprehensive a picture of the source as possible. This is achieved by investigating contemporaneous radio, optical photometric and polarimetric, X–ray, HE gamma-ray and VHE gamma-ray observations between 2009 and 2014 on a variety of timescales, from minutes to years. This unprecedented polarization and multiwavelength coverage of PKS 2155–304 across so many years allows me to investigate the variability, emission properties and magnetic field structure of the source in a comprehensive way. By analysing the source variability on short (intra-day to daily), intermediate (days to months) and long timescales (months to years) and combining my findings, I hope to build a holistic view of the blazar.

This thesis is organised as follows: in Chapter 2, I present a study of the short term variability of the optical polarization of PKS 2155–304 during a period of increased gamma-ray activity. This is done to investigate any possible link between the polarization and the gamma-ray state and to investigate the nature of the polarization variations during a high gamma-ray state.

The intermediate photo-polarimetric variability is put forward in Chapter 3. In this chapter I present an analysis of the optical polarization and $BVRJ$ multiband light curves of PKS 2155–304 during a prominent optical flare in 2010. The photopolarimetric variability during this high optical state is modelled in order to learn about the source and characteristics of the variable emission.

The long term variability of the optical polarization and multiwavelength emission of the blazar is presented in Chapter 4, where I compile radio, optical,

optical polarization, $X-$ray and $\gamma-$ray measurements of PKS 2155–304 spanning roughly 5.5 years. I examine the characteristics of the variable emission and probe the relationship between the low and high energy emission. Lastly, I use the polarization measurements to discover if a stable polarization component exists for the blazar.

Finally, in Chapter 5 I present a summary of my results and a conclusion which attempts to synthesize the results of this work into a physical picture of the source. Suggestions for future work are presented in the final chapter.

2

Evidence for quasi-periodic oscillations in the optical polarization of the blazar PKS 2155–304

N. W. Pekeur[1], A. R. Taylor[1,2], S. B. Potter[3] and R. C. Kraan-Korteweg[1]

[1]Astrophysics, Cosmology and Gravity Centre, Department of Astronomy, University of Cape Town, Private Bag X3, Rondebosch 7701, SA

[2]Department of Physics and Astronomy, University of the Western Cape, Modderdam Road, Private Bag X17, Belville 7530, SA

[3]South African Astronomical Observatory, PO Box 9, Observatory 7935, Cape Town, SA

Abstract

Evidence for the presence of quasi-periodic oscillations (QPOs) in the optical polarization of the blazar PKS 2155–304, during a period of enhanced gamma-ray brightness, is presented. The periodogram of the polarized flux revealed the existence of a prominent peak at $T \sim 13$ min, detected at $> 99.7\%$ significance, and $T \sim 30$ min, which was nominally significant at $> 99\%$. This is the first evidence of QPOs in the polarization of an active galactic nucleus, potentially opening up a new avenue of studying this phenomenon.

2.1 Introduction

PKS 2155–304 is a blazar, a subclass of radio-loud active galactic nucleus (AGN) for which the relativistic jet is oriented close to the line-of-sight of the observer (Urry & Padovani, 1995b). Active galactic nuclei are powered by accretion of matter onto a $10^6 - 10^9 M_\odot$ supermassive black hole (SMBH). The observed emission is dominated by the jet and is characterized by intense and rapid brightness fluctuations across the electromagnetic spectrum, and the presence of polarization at optical to radio wavelengths. PKS 2155–304 exhibits significant variability on timescales ranging from minutes (H.E.S.S. Collaboration et al., 2007) to years (Fan & Lin, 2000; Kastendieck et al., 2011). Short timescale variations, from minutes to hours, probe emission regions with sizes comparable to the gravitational radius of the central SMBH, while variations on timescales of months to years probe the jet structure. The timing signatures indicate that the emission is governed by correlated noise processes (Vaughan et al., 2003; Edelson & Nandra, 1999; Vaughan, 2005; Chatterjee et al., 2008, 2012; Kastendieck et al., 2011), possibly originating from instabilities in the accretion rate and jet.

Quasi-periodic variations have been reported for a small number of AGN. The clearest detection is a ~ 1 hour QPO in the $X-$ray light curve of the radio-quiet Seyfert galaxy RE J1034+396 (Gierliński et al., 2008). PKS 2155–304 is one of only a few blazars for which convincing evidence of quasi-periodic brightness variations have been documented. Long time-scale periodicities were discovered in the optical light curve of the source. Amplitude modulations with periods of 4 and 7 years (Fan & Lin, 2000), and 315 days (Zhang et al., 2014; Sandrinelli et al., 2014) were identified, while a short time-scale oscillation of $\sim$4.6 hours was observed at $X-$ray energies (Lachowicz et al., 2009).

Evidence of quasi-periodic oscillations in the optical polarization of PKS 2155–304 is presented here. The polarization of the source was monitored from 25 – 27 July, 2009 with the HIgh Speed Photo-POlarimeter (HIPPO) of the Southern African Astronomical Society (SAAO). Gamma-ray observations were obtained independently with the High Energy Stereoscopic System (H.E.S.S.) over the same

period, with indications of two $\gamma-$ray flares which bracket the occurrence of the optical polarization fluctuations. The acquisition of the optical polarization measurements and a description of the polarization and $\gamma-$ray observations is given in Section 2.2. Section 2.3 presents an analysis of the observations. Discussion of the results follows in Section 2.4, while the conclusions are presented in Section 2.5.

2.2 Observations

The optical polarization of PKS 2155–304 was observed with the HIPPO (Potter et al., 2010), a rapidly rotating dual-channel photo-polarimeter operated by the SAAO. The instrument is mounted on the 1.9 metre Radcliffe telescope, which is located in Sutherland (South Africa). A comprehensive description of the polarimeter, data acquisition and reduction is presented in Potter et al. 2010. The most important instrument characteristics are described below.

The polarization of the incident light is measured by passing the incoming beam through a $\frac{1}{4}$ waveplate and a $\frac{1}{2}$ waveplate, which detects circular and linear polarization, respectively. The waveplates contra-rotate at 10 Hz, producing a modulation of the intensity dependent on the polarization of the beam. Simultaneous measurement of all Stokes parameters is obtained by rapidly sampling the polarization ellipse of the incoming beam as a function of angles during the rotation of the wave plates. A Thompson beam-splitter separates the beam into the orthogonal components of the electric field vector components, thereby allowing two independent measurements of the polarization. *UBVRI* colour filters, attached to each observation channel, enable two simultaneous colour measurements. Uncertainties in the calculated polarization are largely dependent on photon statistics, which is expected to be relatively small since PKS 2155–304 is a bright source ($m_B = 13^m.6$; Pica et al. 1988).

The intra-day variability (IDV) of the source was monitored from 25 – 27 July 2009 for a total of 9.23 hours using a time-resolution of 5 minutes. The linear and circular polarization of the source was recorded in the $I-$ and $B-$band. A summary of the daily average of the polarization degree and the electric vector

Table 2.1: The mean daily optical polarization of PKS 2155–304 in July 2009.

MJD	$T_{\rm obs}$ (min)	p (%)	θ (°)
55037	290	3.7 ± 0.3	88 ± 2.5
55038	195	7.0 ± 0.3	67 ± 1.0
55039	197	8.3 ± 0.7	68 ± 0.5

position angle (EVPA), or polarization angle[2], of the I– and B–band is presented in Table 2.1. The columns list the Modified Julian date (MJD), duration ($T_{\rm obs}$) and the polarization degree and polarization angle of the source. Table 2.1 demonstrates an increase in the polarization degree from approximately 4% to 8% between MJD = 55037 to 55038, accompanied by a decrease in the polarization angle from 88° to 68°. Historically, the polarization degree of PKS 2155–304 typically ranges from $2\% - 10\%$ on timescales of a few days (Tommasi et al., 2001) and the EVPA displays a systematic decrease on timescales exceeding ten years (Dominici et al., 2008), which is consistent with our findings. Figure 4.1 illustrates the change in the polarization degree. The $\gamma-$ray light curve as recorded by the H.E.S.S. for photons with energies > 300 GeV, is superimposed. The increase in the fractional polarization is associated with an increase in $\gamma-$ray activity, with two prominent flares being detected in the $\gamma-$ray flux, I, (H.E.S.S. Collaboration et al., 2014). The first flare peaks at $I = (8.0 \pm 0.4) \times 10^{-11}$ ph cm^{-2} s^{-1} and is located at MJD = 55035. A subsequent rise is then seen in the $\gamma-$ray flux between MJD = 55038 and 55039, from $I = (1.9 \pm 0.4) \times 10^{-11}$ ph cm^{-2} s^{-1} to $I = (5.6 \pm 0.4) \times 10^{-11}$ ph cm^{-2} s^{-1}, which could be indicative of a developing flare. However, this cannot be verified due to a lack of observations past MJD = 55039. Note that the second rise in $\gamma-$ray flux is accompanied by a similar rise in the polarization degree by about one day.

2.3 Quasi-Periodic Oscillations

The intra-day variation in the optical polarization was investigated by analyzing the high time resolution data taken over the course of each day. The number of photons collected in the I–band were typically an order of magnitude higher compared to

[2]The polarization angle is measured from the North Celestial Pole towards the Celestial East.

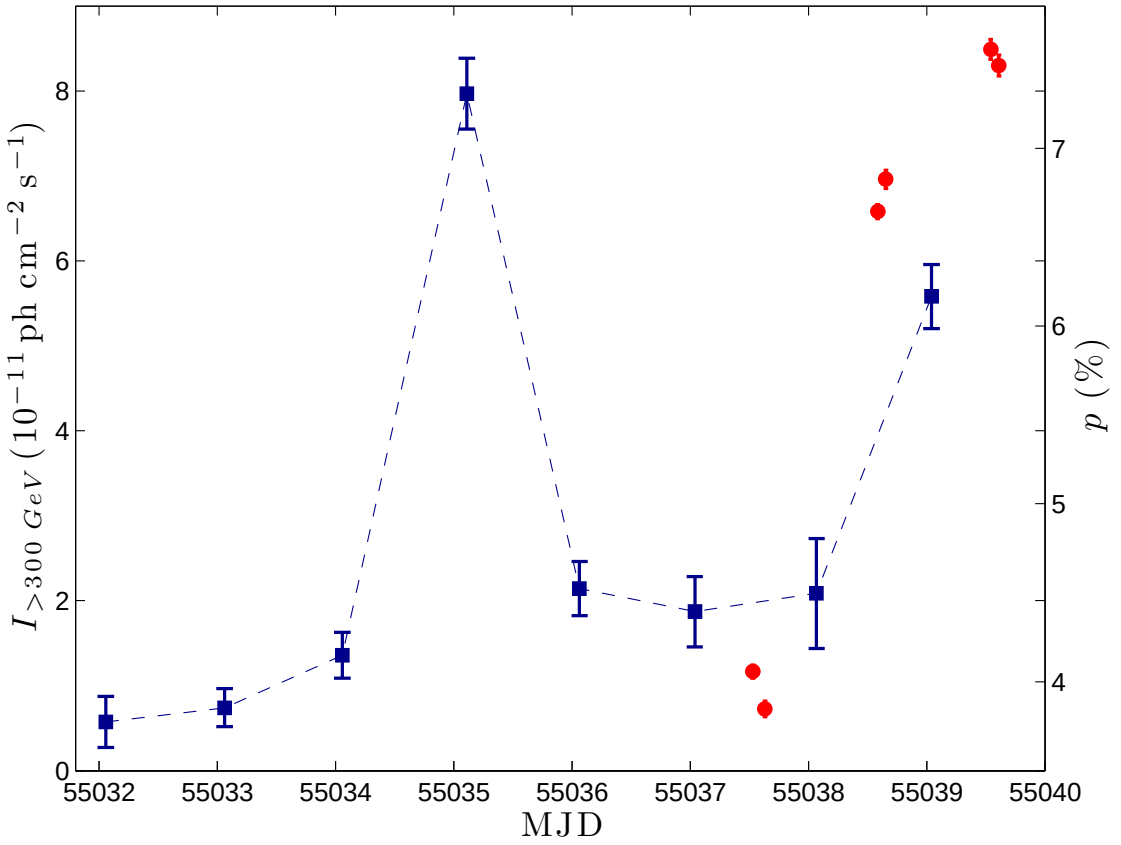

Figure 2.1: The $\gamma-$ray light curve of PKS 2155–304 for photons with energies > 300 GeV in July 2009, as seen by H.E.S.S. (H.E.S.S. Collaboration et al., 2014). The $\gamma-$ray intensity I, measured in ph cm^{-2} s^{-1}, is represented by the filled squares. The I–band polarization degree p (%) is superposed on the $\gamma-$ray light curve and is symbolized by the filled red circles. Two prominent increases in the $\gamma-$ray flux are detected. The first peak occurs on MJD $= 55035$, at $I = (8.0 \pm 0.4) \times 10^{-11}$ ph cm^{-2} s^{-1}. Another increase in $\gamma-$ray flux, from $(1.9 \pm 0.4) \times 10^{-11}$ ph cm^{-2} s^{-1} to $(5.6 \pm 0.4) \times 10^{-11}$ ph cm^{-2} s^{-1} is seen between MJD $= 55038$ and 55039.

the B–band. Since the measurement errors are dominated by photon statistics, the B–band observations display larger measurement errors. More robust measurements were recorded in the I–band, which is what we use in the following analysis.

Inspection of the IDV on MJD $= 55037$ over the 290 minutes of continuous observation (see Fig. 2.2) suggests that the amplitude of the polarization degree is modulated on a timescale of ~ 30 min. These short-term amplitude modulations are superposed on a slowly decreasing baseline. The oscillations thus precede the onset of the increase in the optical polarization degree seen in Fig. 4.1. It is noteworthy such short-term modulations are not seen on MJD $= 55038$ and 55039, after the

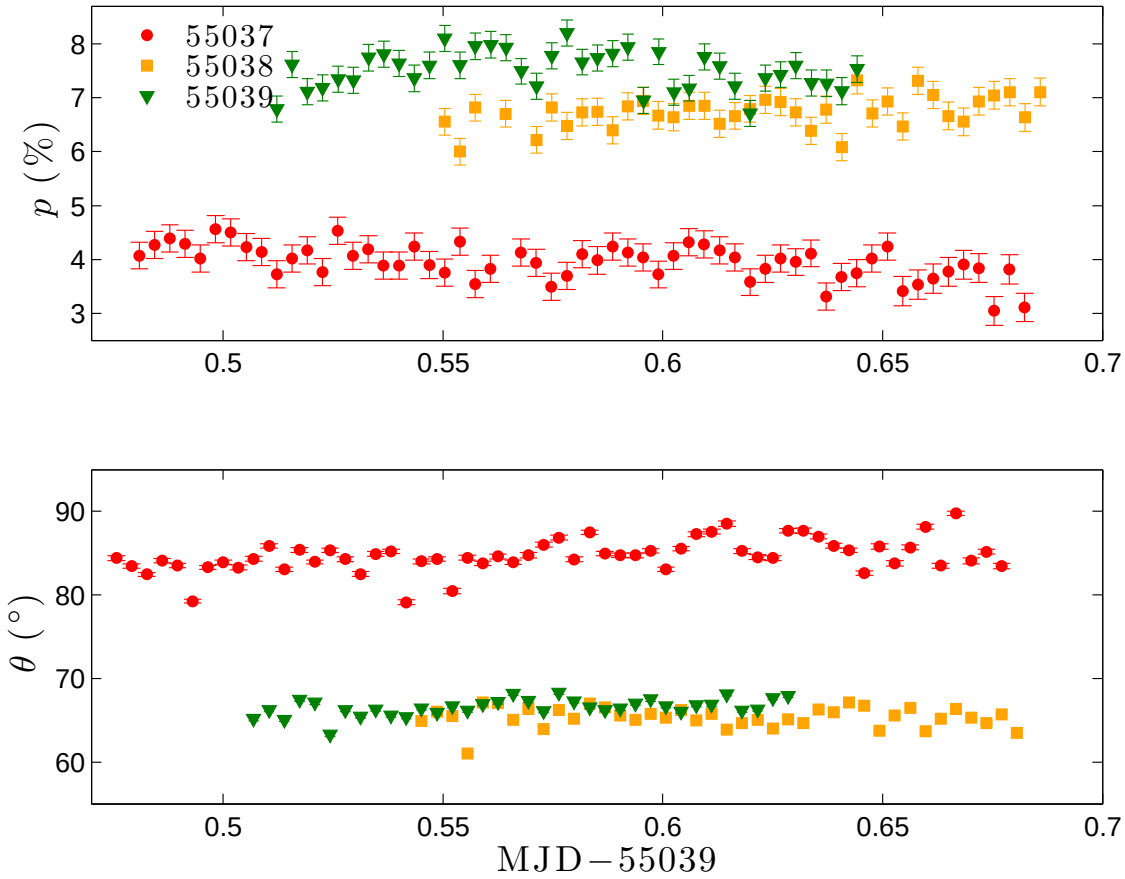

Figure 2.2: The intra-day variability of the I–band polarization (binned to 5 min) of PKS 2155–304 on MJD = 55037 (circles), 55038 (square markers) and 55039 (triangles). The top panel displays the polarization degree p (%), while the position angle of the electric vector θ (°) is shown in the bottom panel. The polarization degree appears to modulated by a periodic component on MJD = 55037.

onset of the rise in the polarized intensity and the second $\gamma-$ray flare.

To test for the presence of periodic components in the optical polarization we computed the periodogram, which measures the amount of variability power as a function of temporal frequency, normalized to the mean of the light curve, in units of (rms/mean)^2 per Hz (Schuster, 1898; Vaughan, 2005). The periodogram was oversampled by a factor of 10 relative to the grid defined by the Fourier frequencies $\nu_k = k/N\Delta T$ to provide good sampling of the spectrum, where N is the number of observations and ΔT is the sampling interval. The periodogram of the Stokes Q and U polarized intensities is displayed in Fig. 2.3. Two prominent peaks are detected at 565 ± 7 μHz and 1293 ± 6 μHz, labelled as A and B, respectively. Each peak signal is well-described by a Gaussian function, for which the uncertainty in

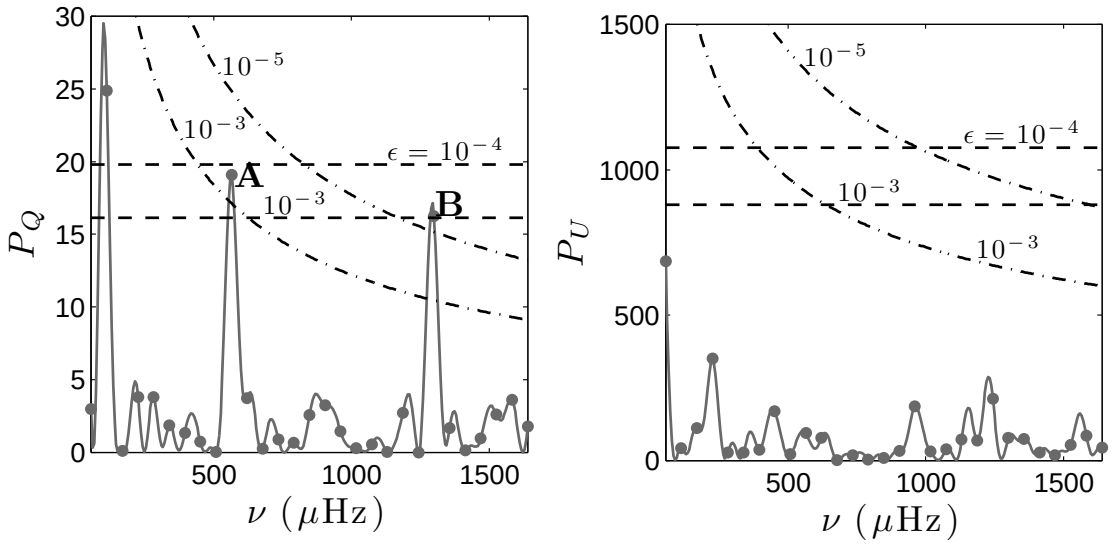

Figure 2.3: The periodogram of the polarized flux, in units of (rms/mean)^2 per Hz. The periodogram of the Stokes Q flux, P_Q, is presented in the left panel, while the periodogram of the Stokes U flux, P_U, is shown on the right. The filled circles represent the periodogram ordinates at the Fourier frequencies. Two prominent peaks are detected at $\nu_A = 565 \pm 7$ μHz and $\nu_B = 1293 \pm 6$ μHz, which are labelled as **A** and **B**, respectively. The false alarm probabilities for white noise, indicated by the dashed lines, and red noise, indicated by the dotted-dashed lines, are superposed.

the position of the peak is given by $\sigma_{\nu_0} = \mathrm{FWHM} \Big/ \left(2\sqrt{2\ln 2} \times \sqrt{snr}\right)$ (Condon, 1997), where FWHM is the full-width half-maximum of the peak and snr is its signal-to-noise ratio. The period corresponding to peak A is $T = 29.4$ min and $T = 12.9$ for peak B. No dominant peaks are detected in the Stokes U periodogram. The lack of detection in U is consistent with a variation in polarized intensity (as opposed to angle), as the observed polarization position angle $\theta \approx 90°$ (see Table 2.1 and Fig. 2.2), places virtually all the polarized emission in Q.

Figure 2.4 displays the Stokes Q light curve folded to the $T = 29.4$ min, the period of spectral component **A** and $T = 12.9$ min, the period of spectral component **B**. Two cycles are plotted for clarity. Although the amplitude modulation is small, a cyclic trend appears to be present for both periods. A non-linear least-squares fit to the data yields a best-fit sinusoid that agrees well with the phase-folded diagram, with a period of $T = 29.5$ min for signal A and $T = 12.9$ min for signal B.

The statistical significance of the periodogram was determined by comparing the observed peak power to the probabilities of deflections arising from a noise

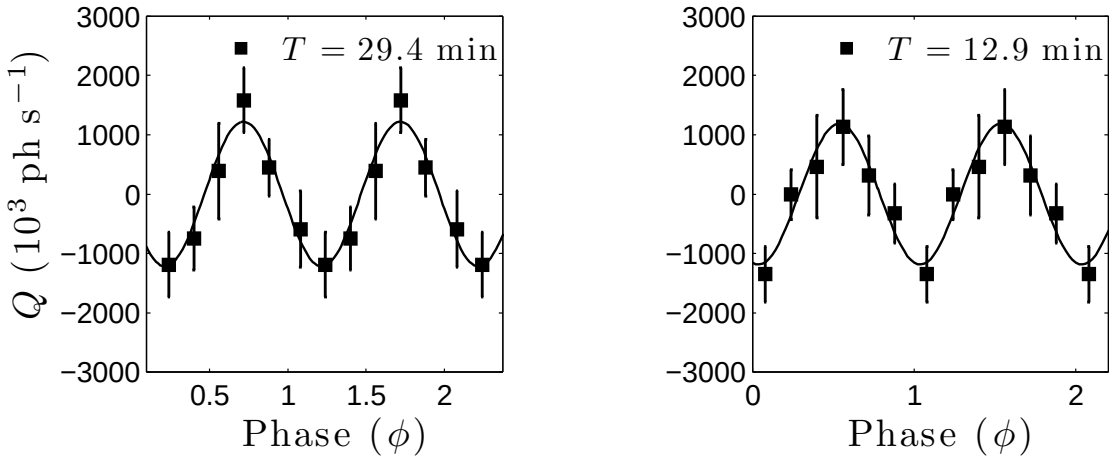

Figure 2.4: The Stokes Q light curve folded to $T = 29.4$ min and $T = 12.9$ min, averaged into six phase bins. Two cycles are plotted for clarity. A cyclic trend appears to be present for both trial periods. The solid line represents the best-fit sinusoid for each case.

continuum $S = N\nu^{-\alpha}$ (or red noise), where α is the spectral index, or slope, and N is the flux normalization of the spectrum. The model spectrum is obtained by fitting a power-law to the observed periodogram using the least-squares (LS) method described in Vaughan 2005. The result of the fit is displayed in Fig. 2.5, which shows the Stokes Q power spectrum on logarithmic axes. The slope is consistent with white noise ($\alpha = 0$), but a formal fit to the spectrum yields a de-biased best-fit line with $\alpha = 0.59 \pm 0.3$ (represented by the solid line). If S represents the true power spectral density, then the ratio $\gamma = 2P/S$ is scattered as a χ^2– distribution with two degrees of freedom and we can define confidence limits for the noise. The upper 99% confidence limit of the underlying continuum was calculated. Fig. 2.5 shows that the observed peaks are detected above the 99% confidence limit (represented by the red dashed line), with the chance probability of detecting peak A $\Pr[\gamma > \gamma_\epsilon] = 3.1 \times 10^{-4}$ (corresponding to $\sim 3\sigma$) and 3.4×10^{-6} for peak B, given the number of frequencies that were examined. The false alarm probabilities for the power-law model, and for white noise, are superposed on the periodogram in Fig. 2.3. The figure illustrates that the observed peaks exceed the $\epsilon = 10^{-3}$ false alarm threshold of white noise.

The robustness of this result was verified by generating 10^4 random light curves with the same mean, variance and sampling rate as the observations, following the procedure described in Timmer & Koenig 1995. The resulting distribution

of power for an underlying continuum with $\alpha = 0.6$ (the best-fit slope to the data) was recorded and the 99% and 99.7% confidence levels computed. The 99% confidence level from the simulated distribution is indicated by the teal dotted-dashed line in Fig. 2.5. Although the simulation shows that the LS test overestimates the significance of the periodic signal, peak A and peak B remain statistically significant, with peak A detected at $> 99\%$ significance, while peak B is detected at $> 99.7\%$ significance.

To conclude, the periodogram of the polarized flux is consistent with the presence of a periodic component at $T \sim 13$ min, with $> 99.7\%$ significance, and $T \sim 30$ min, which was found to be nominally significant at $> 99\%$.

2.4 Discussion

The optical emission in blazars is dominated by synchrotron radiation from relativistic electrons being accelerated in the jet's magnetic field. The polarization is determined by the degree of order and direction of the magnetic field, and the viewing angle of the observer. Since radiation from the jet is highly Doppler boosted, even for small changes in the viewing angle, significant brightness variations will be observed. Fast variations, such as those observed in the optical polarization of PKS 2155–304, therefore most likely originate in the Doppler boosted jet, from an emission region with a size which is comparable to the gravitational radius of the central engine. Using the timescale of the fastest periodic component as the variability timescale $t_{\rm var} \approx 13$ min, a redshift $z = 0.116$ (Falomo et al., 1993) and a Doppler factor $\delta \approx 30$ (Katarzyński et al., 2008), yields an upper limit to the size of the emission region $R \lesssim c\delta t_{\rm var}/(1+z) \approx 10^{15}$ cm.

Quasi-periodic variations can arise if an emission feature with physical properties distinct from the ambient jet medium, such as a relativistic shock, propagates down a jet which contains quasi-helical structures, either in the magnetic field or electron density (e.g., Qian et al. 1991; Romero 1995). A relativistic shock propagating down such an inhomogeneous jet will result in successive peaks in the amplitude of the total

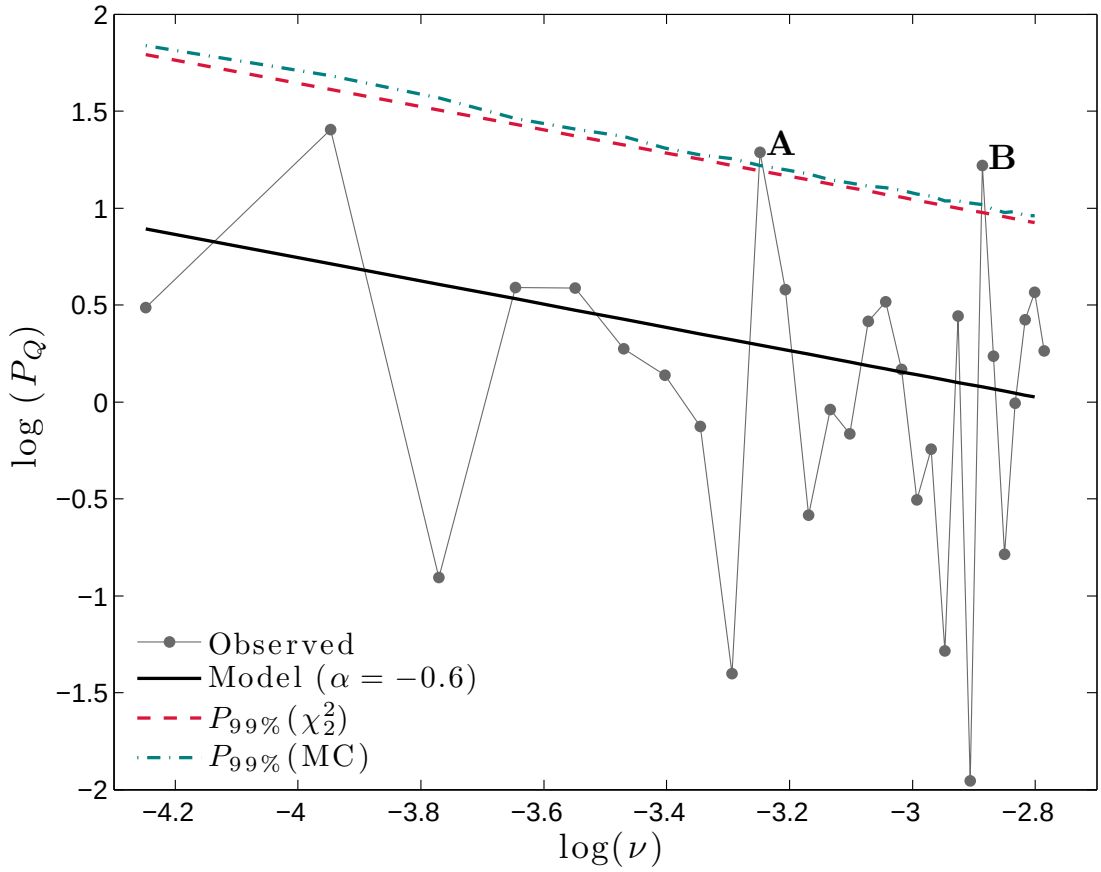

Figure 2.5: The power spectrum of the Stokes Q intensity, normalized to (rms/mean)^2 per Hz. The solid line represents the best-fit power-law with a slope $\alpha = 0.59 \pm 0.3$. The 99% confidence limit of the noise is represented by the dashed line. The robustness of this result was tested by generating 10^4 random light curves with the same mean, variance and sampling rate as the observations from an underlying continuum with $\alpha = 0.6$. The 99% confidence limit of the simulated power distribution is indicated by the teal dotted-dashed line.

and polarized emission at the viewing angle that provides the maximum boosting for the observer (e.g., Camenzind & Krockenberger 1992; Gopal-Krishna & Wiita 1992).

Turbulence behind the shock can also explain the presence of short-lived QPOs (Marscher et al., 1992). For such turbulent flows, the largest eddies will dominate the variability and the period will be determined by their turnover times. The presence of one or more such turbulent cells behind the same shock also provides a possible explanation for the presence of multiple QPOs in the same signal.

2.5 Conclusions

Monitoring of the intra-day optical polarization of PKS 2155–304 revealed the first evidence for quasi-periodic oscillations in the polarized flux of an AGN. The periodogram showed the existence of a periodic component at $T \sim 13$ min, detected at $> 99.7\%$ significance, and $T \sim 30$ min, which was found to be nominally significant at $> 99\%$. The periods of these oscillations are similar to the $T \approx 15$ min QPO seen in the optical light curve of the blazar S5 0716+714 (Rani et al., 2010), which provides further support for the existence of such short timescale periodicities in these sources.

Gamma-ray observations of the source over the same period showed that it was in a high state of activity, experiencing two $\gamma-$ray flares at very high energies (VHE, photons with energies exceeding a few GeV). The first simultaneous optical polarization measurements of the source during a high-state were recorded for the latter flare. Although the physical cause of this QPO is unclear, comparison with the VHE light curve showed that PKS 2155–304 experienced a $\gamma-$ray flare two days before the appearance of the QPOs and another peak two days later. The oscillations could therefore be related either to the late phase of post flare activity of the first flare, which is supported by the decreasing trend observed over the night (as opposed to increasing trend seen on the following nights, see Fig. 2.2) or due to transition between two different gamma-ray flares. Since blazar emission is dominated by synchrotron emission at low energies, which also leads to polarization, and inverse Compton emission at high energies, which both arise from the relativistic jet, this could suggest that the observed QPOs are part of a longer-lived phenomenon within the jet of PKS 2155–304.

Acknowledgements

The authors would like to thank the anonymous referee for many suggestions that significantly improved this paper.

We gratefully acknowledge the support of the South African National Research Foundation (NRF) and the Department of Science and Technology (DST) through the South African Square Kilometre Array Office. N.W.P. also thanks the Science Faculty at the University of Cape Town (UCT) and Centre for Space Physics at North-West University (NWU) for their support. The authors also thanks the H.E.S.S. Collaboration for taking the $\gamma-$ray observations, as well as Markus Böttcher for stimulating discussions.

3

The optical polarization of the blazar PKS 2155–304 during an optical flare in 2010

N. W. Peceur[1], A. R. Taylor[1,2,3] and R. C. Kraan-Korteweg[1]

[1]Department of Astronomy, University of Cape Town, Private Bag X3, Rondebosch 7701, SA

[2]Department of Physics and Astronomy, University of the Western Cape, Modderdam Road, Private Bag X17, Belville 7530, SA

[3]Inter-University Institute for Data Intensive Astronomy, University of Cape Town, Private Bag X3, Rondebosch 7701, SA

Abstract

An analysis is presented of the optical polarimetric and multicolour photometric ($BVRJ$) behaviour of the blazar PKS 2155–304 during an outburst in 2010. This flare develops over roughly 117 days, with a flux doubling time $\tau \sim 11$ days that increases from blue to red wavelengths. The polarization angle is initially aligned with the jet axis but rotates by roughly 90° as the flare grows. Two distinct states are evident at low and high fluxes. Below 18 mJy, the polarization angle takes on a wide range of values, without any clear relation to the flux. In contrast, there is a positive correlation between the polarization angle and flux above 18 mJy. The polarization degree does not display a clear correlation with the flux. We find that the photopolarimetric behaviour for the high flux state can be attributed to a variable component with a steady power-law spectral energy distribution and high optical polarization degree (13.3%). These properties are interpreted within the shock-in-jet model, which shows that the observed variability can be explained by a shock that is seen nearly edge-on. Some parameters derived for the relativistic jet within the shock-in-jet model are: $B = 0.06$ G for the magnetic field, $\delta = 22.3$ for the Doppler factor and $\Phi = 2.6°$ for the viewing angle.

3.1 Introduction

Blazars are a subclass of radio-loud AGN, where the relativistic jet is closely aligned to the line-of-sight of the observer (Urry & Padovani, 1995a) and for which the most extreme observational properties are detected (Fan & Lin, 2000; H.E.S.S. Collaboration et al., 2007; Kastendieck et al., 2011). The observed radiation spans the entire electromagnetic spectrum, from radio to γ–ray wavelengths, and is dominated by non-thermal emission from a relativistic jet, as well as the presence of polarization at radio and optical wavelengths. The spectral energy distribution (SED) consists of two broad emission features. The low-energy component is located at optical to soft X–ray energies and is due to relativistic electrons spiralling in a magnetic field (synchrotron emission). The high-energy component is located at hard X–ray to γ–ray energies and is attributed to Inverse Compton emission of the relativistic electrons. The seed photons for inverse Compton scattering can be provided by the synchrotron emitting electrons themselves (Synchrotron Self Compton emission), or from external photon fields (External Compton emission) (H.E.S.S. Collaboration et al., 2009c; H.E.S.S. Collaboration, Aharonian, Akhperjanian, Anton et al., Abd; Reynoso et al., 2012; Chen et al., 2012). The magnetic field of the jet therefore underlies the physical processes that produce the observed blazar emission.

The polarization is a direct observable of the magnetic field and can provide useful information on the geometry and degree of order of the magnetic field of the relativistic jet. The degree of optical polarization could be related to the level of ordering of the magnetic field or to the electron energy distribution within the emission region, while the position angle of the polarization vector could be related to the direction of the magnetic field vector along the line of sight (Angel & Stockman, 1980; Lister & Smith, 2000; Dulwich et al., 2009).

Various models have been proposed to explain the observed polarization of blazars. These models can be divided into two classes: deterministic and stochastic. Stochastic models are based on lowering the maximum possible polarization degree for synchrotron radiation ($\sim 69\%$ for a power-law particle spectrum with index

$p = 2$) to values that are more compatible with observations ($\lesssim 10\%$) by assuming that the emission region is composed of many cells, each containing a roughly uniform magnetic field that is randomly oriented from cell to cell (e.g. Jones et al. 1985; Jones 1988; Marscher 2014; Kiehlmann et al. 2016).

Deterministic models usually consider the polarization due to a large scale helical magnetic field (e.g. Lyutikov et al. 2005), velocity shear (e.g. Laing 1980; D'Arcangelo et al. 2009), or the compression of an initially tangled magnetic field by shock waves in the jet (shock-in-jet model, Marscher & Gear 1985; Hughes et al. 1985; Cawthorne & Cobb 1990). For a helical magnetic field geometry, the net magnetic field seen by the observer can appear to be either transverse or longitudinal (Lyutikov et al., 2005), while an initially turbulent magnetic field can be partially ordered through velocity shear or shocks propagating in the jet. Velocity shear can arise when fast plasma near the jet axis flows past slower material closer to the boundary. The resulting velocity gradient stretches and aligns the magnetic field along the direction of flow, leading to transverse polarization angles (e.g. Laing 1980; D'Arcangelo et al. 2009). Shocks can partially order a turbulent magnetic field by compressing the magnetic field component parallel to the shock front. For transverse or oblique shocks (e.g. Hughes et al. 1985; Lister et al. 1998; Hughes et al. 2011), the shock front is oriented transverse to the jet axis or at an oblique angle, resulting in polarization angles that are aligned with the jet axis[2]. For conical shocks, the polarization angle can be either parallel or perpendicular to the jet axis (Cawthorne & Cobb, 1990). However, the largest possible polarization for the transverse case is $\sim$ 10%.

Two component models, where the polarization is attributed to a variable component of higher polarization degree superposed on a constant component with lower polarization degree, have also been successful at modelling the observed polarization of blazars (e.g. Hagen-Thorn et al. 2008; Barres de Almeida et al. 2010; Sorcia et al. 2013; Gaur et al. 2014; Bhatta et al. 2015). The constant component is

[2]Relativistic aberration tends to make larger viewing angles appear smaller such that an oblique shock will appear to be oriented closer to the jet viewing angle, thereby appearing to be a transverse shock.

usually identified with persistent emission from the quiescent jet, while the variable component is attributed to a shock. For the shock-in-jet model, ordering of the magnetic field in the shocked region leads to a positive correlation between the polarization degree and total flux (e.g. Hagen-Thorn et al. 2008; Sorcia et al. 2013) if the quiescent jet has a completely chaotic magnetic field. However, if the magnetic field in the unshocked region possesses a component parallel to the jet axis, the shock may strengthen the total flux but partially cancel the polarization, leading to an increase in total flux and a decrease in polarization degree (e.g. Hagen-Thorn et al. 2002; Gaur et al. 2014).

It is not clear which model best describes the photopolarimetric behaviour of flaring blazars. Here, we present quasi-simultaneous multiband photometric and polarization observations of PKS 2155–304 during a prominent optical flare in 2010, in an effort to understand the origin of the observed variability. Measurements were obtained from the long-term monitoring campaign of gamma-ray emitting blazars operated by the Steward Observatory and the SMARTS blazar programme. The polarized and photometric fluxes are compared and analyzed in terms of a two-component model. The paper is organized as follows: Section 4.2 describes the observations, followed by a photopolarimetric analysis of the source in Section 3.3, a discussion of the results is presented in Section 4.7 and the conclusions are put forth in Section 4.10.

3.2 Observations

PKS 2155–304 is a target of the long-term monitoring of the optical polarization of Fermi detected gamma-ray blazars, operated by the Steward Observatory (Smith et al., 2009), and of the Small and Moderate Aperture Research Telescope System (SMARTS), a long-term photometric monitoring programme operated by the Cerro Tololo Inter-American Observatory (Bonning et al., 2012). Photopolarimetric

measurements of the source were obtained from the publicly available SMARTS and Steward Observatory archives[3].

The Steward Observatory's polarization measurements are performed using SPOL, an imaging spectro-polarimeter consisting of polarizing optics, a spectrograph and a CCD imaging camera. The instrument is mounted on the 1.54 m Kuiper telescope or the 2.3 m Bok telescope of the Steward observatory. Light incident on the telescope is passed through an achromatic $\frac{1}{4}$– and $\frac{1}{2}$–wave plate, which measures circular and linear polarization, respectively. A Wollaston prism separates the incident beam into its two orthogonal components, thereby enabling two independent measurements of the polarization. The polarization in the B–, V– and R–band were calculated by multiplying the relative Stokes spectrum (measured between 4355 Å – 7195 Å) with the B–, V– and R–band spectral response functions of the telescope.

The SMARTS photometric observations are performed at optical and near-infrared wavelengths using four small telescopes (1.5m, 1.3m, 1.0m and 0.9m) that are located in Chile. Measurements are obtained with ANDICAM, a dual-channel imager with a dichroic that feeds an optical CCD and an infrared (IR) imager, resulting in simultaneous B–, V–, R–, J– and K–band observations. Photometric errors as low as 0.01 mag in the optical and 0.02 mag in the IR are observed for bright sources (<16 mag in the optical and <13 mag in IR).

The results of the photometric observations between April 2009 and Dec 2014 are shown in Fig. 3.1. The light curves reveal the presence of multiple flares throughout the monitoring period. The most prominent optical outburst occurs in 2010 (visible across all bands), with the source reaching a peak flux of $I_R = 30.5 \pm 1.7$ mJy in the R–band on MJD = 55538. Figure 3.2 displays simultaneous photopolarimetric measurements of PKS 2155–304 for the flare. The figure demonstrates erratic variability for the polarization degree, while the polarization angle or electric vector position angle (EVPA) appears to follow an overall decreasing trend, changing by approximately 90°. At the onset of the flare, the polarization angle is aligned with

[3]The Steward Observatory archive can be found at `http://james.as.arizona.edu/~psmith/Fermi/`. The SMARTS archive can be found at `http://www.astro.yale.edu/smarts/glast/home.php`

the jet axis ($\theta = 150^\circ - 160^\circ$, Piner et al. 2008, 2010), thereafter changing to an EVPA that lies roughly transverse to the jet direction as the flare grows.

3.3 PhotoPolarimetric Analysis

Inspection of the relationship between the polarization angle and R–band flux shows the existence of two distinct states at low and high fluxes (see Fig. 3.3). Below 18 mJy, the polarization angle takes on a range of values ($\sim 75^\circ - 150^\circ$) without any clear relation to the flux, while a positive correlation is observed between the EVPA and R–band flux above 18 mJy (with a correlation coefficient $r = 0.84$), with the polarization angle oriented roughly transverse to the jet direction ($60^\circ - 70^\circ$) for the epoch of highest polarization. The polarization degree, in contrast, does not demonstrate a clear correlation with the flux, although the maximum polarization degree is detected during the high flux state.

3.3.1 Polarization Parameters of the Variable Component

Following Hagen-Thorn & Marchenko (1999), the observed emission is decomposed as the superposition of a variable component and a constant component, $I = I_{\rm var} + I_{\rm cons}$, which yields:

$$\begin{cases} Q = q_{\rm var} I + (Q_{\rm cons} - q_{\rm var} I_{\rm cons}) \\ U = u_{\rm var} I + (U_{\rm cons} - u_{\rm var} I_{\rm cons}), \end{cases} \tag{3.1}$$

where the subscripts var and cons denote the variable and constant emission component, respectively. Then, if the variable component has constant polarization properties (i.e. $q_{\rm var}$ and $u_{\rm var}$ is constant), a linear relationship will be observed for Q versus I and U versus I. The slopes of these lines are the relative Stokes parameters of the variable component (see Equation 3.1), which give the polarization degree and EVPA of the variable emission component. Hence, a linear relation in the space of the Stokes parameters $\{I, Q, U\}$ suggests that the observed emission is due to a single variable component with constant polarization degree and angle.

Figure 3.4 displays the relationship between the Stokes fluxes and the R–band flux. Inspection of Fig. 3.4 reveals two distinct types of behaviour. The Stokes

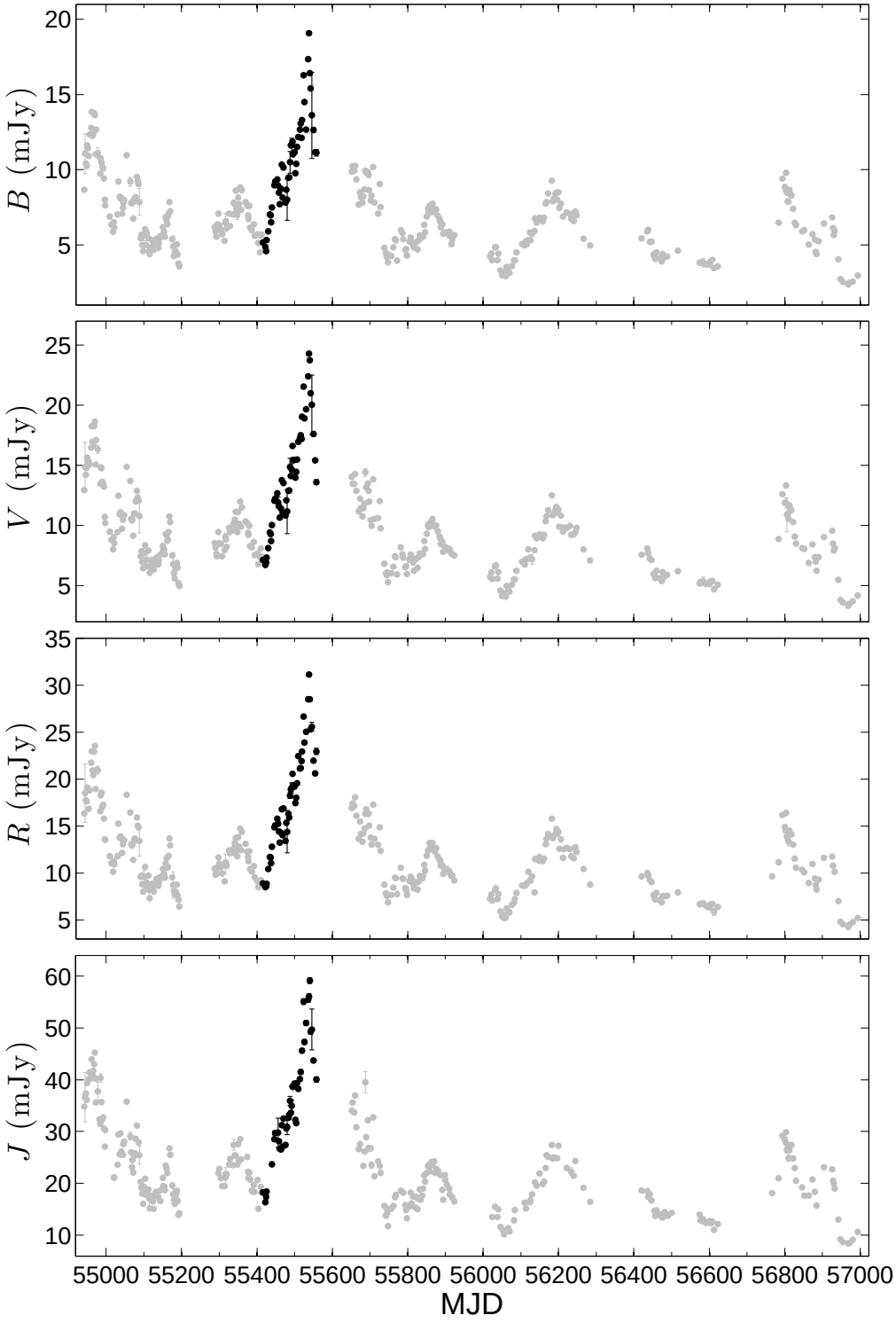

Figure 3.1: Extinction-corrected multiband light curves of PKS 2155–304 between April 2009 and Dec 2014. The most prominent flare occurred in 2010 and is shown in black. The flare is visible for all of the observed bands.

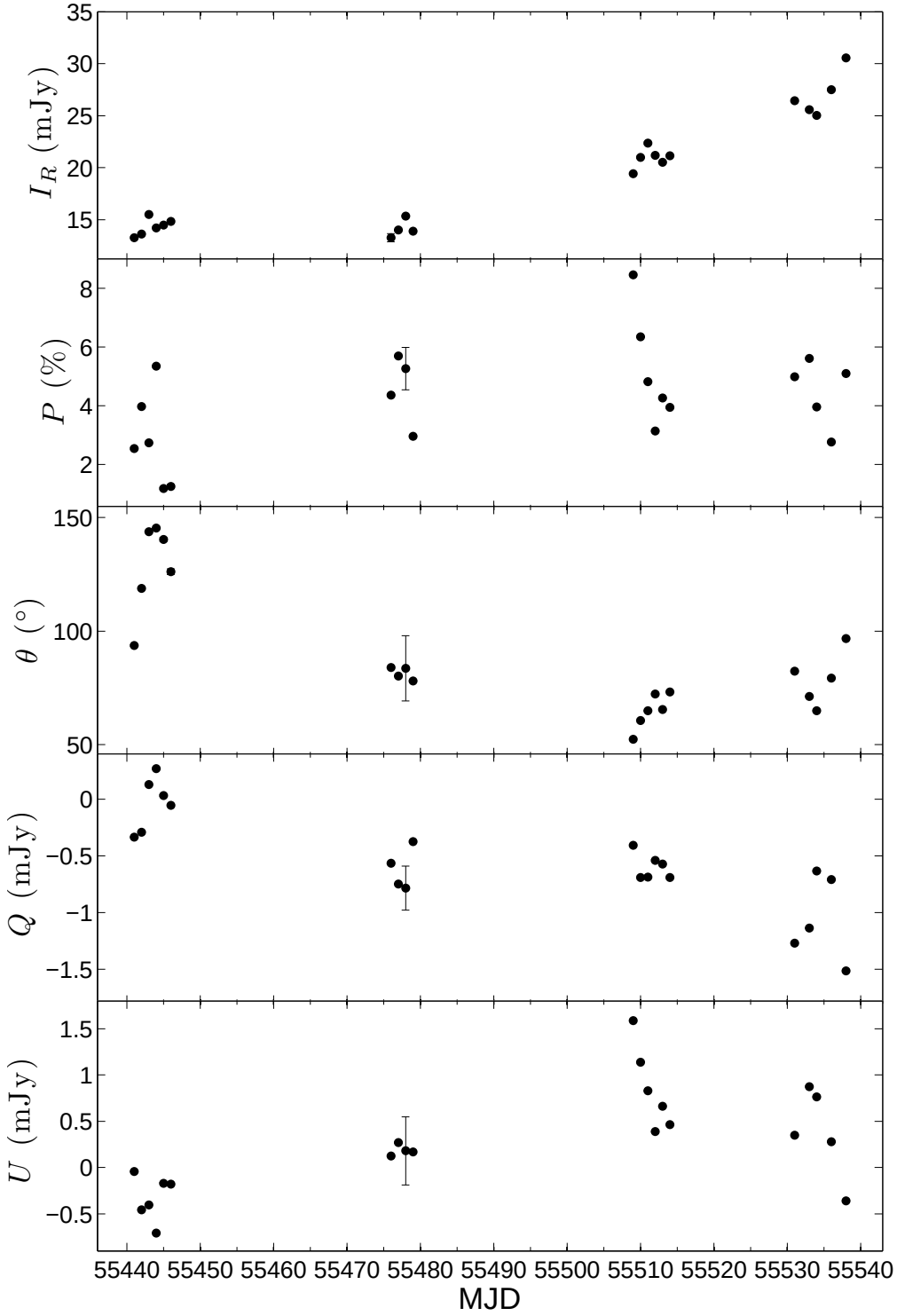

Figure 3.2: Simultaneous photopolarimetric observations of PKS 2155–304 during its 2010 optical outburst. The panels from top to bottom display the photometric flux, polarization degree, polarization angle, absolute Stokes Q flux and the absolute Stokes U flux. All measurements were obtained in the R–band.

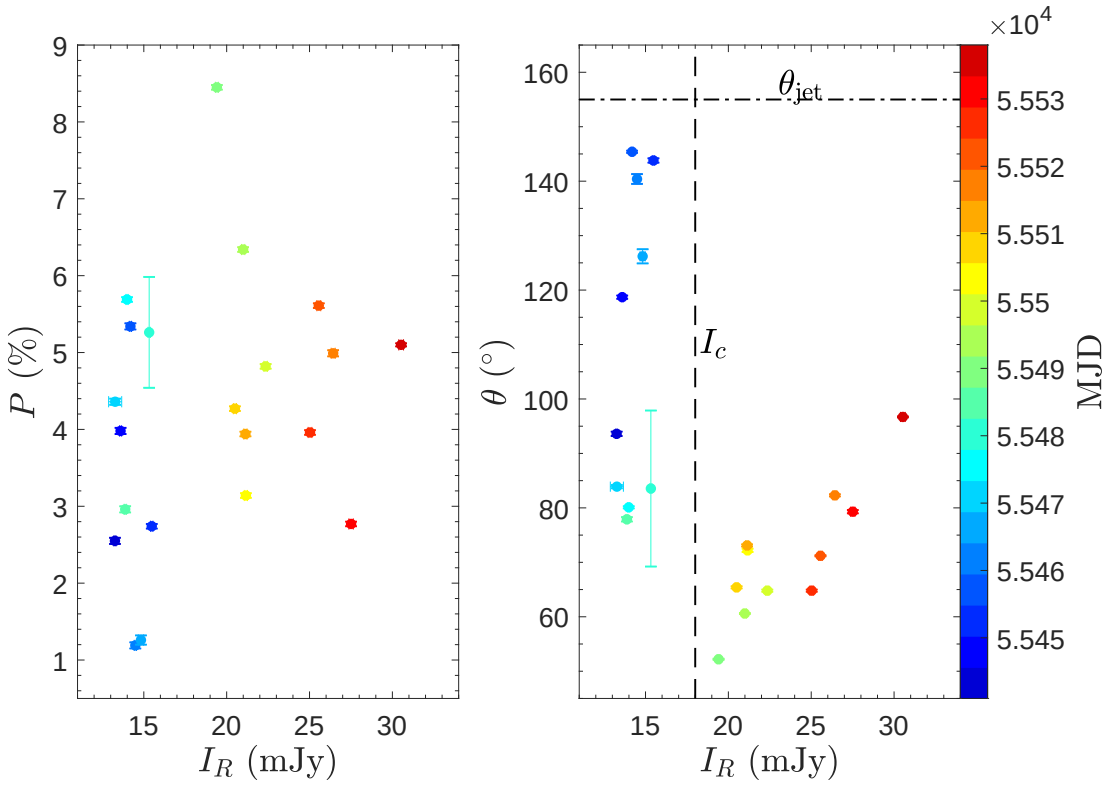

Figure 3.3: *Left:* Dependence between the polarization degree and R–band flux. *Right:* Dependence between polarization angle and R-band flux. Note two distinct states above and below $I_c = 18$ mJy (dashed line). The dotted-dashed line represents the jet direction. Colour indicates the date of the observation, with the scale given by the colour bar.

Q and U flux appear to vary randomly between -0.8 mJy and 0.3 mJy below 18 mJy, while there is a linear relationship between the variables above 18 mJy with a correlation coefficient $r_{Q-I} = -0.82$ for Q vs I and $r_{U-I} = -0.72$ for U vs I. The best fit line, calculated using the orthogonal regression method, is superimposed. The slope of each line gives the relative Stokes parameters of the variable component which yields $p_{\rm var} = 13.3 \pm 2.8\%$ for the polarization degree and $\theta_{\rm var} = 116 \pm 6°$ for the polarization angle of the variable component. The polarization degree is comparable to the highest fractional polarization for the variable component found by Barres de Almeida et al. (2010), $p = 12.5\%$. The derived polarization degree is relatively small when compared to the maximum possible polarization for a synchrotron source with $\alpha = 1.12$ (cf. Section 3.3.2) in a uniform magnetic field ($p = 76\%$), which is indicative of a non-uniform magnetic field direction inside the emitting region.

Below 18 mJy, the polarization variability appears to be well represented by a uniform distribution. Random sampling Q and U from the uniform distribution on the same interval $[-0.8, 0.3]$ yields a variance $\sigma^2_{Q_m} = 0.13$ and $\sigma^2_{U_m} = 0.15$, which is comparable to the observed values, $\sigma^2_Q = 0.13$ and $\sigma^2_U = 0.10$. Therefore, the polarization variability is well-represented by a uniform distribution during the low flux state.

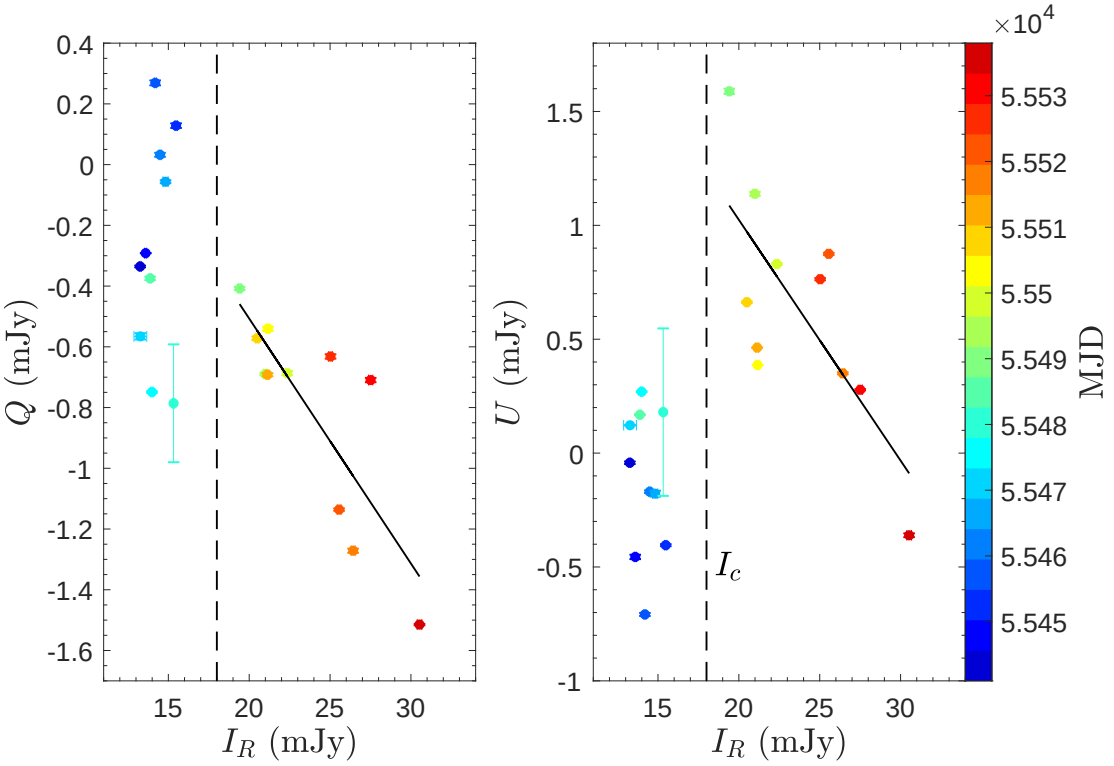

Figure 3.4: Comparison of the absolute Stokes parameters during the optical flare seen in 2010. The linear fit to the data for all $I > 18$ mJy is indicated by the solid line. The dashed line represents $I_c = 18$ mJy. Colour indicates the date of the observation, with the scale given by the colour bar.

3.3.2 Spectral Energy Distribution of the Variable Component

For photometry, the flux ratios for different pairs of spectral bands are (Hagen-Thorn & Marchenko, 1999):

$$\left(\frac{I_\nu}{I_{\nu_0}}\right)^{\text{var}} = \alpha_{\nu\nu_0}, \tag{3.2}$$

where the superscript refers to the variable emission component and ν_0 is the reference spectral band. If the spectral index of the variable emission does not change with frequency then these flux ratios are constant and

$$I_\nu = \alpha_{\nu\nu_0} I_{\nu_0} + \left(I_\nu^{\rm cons} - \alpha_{\nu\nu_0} I_{\nu_0}^{\rm cons} \right). \tag{3.3}$$

Equation 3.3 shows that a linear relationship will be observed for I_ν versus I_{ν_0} for multicolour observations. Hence, a linear relation in the flux-flux diagrams for several bands indicates that the relative SED of the variable component remains steady. The spectral index of the variable emission can then be derived from the slope of the best fit line for $\log \alpha_{\nu\nu_0}$ versus $\log \nu$.

The B–, V– and J–band fluxes relative to the R–band flux is displayed in Fig. 3.5, with the best fit lines calculated using the orthogonal regression method. The slopes of the fitted lines represent the flux ratio between the given pairs of bands. Since a linear relationship is observed it can be inferred that the relative SED of the variable component remains steady during the observation period. The variable emission spectrum of the source is displayed in Fig. 3.6, which shows that the SED is well-described by a power-law $F_\nu \propto \nu^{-\alpha}$ with slope $\alpha = 1.12 \pm 0.07$, consistent with emission from a synchrotron source.

3.3.3 Variability Timescale

Following Burbidge et al. (1974), the timescale of variability for the multiband light curves is defined as $\tau = dt/\ln(I_1/I_2)$, where dt is the time interval between flux measurements I_1 and I_2, with $I_1 > I_2$. All possible timescales τ_{ij} are calculated for any pair of observations for which $|I_i - I_j| > \sigma_{I_i} + \sigma_{I_j}$. The minimum variability timescale is then given by $\tau = \min\{\tau_{ij}\}$, where $i = 1...N-1$, $j = i+1, ...N$ and N is the number of observations. The results are listed in Table 3.1. The columns are (1) the observation band, with I_P the polarized flux in the R–band, (2) the number of observations N and (3) the variability timescale τ (days). Table 3.1 indicates that the timescale of variability during the flare is on the order of a few days and that light curves with similar sampling display an increase of timescale with wavelength.

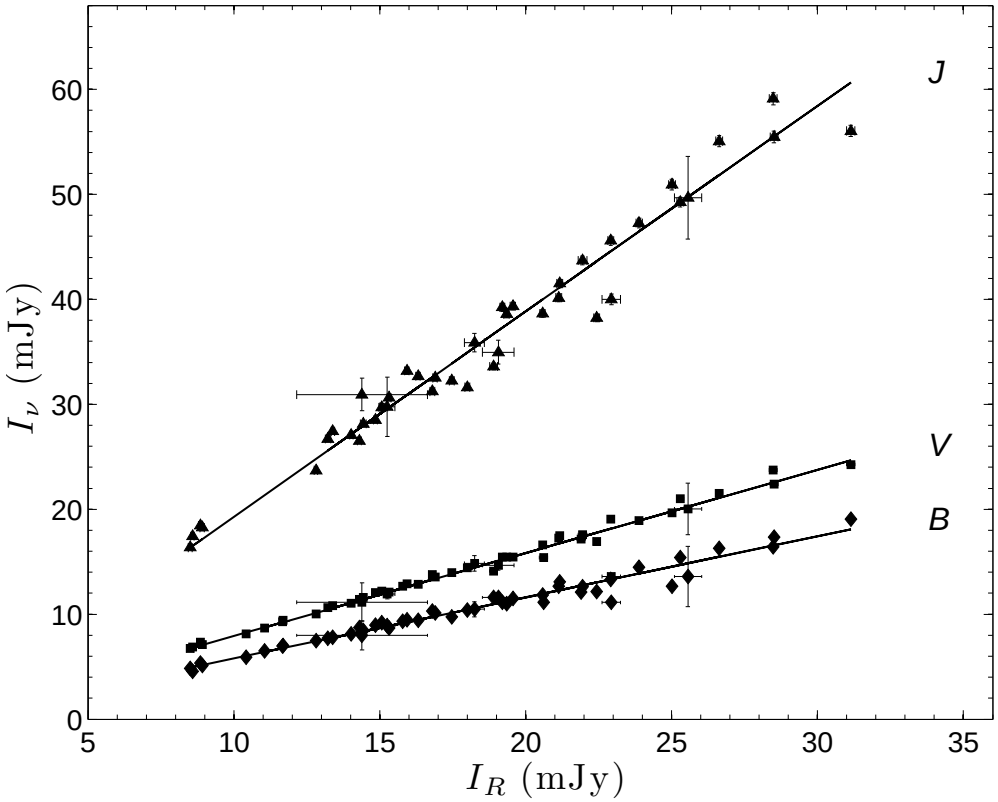

Figure 3.5: The B–, V– and J–band fluxes relative to the R–band flux during the 2010 optical flare of PKS 2155–304. The best fit lines are superimposed.

Table 3.1: Variability timescales of PKS 2155–304 during its 2010 outburst

(1) Band	(2) N	(3) $\tau_{\rm min}$ (days)
B	49	8.38
V	49	9.09
R	49	10.75
J	42	9.16
I_P	21	0.68

The shortest timescale, $\tau \sim 0.7$ days, occurred in the polarized flux. Comparison of the variability timescales of the total and polarized R–band fluxes implies that the polarized emission originates in a subsection ($\sim \frac{1}{16}$) of the optical emission region.

3.4 Discussion

Simultaneous polarimetric and photometric observations of PKS 2155–304 show that the optical flare seen in 2010 can be attributed to a single variable component

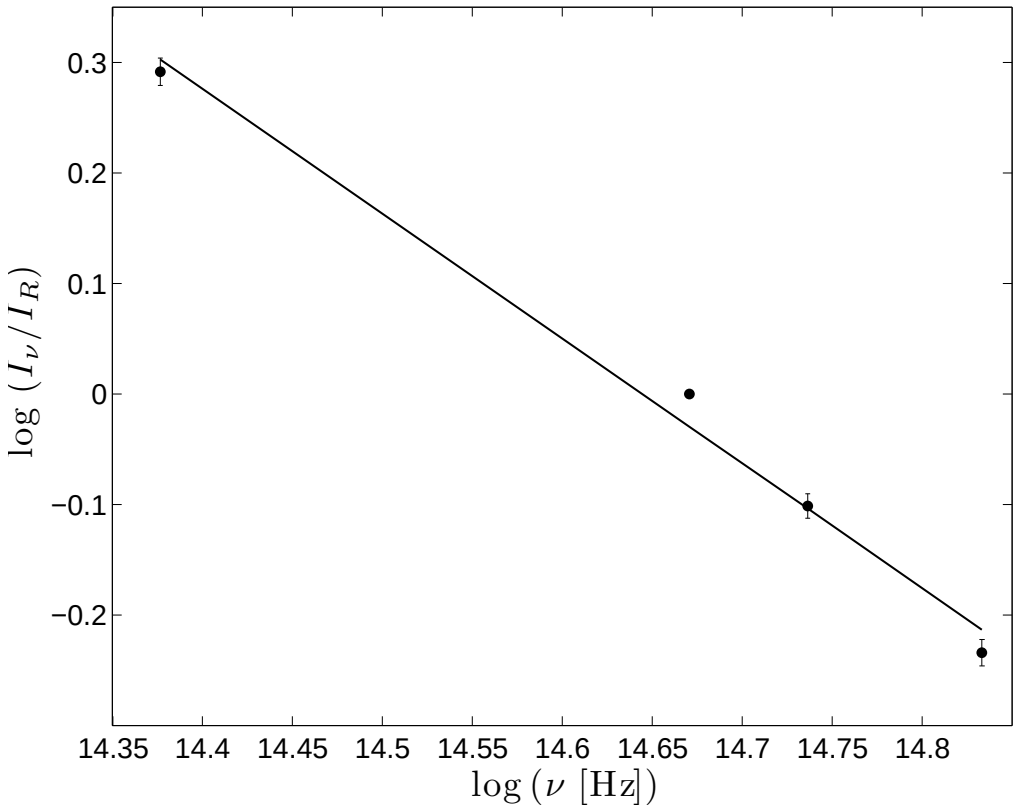

Figure 3.6: Relative SED of the variable emission component of PKS 2155–304 during its 2010 outburst. The best fit line is superimposed, with slope $\alpha = 1.12 \pm 0.07$.

with the following properties:

1. a steady spectral shape,
2. a high degree of polarization,
3. a correlation between the flux and polarization angle,
4. a tendency of the magnetic field to be transverse to the jet direction during the epoch of highest polarization, and
5. an increase in the timescale of variability with wavelength.

These characteristics are consistent with a shock propagating in a relativistic jet with a turbulent magnetic field (Marscher & Gear, 1985; Hughes et al., 1985), with synchrotron radiation losses leading to larger variability timescales at longer wavelengths. The shock orders the turbulent magnetic field along the shock front,

leading to a change in the polarization angle. Since transverse shocks lead to polarization angles oriented parallel to the jet axis, it is more likely that an oblique shock is responsible for the observed emission.

3.4.1 Shock-in-Jet Model

The observed flux of a shock moving through a turbulent plasma with constant bulk Lorentz factor Γ is:

$$F = F_0 \nu^{-\alpha} \delta^{(3+\alpha)} \delta'^{(2+\alpha)}, \tag{3.4}$$

where F_0 is the flux scaling factor, $\delta = [\Gamma(1 - \beta \cos \Phi)]^{-1}$ is the Doppler factor of the jet in the observer's frame, $\beta = \sqrt{1 - \Gamma^{-2}}$ is the speed of the shock normalized to the speed of light and Φ is the viewing angle of the jet in the observer's frame. The factor δ' is the Doppler factor of the shocked plasma in the rest frame of the shock. Without loss of generality, it can be assumed that the velocity of the shocked plasma in the frame of the shock is $\ll c$, where c is the speed of light and $\delta' \approx 1$ (Hagen-Thorn et al., 2008).

From Hughes & Miller (1991), the polarization degree of the shocked plasma is:

$$p \approx \frac{\alpha + 1}{\alpha + 5/3} \frac{(1 - \eta^{-2}) \sin^2 \Psi}{2 - (1 - \eta^{-2}) \sin^2 \Psi}, \tag{3.5}$$

where $\eta = n_{\text{shock}}/n_{\text{unshocked}}$ is the density of the shocked region relative to the unshocked region and Ψ is the viewing angle of the shock in the observer's frame, which is subject to relativistic aberration and is defined as:

$$\Psi = \tan^{-1} \left\{ \sin \Phi / \left[\Gamma \left(\cos \Phi - \sqrt{1 - \Gamma^{-2}} \right) \right] \right\} \tag{3.6}$$

Typical bulk Lorentz factors derived from emission models of the VHE emission of PKS 2155–304 during the high state seen in 2006 yield $\Gamma = 25 - 50$ (Foschini et al., 2007; Begelman et al., 2008; Narayan & Piran, 2012), while Reynoso et al. (2012) showed that the observed VHE emission could also be explained by multiple shocks with $\Gamma = 10.5 - 13$. The Doppler factor $\delta(t)$ can then be determined from Equation 3.4 by adopting $\alpha = 1.12$, the spectral index of the variable component,

and an average value of $\Gamma \sim 20$. The scaling factor $F_0 = F_{\max}\nu^{\alpha}/\delta_0^{(3+\alpha)}$, with $F_{\max}$ the observed flux in the $R-$ band at peak polarization. The δ_0 factor is calculated from $\Phi_0 = 2.9°$, which is determined from Equation 3.6 for $\Psi = 90°$, corresponding to the maximum polarization degree due to the shock. The evolution of the shock parameters are found by using $\delta(t)$ to solve for $\Phi(t)$, which is then used to solve for the viewing angle of the shock, $\Psi(t)$, through Equation 3.6. The shock compression factor, $\eta(t)$, can then be derived by substituting $\Psi(t)$ and the observed polarization degree into Equation 3.5. The resulting shock parameters are displayed in Fig. 3.7 and demonstrate that, for constant bulk Lorentz factor, small changes in the viewing angle ($< 1°$) and plasma compression factor ($\Delta\eta = 0.10$) produce large variations in the flux and polarization degree. The peak flux is reached when the viewing angle of the jet is a minimum ($\Phi = 2.6°$). The plasma compression reaches its highest value during the rising phase of the flare, roughly 30 days before the total brightness reaches its peak value. However, η does not appear to have any systematic trends.

The shock is seen nearly edge-on throughout the flaring period ($\Psi \sim 91°$), varying by $< 12°$, which implies that the shock is seen at an oblique angle to the jet axis (see Fig. 3.8). Compression of the magnetic field by the shock yields a net magnetic field component parallel to the shock front. The parallel and perpendicular magnetic field components with respect to the jet axis are then given by $B_{\parallel} = B\cos\Phi$ and $B_{\perp} = B\sin\Phi$, respectively. The corresponding electric field components perpendicular and parallel to the jet axis are $E_{\perp} = E\cos\Phi$ and $E_{\parallel} = E\sin\Phi$ (see Fig. 3.8). For the small angle approximation relevant for blazars the electric field components reduce to $E_{\perp} \approx E$ and $E_{\parallel} \approx 0$. Hence, the polarization angle for an edge-on shock is expected to lie transverse to the jet axis, as demonstrated in Fig. 3.2, which shows that the polarization angle lies roughly transverse to the jet axis during the peak polarization epoch ($\theta \sim 60° - 70°$).

For the shock-in-jet scenario, relativistic electrons are injected into the emitting region by the shock, leading to a steady spectral shape and short timescale of the variability in the optical bands. A steady spectral shape implies a quasi-steady state of the emission between the rate of injection and radiative losses, which is

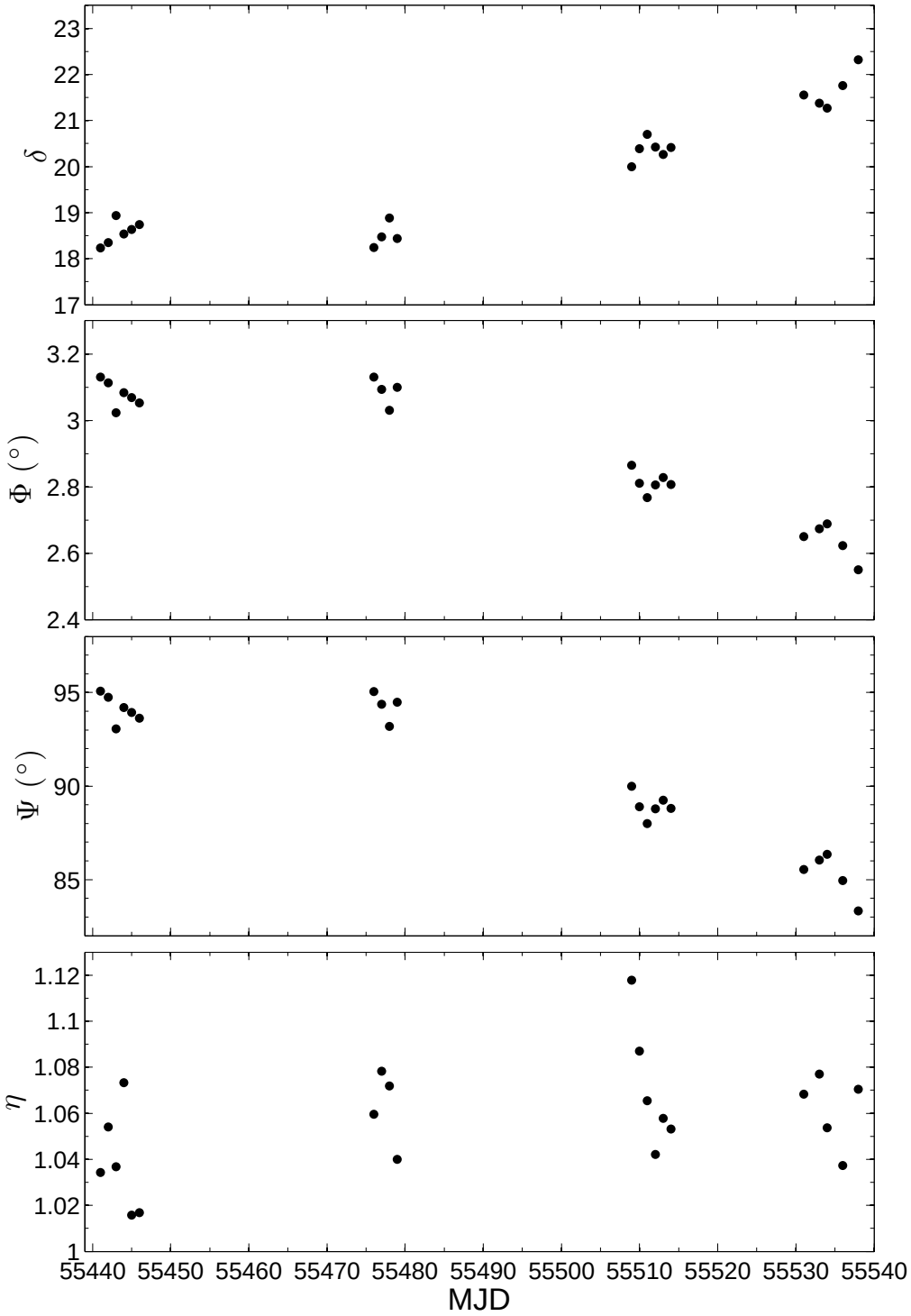

Figure 3.7: Derived values for the Doppler factor δ, jet viewing angle Φ, viewing angle of the shock Ψ and compression factor of the shocked plasma η for PKS 2155–304 during its 2010 optical outburst.

re-established every $8 - 11$ lt-days. The timescale of variability relates to the thickness of the shock front, which is determined by the lifetime of the relativistic

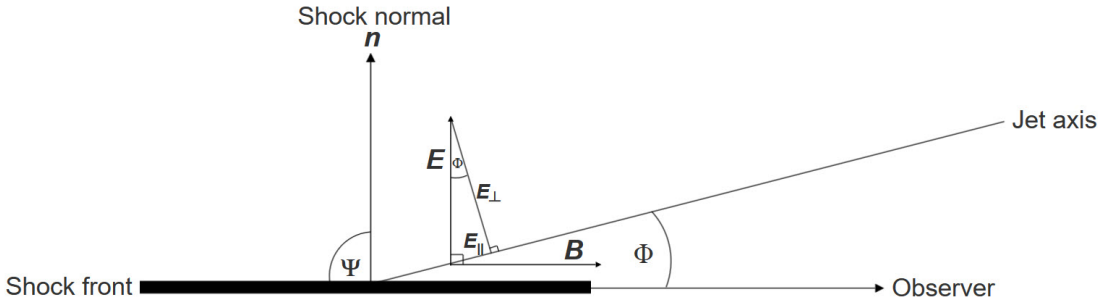

Figure 3.8: Electric field arising from shock compression of a tangled magnetic field for an edge-on shock ($\Psi = 90°$) for a blazar with viewing angle Φ.

electrons being accelerated at the front. The lifetime of the synchrotron electrons for a given frequency ν in GHz in the observer's frame is Hagen-Thorn et al. (2008):

$$t_{\rm sync} = 4.75 \times 10^2 \left(\frac{1+z}{\delta \nu_{\rm GHz} B_{\rm G}^3} \right)^{1/2} \text{ days}, \tag{3.7}$$

where $B_{\rm G}$ is the magnetic field in gauss. Adopting the maximum derived Doppler factor for the observations ($\delta = 22.3$) and $\tau = 10.75$ days in the R–band yields $B = 0.06$ G, in agreement with other estimates of the typical magnetic field in blazars (e.g., Marscher & Gear 1985; Hagen-Thorn et al. 2008; Barres de Almeida et al. 2010; Sorcia et al. 2013). Equation 3.7 also implies that the timescale of variability in the R–band should be a factor of 1.2 greater than the B–band, which is consistent with what is observed (see Table 3.1). Therefore, the polarimetric and multicolor photometric behaviour of PKS 2155–304 during its 2010 outburst is consistent with the characteristics of the shock-in-jet model.

3.4.2 Helical Magnetic Field

An alternative interpretation for the photopolarimetric behaviour of PKS 2155–304 during its 2010 optical flare is that the observed variations are due to changes in the bulk Lorentz factor and viewing angle of a jet with a helical magnetic field geometry.

For a jet pervaded by a helical magnetic field, the observed polarization for

optically thin synchrotron emission[4] can be approximated as (Lyutikov et al., 2005):

$$P = P_{\max} \sin^2 \phi, \tag{3.8}$$

with $P_{\max} \approx 20\%$ and ϕ the viewing angle in the rest frame of the jet, which is related to the observed angle Φ through the Lorentz transformation:

$$\sin \phi = \delta \sin \Phi, \tag{3.9}$$

where δ is the Doppler factor of the jet in the observer's frame. The Doppler factor can be obtained from the observed flux due to a relativistic plasma with bulk Lorentz factor Γ for a smooth, continuous jet:

$$F_\nu = \delta^{2+a} F'_\nu, \tag{3.10}$$

where $F'_\nu \propto \nu'^{-\alpha}$ is the flux in the rest frame of the jet, ν' the frequency in the rest frame of the jet and α is the spectral index. Adopting $\alpha = 1$ (comparable to value derived for the variable component) yields $\delta = \delta_{\max}(F/F_{\max})^{1/3}$, where $\delta_{\max}$ is determined from the definition of the Doppler factor for $\Phi_{\min} = 2.6°$ and $\Gamma = 20$ and $F_{\max}$ is the maximum observed flux in the R–band, and the viewing angle through the definition of the Doppler factor. The polarization degree for a helical magnetic field can then be recovered by substituting δ and Φ into Equation 3.9 and 3.8. The results are displayed in Fig. 3.9 and demonstrate that the helical magnetic field model overestimates the observed polarization degree. Adopting a lower value for the bulk Lorentz factor ($\Gamma = 10.5$[5] Reynoso et al. 2012.) yields a similar result, although the resulting polarization degree is closer to the observed level of polarization. Hence, it is unlikely that the observed polarization of PKS 2155–304 during its 2010 outburst is due to a helical magnetic field.

[4]For the diffuse and reverse-field pinch cases of a filled jet, where the number density of relativistic particles is proportional to the square of the magnetic field (see fig. 11c and 12c in Lyutikov et al. (2005)).

[5]Compare with models of the quiescent emission, which yield $\Gamma = 10$ (Reynoso et al., 2012).

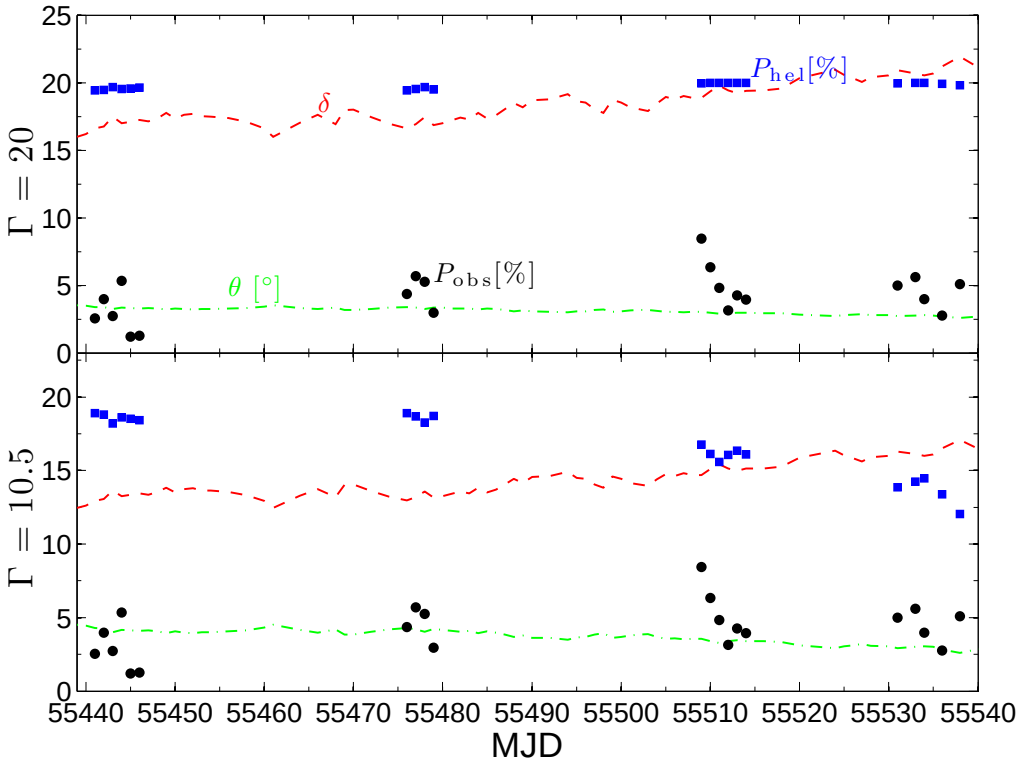

Figure 3.9: Top panel: The Doppler factor δ (red dashed line) and viewing angle θ (green dotted-dashed line) characterizing the optical emission region according to a geometrical interpretation of the long-term optical flux variability for a bulk Lorentz factor $\Gamma = 20$. The observed polarization degree is represented by the black filled circles, while the polarization degree as predicted by the helical magnetic field model is indicated by the blue filled circles. The $\Gamma = 10.5$ case is shown in the bottom panel for comparison. Models of the quiescent emission give $\Gamma = 10$ (Reynoso et al., 2012).

3.5 Conclusions

The BL Lac PKS 2155–304 experienced a prominent optical outburst in 2010, increasing by a factor of 3.7 over roughly 4 months. Analysis of multi-colour photometric measurements and R–band polarization measurements indicate the following:

1. The existence of two distinct states at low and high fluxes. Below 18 mJy, the polarization angle and photometric flux is not correlated, while there is a positive correlation between the polarization angle and flux above 18 mJy ($r = 0.84$).

2. During the high flux state, the polarization angle during the epoch of highest polarization tends to be oriented transverse to the jet direction.

3. The variable emission can be attributed to a variable component with high polarization degree (13.3%) and a constant power-law spectral energy distribution with $\alpha = 1.12 \pm 0.07$.

4. Variations on timescales of days are present for all observation bands, with the minimum timescale of variability increasing with wavelength.

These properties are consistent with the shock-in-jet model, which shows that the observed variability can be explained by an edge-on shock (assuming constant bulk Lorentz factor $\Gamma = 20$). Some parameters derived for the relativistic jet within the shock-in-jet model are $B = 0.06$ G for the magnetic field, $\delta = 22.3$ for the Doppler factor and $\Phi = 2.6°$ for the viewing angle.

Acknowledgements

We gratefully acknowledge the support of the South African National Research Foundation (NRF) and the Department of Science and Technology Department through the South African Square Kilometre Array project. Data from the Steward Observatory's spectropolarimetric monitoring project were used, which is supported by the Fermi Guest Investigator grants NNX08AW56G, NNX09AU10G, NNX12AO93G, and NNX15AU81G. This paper also makes use of SMARTS optical and near-infrared light curves. Special thanks to the referee for her, or his helpful suggestions.

4

A multiwavelength view of the long-term behaviour of PKS 2155–304

Abstract

A study of the long-term multiwavelength variability of the blazar PKS 2155–304 is presented. Radio, optical, optical polarization, high energy (HE) and TeV $\gamma-$ray observations over a roughly 5 year period between July 2009 and December 2014 are analysed in an effort to investigate the variability properties, correlated behaviour, spectrum and magnetic field structure of the source. The optical, $X-$ray and HE flux variations are found to be correlated, while the radio flux lags behind the higher energy emission by ~ 46 d. A structure function (SF) analysis showed that the multiband emission can be described by a power-law spectral density function above a break frequency $\nu_{\rm br}$, with the optical and $X-$ray SF breaking at frequencies corresponding to timescales of 240 d and 24 d, respectively. Below the break frequency, the SF is characterised by white noise. Evidence supporting the presence of a periodic oscillation at a period of roughly 1.8 y is also found.

The optical emission is well-described by a constant spectral component with a power-law spectrum of index $\alpha = -1.13$, consistent with synchrotron emission. An analysis of the optical polarization showed evidence supporting the existence of a persistent polarization component with a polarization degree of 3.4% and a polarization angle of 76°.

4.1 Introduction

Blazars belong to a subclass of radio-loud AGN, where the relativistic jet emanating from the central engine is closely aligned with the line-of-sight to the observer (Urry & Padovani, 1995a). Blazars are known for displaying intense and rapid variability across the electromagnetic spectrum (from radio to γ–ray wavelengths) (Fan & Lin, 2000; H.E.S.S. Collaboration et al., 2007; Kastendieck et al., 2011), along with polarization at radio and optical wavelengths.

The spectral energy distribution (SED) is comprised of two broad emission features. The low-energy component can be found at radio to soft X–ray energies and the high-energy component lies at hard X–ray to γ–ray energies. The prevailing paradigm for blazar emission is that the low energy photons are produced through synchrotron emission and the high-energy photons through Inverse Compton (IC) scattering of the synchrotron photons, in process known as Synchrotron Self Compton (SSC) emission. Alternatively, the seed photons for inverse Compton scattering can be provided by external photon fields in a process referred to as External Compton (EC) emission (H.E.S.S. Collaboration et al., 2009b; Abdo et al., 2010; Reynoso et al., 2012; Chen et al., 2012). Photons external to the emission region can originate from, for example, the accretion disk (Sikora et al., 1994), Broad Line Region (Ghisellini & Madau, 1996) or obscuring torus (Sikora et al., 2002) of the AGN, or come from different locations inside the blazar jet (Ghisellini et al., 2005). Since the same particle population underlies both processes (SSC and EC leptonic jet models; reviewed in Böttcher 2002), correlations between the low and high frequency emission components of the SED are expected.

The foremost competing model for production of the high-energy photons in blazars is the hadronic model, where the high-energy SED component is identified with emission from ultra-relativistic protons (e.g., Mücke & Protheroe 2001b; Mücke et al. 2003). For highly magnetized regions ($\sim$ 30G$-$100 G, Aharonian 2000), direct production of gamma-rays through proton synchrotron emission is possible, while secondary gamma-rays can be generated by protons through their interaction with surrounding matter (Pohl & Schlickeiser, 2000) or photon fields (Mannheim, 1993).

Since the synchrotron emission component is related to the proton population responsible for the high-energy emission (due to relativistic electrons accelerated in conjunction with the protons, or as a result of interactions between the protons and ambient photon fields or matter), correlations between the low- and high-energy emission are also expected for the hadronic model. Nevertheless, leptonic blazar emission models are generally favoured, as both the synchrotron and IC mechanisms are suppressed for protons and the less massive electrons are associated with faster acceleration and cooling times, which is more compatible with the variability timescales observed during blazar flares (Aharonian, 2000).

The broadband emission and variable nature of blazars mean that long term monitoring of the multiwavelength emission (including polarization) can provide insight into the physical processes occurring on a range of timescales. The polarization, as a direct measure of the magnetic field, can help gain insight into the geometry and degree of order of the jet's magnetic field.

The launch of the Fermi gamma-ray telescope, with its all-sky monitor, and publication of the Fermi AGN catalogue (4LAC, Ajello et al. 2020) has given rise to many observation programmes of this kind, which aim to complement the Fermi observations to enable multiwavelength studies of the long term behaviour of blazars. Here, we utilise the results from three such observation campaigns, F-GAMMA, SMARTS and the Steward Observatory's polarization monitoring programme, to study the long term behaviour of PKS 2155–304.

PKS 2155–304 is a nearby ($z = 0.116$), bright southern blazar. As is typical for objects of this type, the source exhibits significant variability from radio to TeV energies, on timescales ranging from minutes (H.E.S.S. Collaboration et al., 2007) to years (Fan & Lin, 2000; Kastendieck et al., 2011). With its extreme observational properties, PKS 2155–304 serves as an ideal candidate for studying the underlying emission processes of blazars. Radio, optical photopolarimetric, high energy (HE) and very high energy (VHE) flux observations spanning roughly 5 years are analysed in order to investigate the variability properties, cross-band correlations, spectrum and magnetic field structure of the source. The paper is

organized as follows: the multiwavelength observations are presented in Section 4.2, followed by an analysis of the variability properties of the source (Section 4.3) and a time-series analysis (Section 4.4). The spectrum of the variable emission component is given in Section 4.5, while the polarization properties of the blazar are presented in Section 4.6. Finally, a discussion of the results is presented in Section 4.7 followed by the conclusions in Section 4.10.

4.2 Observations

PKS 2155–304 is the target of numerous long-term monitoring campaigns. Here, we analyse measurements of the source that were obtained from the F-GAMMA and ATCA (radio), SMARTS (optical) and the Steward Observatory (optical and polarization), *Swift* ($X-$ray), Fermi (high-energy $\gamma-$ray) and H.E.S.S. (very high-energy $\gamma-$ray) observation programmes of the source. A description of the multiwavelength observations from these campaigns are given below.

4.2.1 Radio

Measurements of the total integrated radio intensity of PKS 2155–304 were obtained from the F-GAMMA radio monitoring programme (Fuhrmann et al., 2016; Angelakis et al., 2019), which presents a compilation of AGN detected by the Fermi telescope, and from the monitoring of southern, Fermi detected AGN with the Australia Telescope Compact Array (ATCA), as a member of the ATCA Calibrator Database (Stevens et al., 2012). The F-GAMMA campaign aims to provide multi-frequency radio observations of Fermi-LAT blazars (Atwood et al., 2009). The sample currently includes 65 $\gamma-$ray bright blazars that were observed between 2007 and 2015 with the 100 m Effelsberg (at 2.64, 4.85, 8.35, 10.45, 14.6, 23.05, 32, and 43 GHz) and 30 m IRAM (at 86.2, 142.3, and 228.9 GHz) single dish telescopes. Occasional monitoring was also performed with the APEX 12 m telescope at 345 GHz. Observations of PKS 2155–304 were performed from June 2009 to April 2014, primarily with the 100 m Effelsberg single dish radio telescope, which provided radio intensities

measurements at 28 mm, 36 mm, 60 mm and 11 cm. The fractional errors for the multiband measurements are $\lesssim$4%.

ATCA consists of an array of six 22 m radio telescopes situated in Australia. Observations were made at 7 mm, 15 mm, 4 cm and 16 cm. The ATCA Calibrator Database programme also observes the radio spectra of AGN from the Tracking Active Galactic Nuclei with Austral Milliarcsecond Interferometry (TANAMI) project (Ojha et al., 2010). The fractional errors for the multiband measurements are $\lesssim$3%. The archive is publicly available at `https://www.narrabri.atnf.csiro.au/calibrators/calibrator_database.html`.

4.2.2 Optical

Photometric observations of PKS 2155–304 were obtained from the Small and Moderate Aperture Research Telescope System (SMARTS) and the Steward Observatory's (SO) blazar monitoring programmes.

The Small and Moderate Aperture Research Telescope System monitors bright southern gamma-ray blazars from the Fermi AGN catalogue (Ajello et al., 2020). Observations are performed at optical and near-infrared wavelengths (in the $BVRJK$ bands), using four small telescopes (1.5m, 1.3m, 1.0m and 0.9m). Photometric errors of $\sim$ 0.01 mag are recorded in the optical and 0.02 mag in the IR band, where the sources brightness is <16 mag in the optical and <13 mag in IR. The SMARTS observations are publicly available and can be found at `http://www.astro.yale.edu/smarts/glast/home.php`. The B–, V–, R– and J–band light curves of PKS 2155–304 were obtained between May 2008 and October 2015.

The SO campaign aims to provide photopolarimetric measurements of FERMILAC blazars (Smith et al., 2009). Observations are performed with the 1.54 m Kuiper telescope or the 2.3 m Bok telescope of the observatory. The results of the SO observation programme are publicly available at `http://james.as.arizona.edu/~psmith/Fermi/`. V–band observations of PKS 2155–304 were obtained between October 2008 to July 2015 with typical errors of 0.01 mag.

4.2.3 Polarization

Optical polarization observations of PKS 2155–304 were obtained from the Steward Observatory's blazar monitoring campaign (c.f. Section 4.2.2). Measurements were performed with the spectro-polarimeter, SPOL, which is mounted on either the 1.54 m Kuiper telescope or the 2.3 m Bok telescope of the observatory. SPOL is an imaging spectro-polarimeter consisting of polarizing optics, a spectrograph and a CCD imaging camera (Schmidt et al., 1992). Polarization spectra are produced between 4355 Å – 7195 Å, using a 12.7" × 51.0" grating with a spectral resolution of ~ 4 Å. The B–, V– and R– band polarization were calculated by multiplying the relative Stokes spectrum of the target with the B–, V– and R–band spectral response functions of the telescope. The multiband polarimetric measurements were obtained between October 2008 and July 2015.

4.2.4 $X-$ray

PKS 2155–304 is one of the 23 Fermi-detected gamma-ray sources being monitored by the *Swift* $X-$ray telescope (XRT). The $X-$ray light curve of PKS 2155–304 is measured for photon energies from 0.3–10 keV, from May 2009 to November 2014, with typical fractional errors less than 3%. Measurements are publicly available at `https://www.swift.ac.uk/swift_portal/`. A comprehensive description of the data reduction procedure, as well as a summary of the results can be found in Stroh & Falcone (2013).

4.2.5 High Energy $\gamma-$ray

The Fermi Gamma-ray Space Telescope has been operational since 2008. PKS 2155–304, as one of the primary monitoring targets of the Fermi telescope, is regularly observed in the normal survey mode of the telescope. Its principal scientific instrument is the Large Area Telescope (LAT), which is sensitive to photon energies between 20 MeV and 300 GeV. The LAT observes the entire sky every three hours in survey mode. Observations of the source were retrieved from the Fermi database, which is publicly available at `https://fermi.gsfc.nasa.gov/ssc/data/access/`.

The high energy (HE) light curve was constructed using the Fermi Science Tools, the reduction software developed for the instrument. Only events with the highest probability of being photons and coming from zenith angles $< 100°$ (to avoid the Earth's albedo) were selected for analysis. Photons in the 0.2− 300 GeV energy band were extracted from a region located within a 10° radius of the source position. The energy range is restricted to values exceeding 200 MeV in order to minimize the effect of calibration uncertainties at low energies. An unbinned maximum likelihood technique (Mattox et al., 1996) was used to calculate the integrated $\gamma-$ray flux by modelling the time-averaged photon energy spectrum of the source (above a threshold energy E_0) as a power law of the form $dN/dE = I_0\,(E/E_0)^{-\alpha}$, where $\alpha = -1.83 \pm 1.29 \times 10^{-2}$ represents the spectral index and $I_0 = (64.3 \pm 0.266) \times 10^{-7}$ the flux normalization constant (measured in ph cm^{-2} s^{-1} MeV^{-1}). Galactic diffuse emission, primarily due to cosmic-ray interactions with the interstellar matter, was excluded from the fit by using the model provided by the Fermi Collaboration, which was created based on the Galactic cosmic-ray propagation code GALPROP (Strong et al., 2004b,a). The extragalactic diffuse emission and residual instrumental background was removed by modelling it as an isotropic power-law function. The HE light curve was obtained between April 2009 and December 2015. The sensitivity of the instrument results in an integration time of 7 days.

4.2.6 Very high energy $\gamma-$ray

Very high energy (VHE) measurements of PKS 2155–304 were obtained from the H.E.S.S. Collaboration et al. (2017) study of the long-term $\gamma-$ray variability of the blazar between July 2004 and November 2012. The observations were performed with the High Energy Stereoscopic System (H.E.S.S.), an array of five Imaging Atmospheric Cerenkov Telescopes (IACTs), located in Namibia. Measurements were taken during the first phase of H.E.S.S., when the instrument consisted of four 12 m diameter telescopes. The VHE light curve was constructed by modelling the time-averaged photon energy spectrum as a log-parabola of the form $dN/dE \propto E^{-a-b\log E}$, above a threshold energy of 200 GeV, where a is the best-fit power-law index and

Table 4.1: Observation Summary

Campaign	Telescope Diameter	Spectral Range	Type	Date Range
F-GAMMA	30 m	28, 36, 60, 110 mm		28 Jun. 2009 – 05 Apr. 2014
ATCA	6 × 22 m	7, 15, 40, 160 mm		24 Apr. 2009 – 19 Nov. 2014
SMARTS	1.5, 1.3, 1.0, 0.9 m	*B, V, R*	Photometry	20 Apr. 2009 – 03 Dec. 2014
SO	1.54, 2.3 m	4355 − 7195 Å	Polarimetry	25 Jul. 2009 – 28 Dec. 2014
Swift-XRT	∼ 10 cm	0.3 – 10 keV		28 May 2009 – 09 Nov. 2014
Fermi LAT	0.72 m	200 MeV − 0.3 GeV		04 Apr. 2009 – 25 Dec. 2014
H.E.S.S.	4 × 12	> 200 GeV		24 Jun. 2009 – 15 Nov. 2012

b is the curvature index. The total integrated $\gamma-$ray intensity per night was derived using a separate log-parabola fit of the spectrum for each year. The energy spectrum is characterized by a mean spectral index $\langle a \rangle = 0.3209 \pm 0.017$ and $\langle b \rangle = 0.164 \pm 0.114$ for the curvature index. The total observation time (328 h) yielded a total detection significance exceeding 300σ.

A summary of the multiwavelength observation campaigns used in this analysis of PKS 2155–304 is presented in Table 4.1. The columns list: (1) the name of the observation programme or telescope, (2) telescope diameter, (3) the spectral range or observing band covered by each campaign, (4) the type of observations and (5) the date range.

4.2.7 Results

The multi-wavelength light curves of PKS 2155–304 are displayed in Fig. 4.1. The corresponding photopolarimetric observations in the R–band are shown in Fig. 4.3. Figure 4.1 shows that the source exhibits a number of interesting features during the observation period. The largest VHE flare occurred during 2009, peaking at $[1.8 \pm 0.1] \times 10^{-10}$ ph cm^{-2} s^{-1} on MJD = 55035, followed by another flare on MJD = 55039, which peaked at $[1.3 \pm 0.1] \times 10^{-10}$ ph cm^{-2} s^{-1} (shaded region 1). Both flares develop over ~ 5 days. The latter flare is accompanied by an increase in the polarization degree and the detection of quasi-periodic oscillations in the polarized flux (Pekeur et al., 2016), as well as moderate amplitude fluctuations in the HE and optical band.

During 2010 PKS 2155–304 experienced its most prominent optical outburst, reaching a peak brightness of 31.1 ± 0.1 mJy in the R–band on MJD = 55538, coinciding with a moderate increase in flux at high energies and in the radio band, and seemingly correlated behaviour in the $X-$ray band (shaded region 2). The optical flare peaks after roughly 114 days, followed by a decrease over 15 days, before showing another rise in flux 4 days later. The HE and radio flux peak roughly 95 days after the optical emission and the shape of the HE and radio flares are much broader than the optical flare. If the radio to HE emission is correlated, then this might indicate that the optical flare continued to develop outside of the optical observation window.

A photopolarimetric analysis of the source during this period revealed the existence of two distinct optical polarization states at low and high fluxes (Peceur et al., 2020). A positive correlation was observed between the polarization angle and flux for the high state, while the polarization angle exhibited a broad range of values with no clear relation to the flux for the low state. The observed variability during the high flux state was attributed to a shock that is seen nearly edge-on.

Moderate $X-$ray and optical flares are detected in 2012. The $X-$ray flare develops over ~ 134 days, reaching a peak flux of 5.5 ± 0.1 ph s^{-1} on MJD = 56181. The optical flare develops over ~ 228 days, reaching a peak flux of 15.8 ± 0.04 mJy on MJD = 56182. The flares are accompanied by a minor increase in the HE and radio flux (shaded region 3).

The most prominent HE and $X-$ray flares are observed during 2014, peaking at 12.1 ± 0.1 ph s^{-1} on MJD = 56799 and $[7.2 \pm 0.4] \times 10^{-7}$ on MJD = 56793, respectively. The flares develop over roughly 40 days and are accompanied by a moderate optical flare, which develops over ~ 99 days, reaching a peak brightness of 16.4 ± 0.04 mJy on MJD = 56804 (shaded region 4).

Finally, we observe that the multiband light curves appear to show flaring activity roughly every two years.

The time dependence of the radio spectral index, $\alpha_{\rm radio}$, as derived from the F-GAMMA and ATCA observations is displayed in Fig. 4.2. The shaded regions

highlight periods when the radio emission becomes more optically thin (decreasing $\alpha_{\rm radio}$), while the optical flux is decreasing, and periods when the optical flux increases while the radio emission becomes more opaque (increasing $\alpha_{\rm radio}$).

Figure 4.3 shows that optical flares typically occur during periods when the polarization angle experiences large swings ($\gtrsim 80°$), such that the polarization angle is aligned with the jet direction ($\theta_{\rm jet} \sim 150° - 160°$).

4.3 Fractional Variability Amplitude

To estimate the intrinsic variability of the source at different wavelengths the fractional variability amplitude, $F_{\rm var}$, (Edelson et al., 1990) is calculated. The fractional variability amplitude characterizes the variance of a given light curve when the contribution from the measurement errors have been subtracted and is defined as,

$$F_{\rm var} = \sqrt{\frac{\sigma^2 - \overline{\sigma_{\rm err}^2}}{\overline{x}^2}}, \tag{4.1}$$

where $\overline{x}$ is the mean of the light curve, σ^2 is the variance of the light curve and $\overline{\sigma_{\rm err}^2} = \frac{1}{N}\sum_{i=1}^{N}\sigma_{{\rm err},i}^2$ is the mean-square-error of the measurements. The uncertainty is given by:

$$\mathrm{err}(F_{\rm var}) = \sqrt{\left(\frac{1}{2N}\frac{\overline{\sigma_{\rm err}^2}}{F_{\rm var}\overline{x}^2}\right)^2 + \left(\sqrt{\frac{\overline{\sigma_{\rm err}^2}}{N}}\frac{1}{\overline{x}}\right)^2} \tag{4.2}$$

(Vaughan et al., 2003).

The results for the different bands are listed in Table 4.2. The columns are (1) observation band, with the optical and polarized flux in the R–band and (2) fractional variability amplitude $F_{\rm var}$ (%). Figure 4.4 illustrates the relationship between the fractional variability amplitude and spectral band. The figure indicates that the variability amplitude may be linearly related to $\log\nu$ in the radio to $X-$ray regime.

There are few caveats in the cross-band comparison. The HE flux was binned in one week intervals compared to one day for the other bands. This means that any fast variations will be smoothed out, leading to an underestimate of $F_{\rm var}$. Furthermore, undersampling of the VHE light curve could also lead to an underestimation of $F_{\rm var}$.

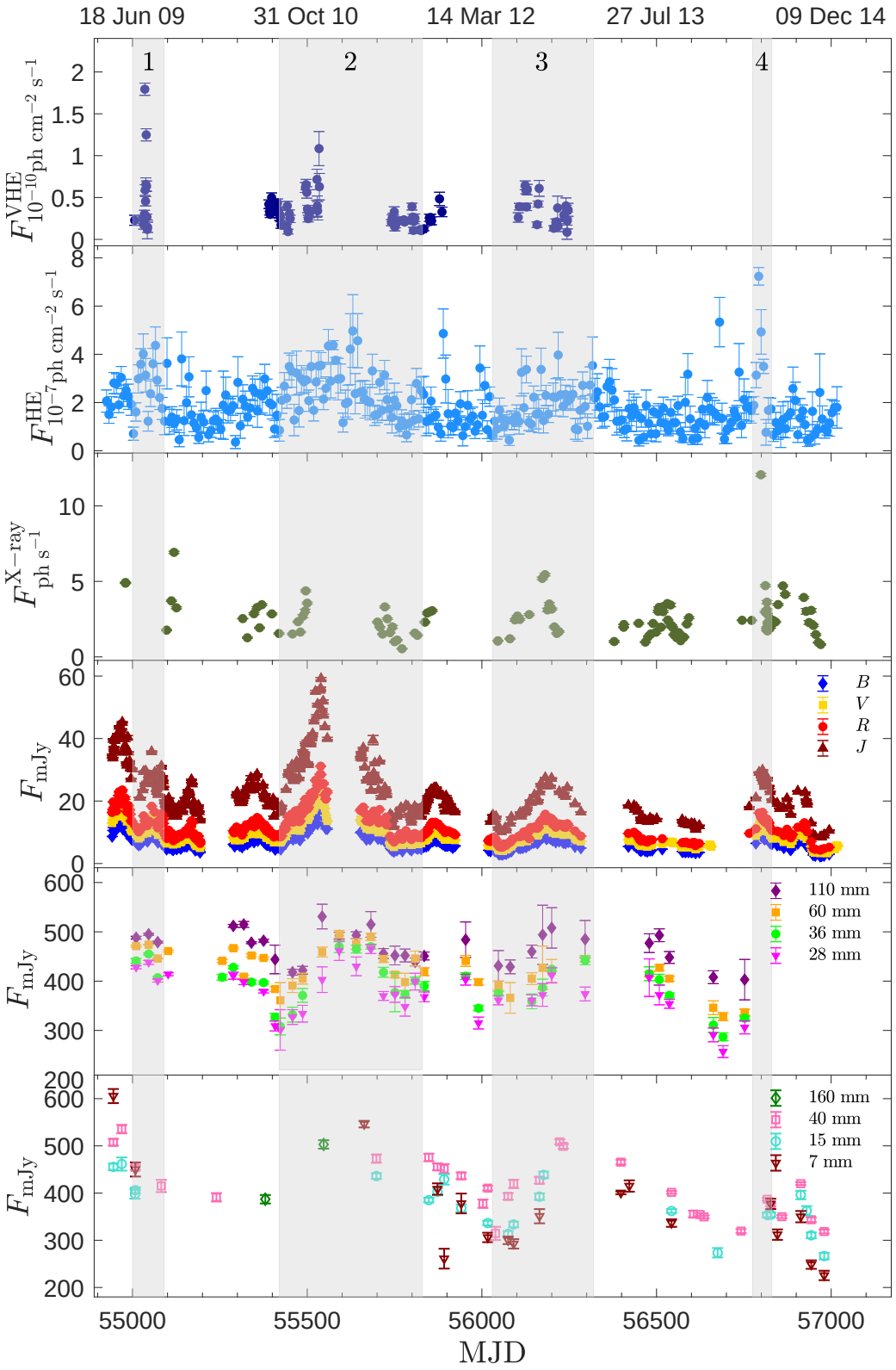

Figure 4.1: The multiwavelength variability of PKS 2155–304 between April 2009 and December 2014. From top to bottom: The VHE flux above 200 GeV, the HE flux above $>$ 200 MeV, the $X-$ray light curve, for photon energies ϵ from 0.3 – 10 keV, extinction-corrected multiband ($BVRJ$) light curves and radio intensities at 110 mm, 60 mm, 36 mm and 28 mm for the F-GAMMA and 160 mm, 40 mm, 15 mm and 7 mm for the ATCA observations. The shaded regions highlight possible correlated behaviour between the spectral bands.

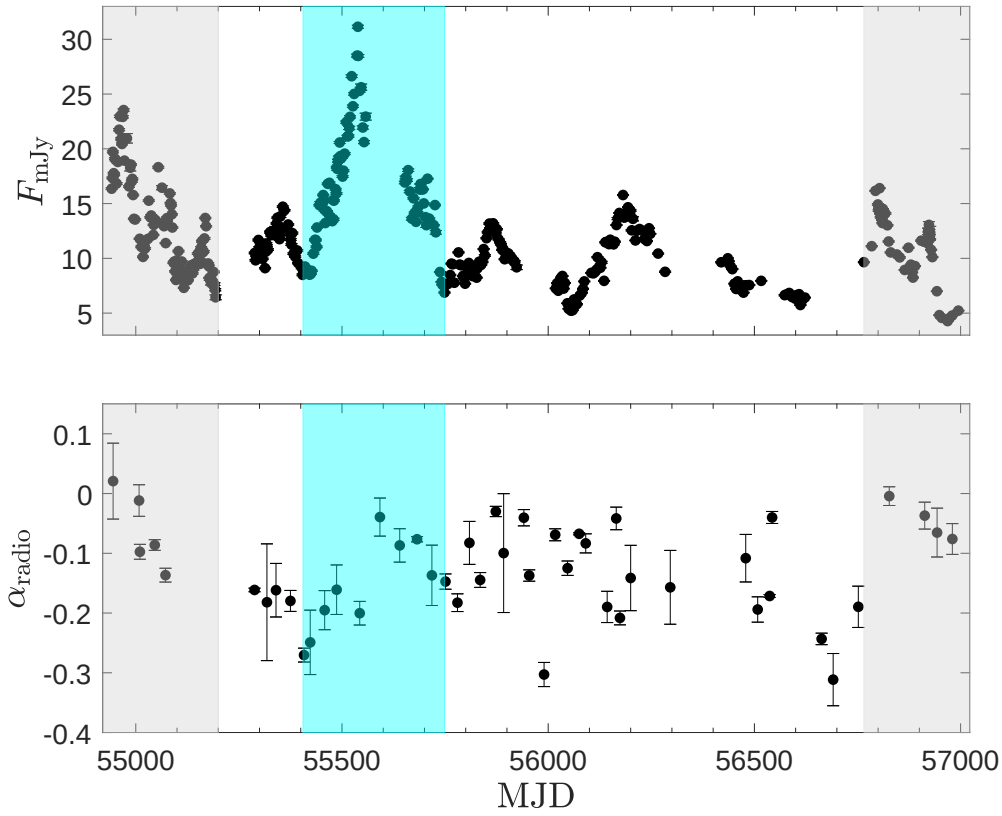

Figure 4.2: *R*–band light curve of PKS 2155–304 from 2009 to 2014 (top) and the radio spectral index (α), as derived from the multiband radio measurements displayed in Fig. 4.1, during the same period (bottom). The shaded regions highlight periods when the optical flux decreases while the radio emission becomes more optically thin, or increases while the radio emission becomes more opaque.

Table 4.2: Fractional variability amplitude of PKS 2155–304 between 2009 and 2014 from VHE to radio wavelengths.

(1) Band	(2) F_{var} (%)
VHE	68.9 ± 1.9
HE	42.8 ± 1.8
$X-$ray	57.3 ± 0.2
Optical	36.8 ± 0.1
Polarized Flux	68.0 ± 0.5
Radio	9.4 ± 0.6

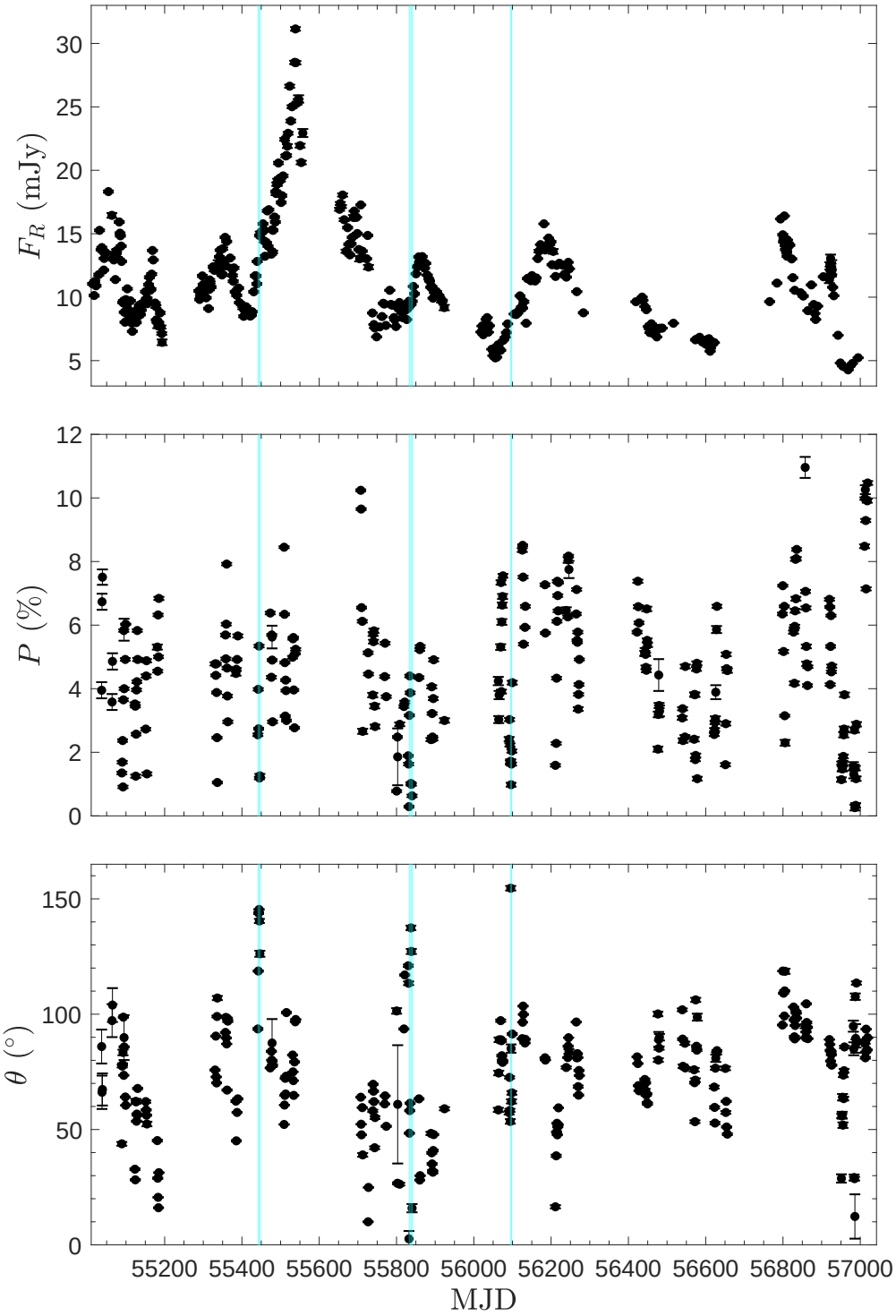

Figure 4.3: *R*–band photopolarimetric observations of PKS 2155–304 from 2009 to 2014. The panels from top to bottom are: the photometric flux, polarization degree and polarization angle. The cyan regions indicate where the polarization angle is roughly parallel to the position angle of the jet ($\theta_{\rm jet} \sim 150^\circ - 160^\circ$).

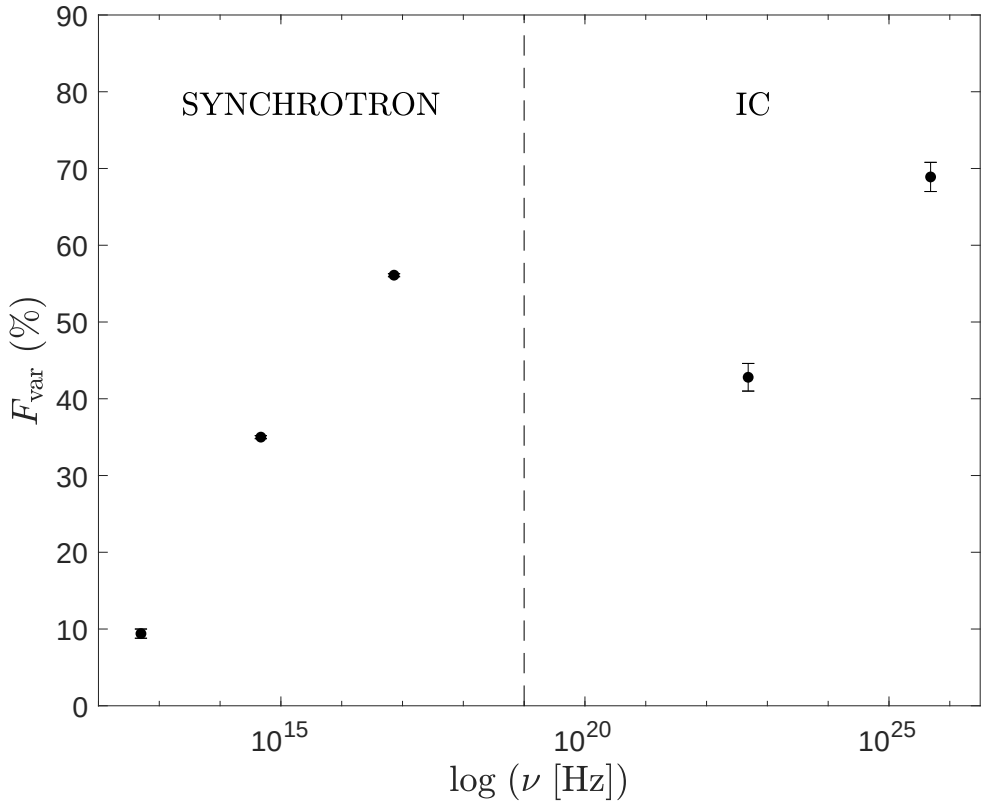

Figure 4.4: Fractional variability amplitude as a function of frequency. The dashed line separates the synchrotron and IC regimes.

4.4 Time Series Analysis

4.4.1 The Z–Transformed Discrete Correlation Function

The multiwavelength light curves of PKS 2155–304 (Fig. 4.1) demonstrate possible correlated behaviour for the VHE, HE, $X-$ray , optical and radio variabilities (shaded regions). A measure of the correlated behaviour between the bands is given by the Z–transformed discrete correlation function (ZDCF; Alexander 1997). The ZDCF utilizes Fisher's z-transform of the correlation coefficient and provides an improved way of estimating the discrete correlation function for sparse, unevenly sampled light curves (see Alexander 1997 for a detailed discussion).

The ZDCF between the HE, $X-$ray , 60 mm and 110 mm light curves and the optical light curve are displayed in Fig. 4.5. The ZDCF for the radio bands relative to the optical band show negative lag (~ -45 days at 60 mm and ~ -47 days at 110 mm) with strong significance for the 60 mm band ($r \sim 0.7$) and

marginal significance for the 110 mm band ($r \sim 0.5$), such that the radio flux lags behind the optical. The lag of the HE and $X-$ray bands are consistent with zero ($\tau = 1.5^{+3.0}_{-1.0}$ and $\tau = 3.3^{+3.6}_{-1.1}$ days, respectively), with marginal significance ($r \sim 0.5$ and $r \sim 0.4$, respectively). This result is consistent with the findings of Rajput et al. 2021 who observed correlated flux variations in the IR, optical, and HE emission of the source during epoch 4 (see Fig. 4.1).

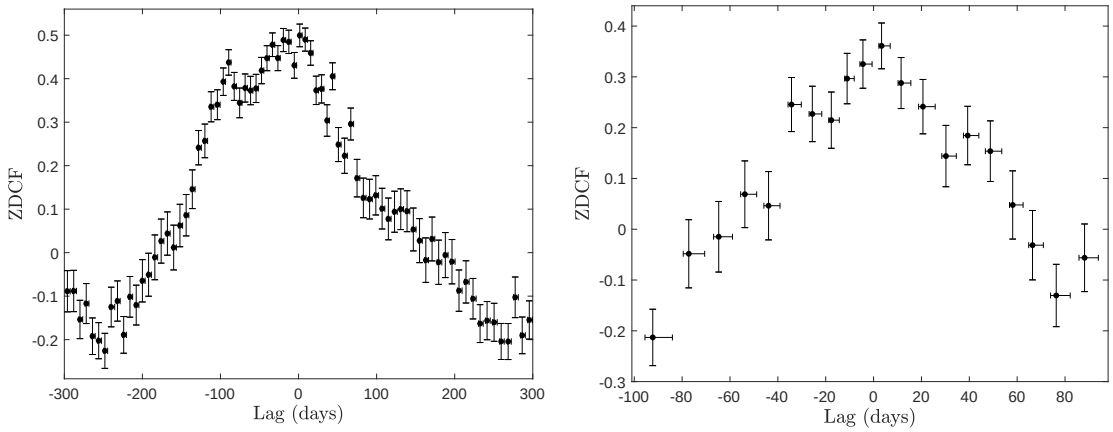

(a) High energies: The lag $\tau = 1.5^{+3.0}_{-1.0}$ days with correlation coefficient $r = 0.50$.

(b) $X-$ray : The lag $\tau = 3.3^{+3.6}_{-1.1}$ days with $r = 0.39$.

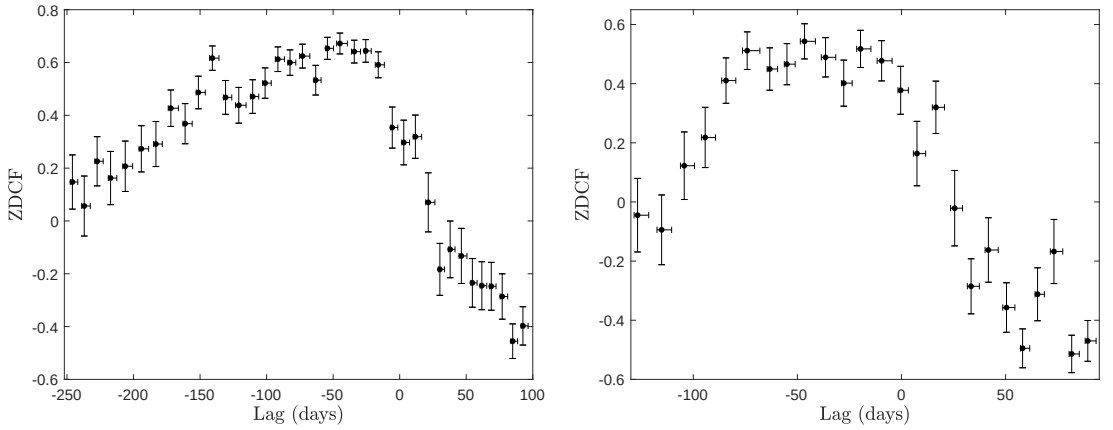

(c) 60 mm Radio: The lag $\tau = -44.9^{+5.5}_{-2.5}$ days with $r = 0.67$.

(d) 110 mm Radio: The lag $\tau = -46.6^{+5.2}_{-2.0}$ days with $r = 0.54$.

Figure 4.5: The Z-Transformed Discrete Correlation Function of the HE, $X-$ray , 60 mm and 110 mm light curves of PKS 2155–304 with respect to the optical flux. Note that negative lag means that e.g. the radio flux lags behind the optical flux.

4.4.2 The Structure Function

The structure function (SF, Hughes et al. 1992; Lainela & Valtaoja 1993) measures the mean value of the flux variance of a light curve and is defined as $\mathrm{SF}(\tau) = \langle [x(t) - x(t+\tau)]^2 \rangle$, where $x(t)$ represents the flux values separated by time interval τ. The SF was computed for the radio to HE observation bands (the VHE flux was excluded due to having too few observations). The structure functions of the radio, optical, $X-$ray and HE light curves of PKS 2155–304 are displayed in Fig. 4.6.

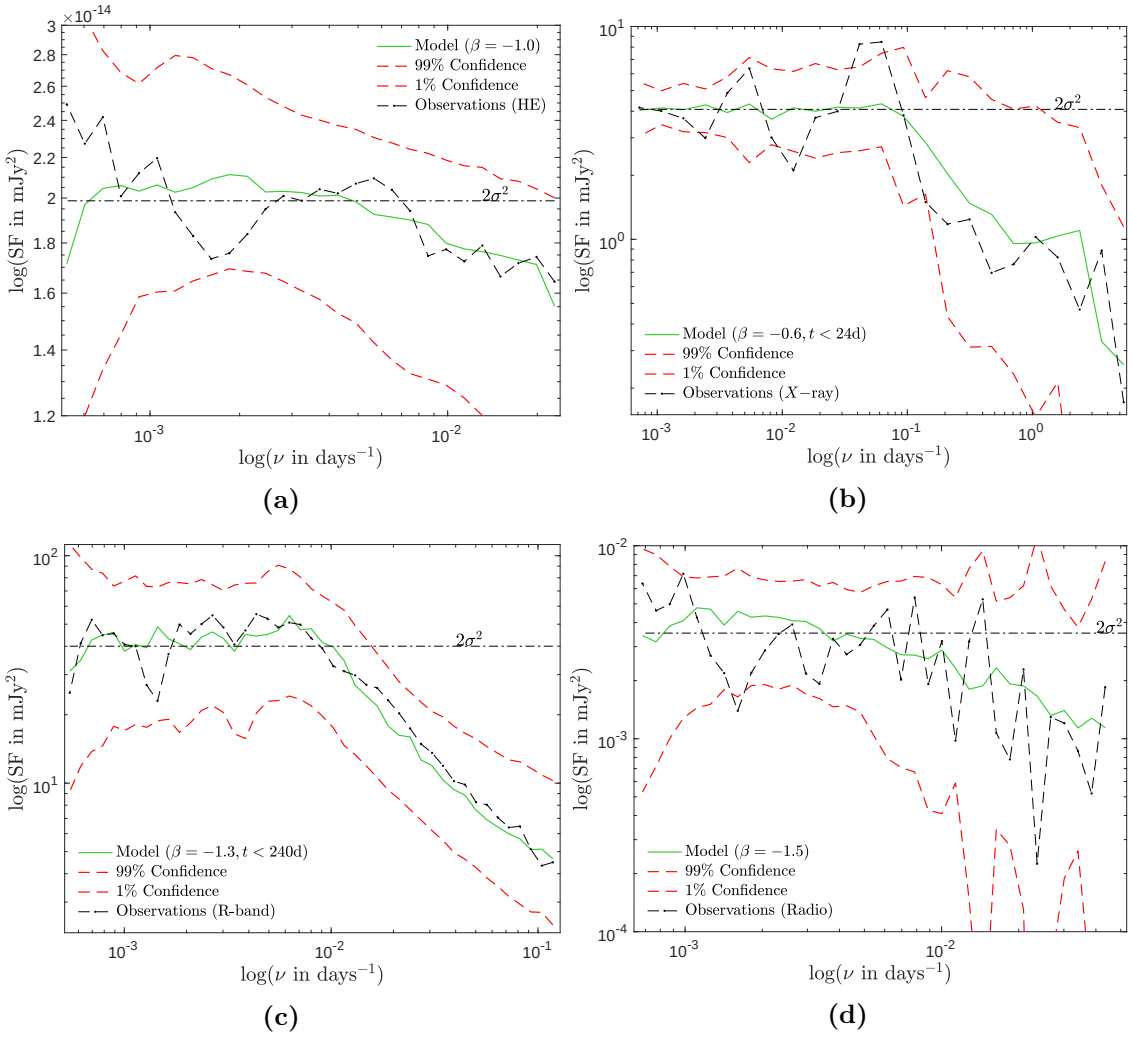

Figure 4.6: The structure function (SF) of the (a) HE, (b) X–ray, (c) Optical (R–band) and (d) Radio light curves of PKS 2155–304, plotted on a loglog scale using equal frequency bins. The SF corresponding to the best fit power law PSD function is represented by the solid line. The upper and lower 99% confidence level of the probability density function for each frequency bin are given by the dashed lines. For lags longer than the longest correlation timescale, the SF for the $X-$ray and optical bands plateaus at an amplitude equal to twice the variance of the light curve (dashed line).

Table 4.3: Fitted parameter values of the PSD function for the Radio, Optical, $X-$ray and HE structure functions. The best-fit values for each band are listed in columns (4) & (5).

(1) Band	(2) $-\beta$	(3) $t_{\rm br}$ (d)	(4) $-\beta^{\rm BF}$	(5) $t_{\rm br}^{\rm BF}$ (d)
HE	$0.6-1.8$ (0.1)	–	1.0	–
$X-$ray	$0.1-1.0$ (0.1)	$10-30$ (1)	0.6	24
Optical	$0.8-2.0$ (0.1)	$200-350$ (10)	1.3	240
Radio	$0.6-1.8$ (0.1)	–	1.5	–

The shape of the SF is modelled by assuming a power law noise continuum with a power spectral density function PSD $\propto \nu^{\beta}$ above a characteristic break frequency $\nu_{\rm br}$ for the $X-$ray and optical bands a single power law at HE and radio energies. The effects of sampling and measurement noise was included by generating 5000 random light curves with the same mean, variance and sampling rate as the observations. Following Kastendieck et al. (2011), the best-fit PSD was computed by using a forward-folding technique for each value of β and $\nu_{\rm br}$ (see columns (3) & (4) in Table 4.3) and a maximum likelihood estimator is used to determine the best-fit parameter values for the PSD. The fitted values and best-fit parameters are listed in Table 4.3. The columns are (1) the observation band, (2) the fitted range of spectral indices and (3) the fitted range for the turnover timescale $\left(t_{\rm br}=\frac{1}{\nu_{\rm br}}\right)$, with the increments for both parameters displayed in brackets. The best-fit parameters are recorded in columns (4) and (5).

The fitted models and variance plateaus are superimposed on each structure function (see Fig. 4.6). The $X-$ray and optical SFs are best-described by a power law noise model with spectral indices $\beta=-0.6$ & -1.3, respectively. The break timescale is $t_{\rm br}=24$ d for the $X-$rays and 240 d at optical energies. The best fit models at HE and radio energies are described by a single power law with $\beta=-1.0$ and -1.5, respectively. Plotting the model spectral index as a function of frequency (see Fig. 4.7) and separating the synchrotron and inverse Compton energy regimes displays possible evidence of a relationship between β and the spectral band ($\propto \log\nu$) for the synchrotron regime.

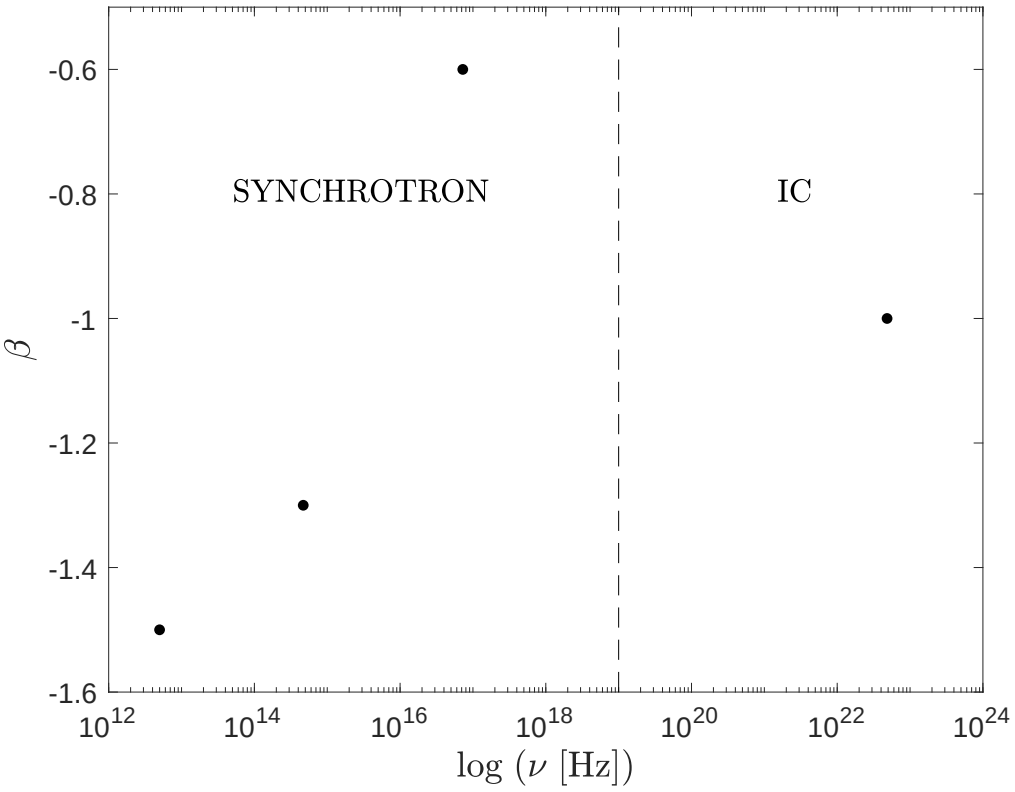

Figure 4.7: The spectral index of the fitted SF as a function of frequency. The dashed line separates the synchrotron and IC regimes.

Further inspection of the HE, optical and radio SFs shows the presence of a prominent dip at $\nu \sim 1.4 \times 10^{-3}$ days^{-1}, the signature of a possible periodic oscillation. Specifically, the minimum value of the HE and radio feature correspond to $\tau = 1.71$ y and the optical feature to $\tau = 1.89$ y. The three timescales agree within the width of the feature (~ 100 d) and are consistent with the approximately 2 y periodic flaring behaviour observed for the multiband light curves (see Fig. 4.1). The radio feature is statistically significant above 99% confidence (see Fig. 4.6d), while re-binning the optical SF in the J–band in equal frequency and lag bins (see Fig. 4.8) shows that it is significant at and above 99% confidence, respectively.

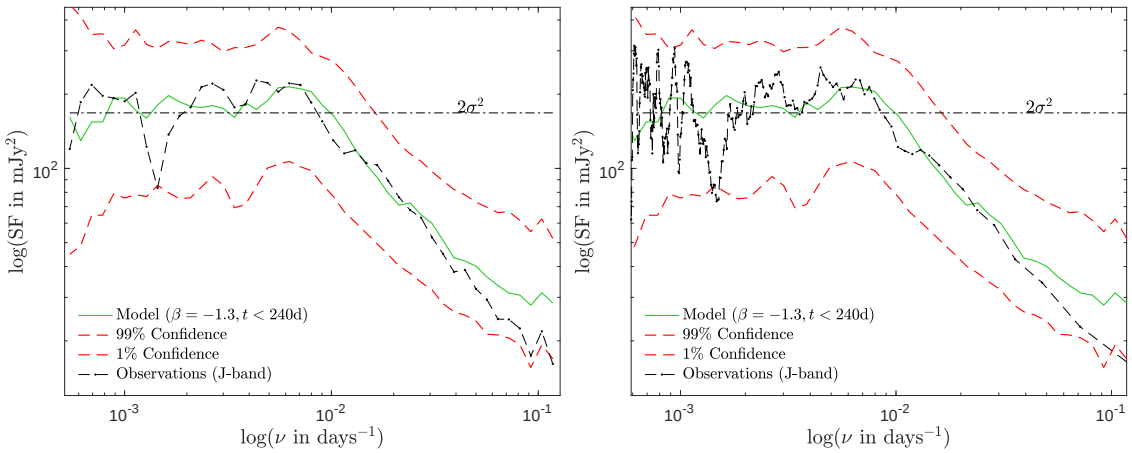

Figure 4.8: The J–band structure function of the PKS 2155–304 for equal frequency bins (left) and lag bins (right). The best fit model (solid line) and the lower 99% confidence levels (dotted-dashed line) are superimposed.

4.5 Spectral Energy Distribution of the Variable Emission

Following Hagen-Thorn & Marchenko (1999), the observed emission is separated into a variable component and a constant component, $F = F_{\rm var} + F_{\rm cons}$. The ratio of the fluxes for different pairs of spectral bands are given by:

$$\left(\frac{F_\nu}{F_{\nu_0}}\right)^{\rm var} = \alpha_{\nu\nu_0}, \tag{4.3}$$

where the superscript denotes the variable component, ν_0 denotes the reference spectral band and $\alpha_{\nu\nu_0}$ is the spectral index of the variable component. If $\alpha_{\nu\nu_0}$ does not vary with frequency then these flux ratios are constant and

$$F_\nu = \alpha_{\nu\nu_0} F_{\nu_0} + \left(F_\nu^{\rm cons} - \alpha_{\nu\nu_0} F_{\nu_0}^{\rm cons}\right). \tag{4.4}$$

Equation 4.4 demonstrates that a linear relationship will be seen when plotting F_ν against F_{ν_0} for several bands. Therefore, the presence of a linear relationship for the flux-flux diagrams across multiple bands indicates that the relative SED of the variable emission component is unchanged. The spectral index of the variable emission component is then given by the slope of the best fit line for $\log \alpha_{\nu\nu_0}$ against $\log \nu$.

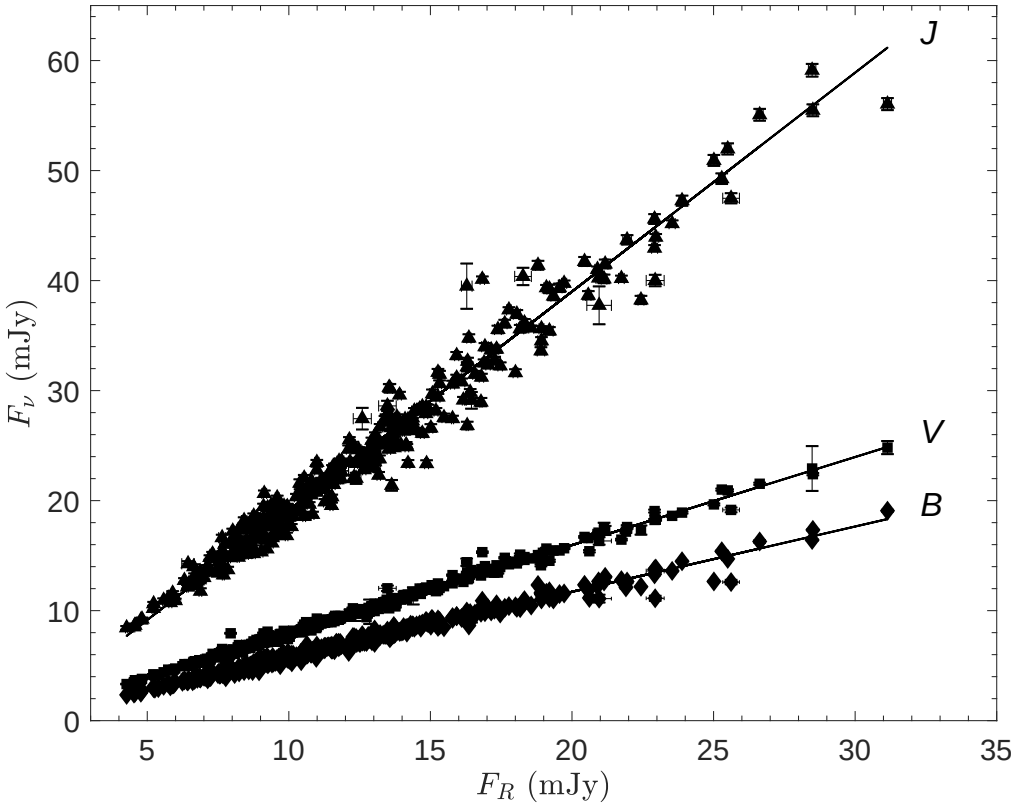

Figure 4.9: The B–, V– and J–band fluxes relative to the R–band flux of PKS 2155–304 between 2009 and 2014. The best fit lines are superimposed.

The B–, V– and J–band fluxes relative to the R–band flux is shown in Fig. 4.9. The orthogonal regression method is used to calculate the best fit lines. The flux ratio between the specified pairs of optical bands are given by the slopes of the best fit lines. Fig. 4.9 shows that a linear relationship is seen for the flux-flux diagrams. Hence, it can be concluded that the relative SED of the variable component remains constant. The emission spectrum of the variable component is presented in Fig. 4.10. The figure shows that the SED is well represented by a power-law $F_\nu \propto \nu^\alpha$ with slope $\alpha = -1.13 \pm 0.07$, in agreement with synchrotron source emission.

4.6 The Persistent Polarization

If the jet possesses an underlying persistent polarization component, the mean position of the Stokes or relative Stokes parameters will be displaced from the origin of the Stokes plane. The relative Stokes parameters, q and u, of the optical

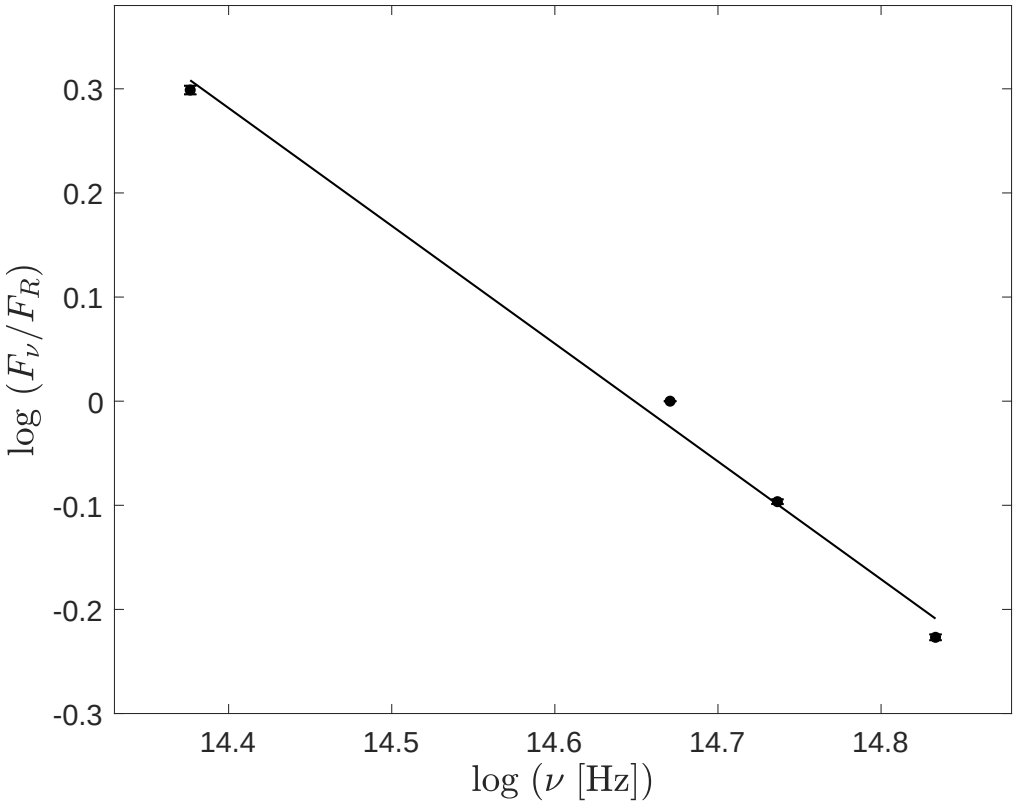

Figure 4.10: Relative SED of the variable emission component of PKS 2155–304. The best fit line is superimposed, with slope $\alpha = -1.13 \pm 0.07$.

polarization of PKS 2155–304 during the five years of observation are illustrated in Fig. 4.11. The mean values are $\langle q \rangle = [-3.0 \pm 0.17] \times 10^{-2}$ and $\langle u \rangle = [1.6 \pm 0.15] \times 10^{-2}$. The resulting polarization degree $p_c = 3.4 \pm 0.2\%$, with a dispersion of $\sigma_{p_c} = 3.7\%$. The polarization angle $\theta_c = 76^\circ \pm 1.4^\circ$.

The optical polarization degree of the persistent component is similar to the polarization degree seen from the resolved radio core $p_{\rm jet} \sim 3\%$ (Piner et al., 2008, 2010) and the polarization angle lies roughly transverse to the position angle of the blazar's parsec-scale radio jet ($\theta_{\rm jet} = 150^\circ - 160^\circ$). This implies that the magnetic field associated with the persistent optical polarization is aligned with the jet direction.

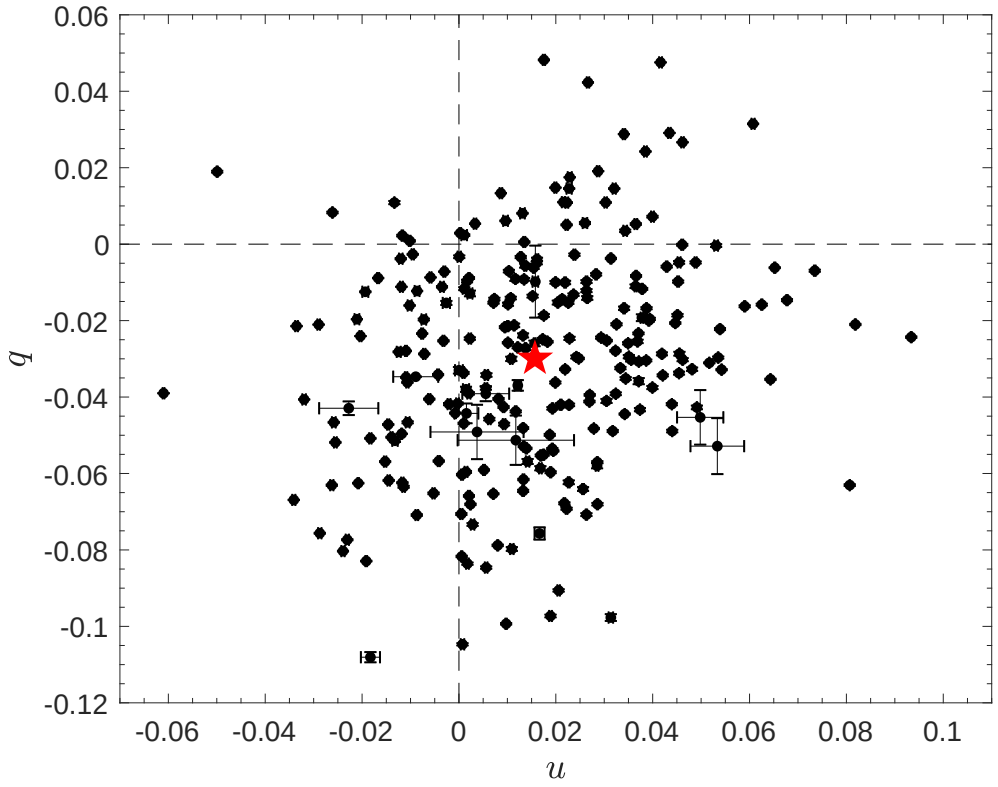

Figure 4.11: The relative Stokes parameters q and u of PKS 2155–304in the R–band. The mean values $\langle q \rangle = (-3.0 \pm 0.17) \times 10^{-2}$ and $\langle u \rangle = (1.6 \pm 0.15) \times 10^{-2}$, are represented by the star. The associated polarization degree is $p_c = 3.4 \pm 0.2\%$ and the polarization angle is $\theta_c = 76 \pm 1.4°$.

4.7 Discussion

Long term radio, photopolarimetric, high energy and very high energy observations of PKS 2155–304 covering ~ 5 years have been presented here. The light curves reveal the complex multiband flaring behaviour of the blazar, including evidence of cross-band correlations. Flares are observed on a variety of timescales, from 5 days, 40 days, ~ 3 months and ~ 7.5 months, with flaring activity seemingly occurring roughly every two years. These aspects are explored in more detail in the sections that follow.

4.7.1 Variability

A comparison of the fractional variability amplitude of PKS 2155–304 at different photon energies demonstrates that the source is more variable at higher energies (see Table 4.2). The variability amplitude rises with frequency in both the synchrotron

and IC regime, in agreement with the results of Chevalier et al. 2019, which reproduced the behaviour through a time-dependent, one-zone synchrotron self-Compton model. Note that Chevalier et al. 2019 has roughly 3 years of multiband observations overlapping with this study.

4.7.2 Cross-Band Correlations

Models of the broad band SED of PKS 2155–304 have shown that the emission is well-described by SSC radiation from a single emission zone (H.E.S.S. Collaboration et al., 2005a; Abdalla et al., 2020; Rajput et al., 2021). The electron population responsible for the production of the optical to soft $X-$ray photons also produces the hard $X-$ray to VHE photons. Correlations between the low- and high-energy emission of the source are therefore expected. These cross-band correlations were investigated by computing the ZDCF, which indicates that the radio photons lag behind the optical, while the optical, $X-$ray and HE $\gamma-$ray photons appear to be co-evolving. The time lag between the radio and optical emission can be explained within the synchrotron framework, where radiation at lower frequencies take longer to reach the optically thin state. Hence, the optical and $X-$ray emission are expected to peak before the radio emission. The nearly zero lag between the optical, $X-$ray and HE emission may indicate that the emission is produced by the same population of electrons, in a nearly cospatial location, as predicted by SSC models (e.g. H.E.S.S. Collaboration et al. 2017; Chevalier et al. 2019; Rajput et al. 2021).

Provided that the large lag seen for the radio emission is due to opacity effects, the radio emission should be optically thick during the rise of a given flare and optically thin during its decline. For a given outburst, imagine an event that creates a population of energetic electrons emitting synchrotron radiation. These electrons occupy an emitting region, which undergo dynamical evolution, e.g. an expanding shock propagating along the jet. The total flux will increase due to the expanding source. Once the source becomes optically thin, the total flux will peak and start to decrease (as long as the energy injection has stopped). Hence, at radio frequencies, the source will start off optically thick ($\alpha_{\rm radio} > 0$) during the rise of the flare,

then become optically thin during its decline ($\alpha_{\rm radio} < 0$). Figure 4.2 shows that the radio emission becomes more optically thin (decreasing spectral index) during periods when the optical flux decreases and more opaque (increasing spectral index) during periods when the optical flux increases. A possible explanation is that the observed radio emission is a superposition of the variable emission component and an optically thin persistent jet (refer to Section 4.6).

4.7.3 Structure Function

The variable nature of the long term ($\mathcal{O}(5$ yrs)) light curve of PKS 2155–304 is investigated through the structure function, which measures the variability power of the source as a function of timescale. The shape of the structure function can help gain insight into the underlying physical processes that give rise to the flux variations. Figure 4.6 shows that the multiband structure functions of PKS 2155–304 have the characteristic shape of a power-law at high frequencies, flattening below a break frequency $\nu_{\rm br}$ for the optical and $X-$ray bands. Significant indications of a periodic oscillation are also observed at radio and optical energies, at $> 99\%$ confidence.

At optical energies, the spectral index of the best-fit model is $\beta = -1.3$, consistent with the findings of Kastendieck et al. 2011 ($\beta = -1.6^{+0.4}_{-0.2}$). The spectral index at high energies, $\beta = -1.0$, agrees with the value derived by the H.E.S.S. Collaboration et al. 2017 ($\beta = -1.2^{+0.2}_{-0.3}$). The break frequency (or alternately, the break timescale $t_{\rm br} = \frac{1}{\nu_{\rm br}}$) for the SF at optical and $X-$ray energies correspond to timescales of 240 d and 24 d, respectively. Below the break frequency, for lags longer than the longest correlation timescale, the SF is characterised by white noise around a plateau equal to twice the amplitude of the light curve variance (Hughes et al., 1992). The absence of a noise plateau for the radio and HE (H.E.S.S. Collaboration et al., 2017) bands might indicate that longest correlation timescale has not yet been reached and that a longer observation period is required.

As well as displaying power-law behaviour, the HE, optical and radio structure functions all reveal the presence of a dip at lag $\tau \sim 1.8$ y (see Fig. 4.6a, 4.6c and 4.6d). This is evidence of the presence of a periodic oscillation for the source.

Further evidence of a periodic oscillation at this timescale was presented by Chevalier et al. 2019. The authors reported a possible periodicity at ~ 1.9 y based on a Lomb-Scargle periodogram analysis of the Fermi-LAT and R–band SMARTS light curves of the source spanning a roughly 5.5 y period, for which there is a ~ 3 y period overlapping with this study.

The presence of red noise behaviour and a potential periodicity in the long term multiband lightcurves of PKS 2155–304, demonstrate the complexity of the processes that drive the variability. While the exact nature of the variations in blazar jets are not yet fully understood, the observed variability is typically attributed to either self-organised criticality (SOC, Bak et al. 1987), which gives rise to power-law noise behaviour, or periodicities driven by jet dynamics (Rieger, 2004). A general motivation for SOC in blazars is given by models of SOC in astronomical shocks (Malkov et al., 2000) and compact plasmas (Sivron, 1998). The impact of SOC is expected to be constrained by the effective size of the emitting region. Hence, the power-law noise behaviour, driven by SOC, is expected to disappear at longer timescales. Within the framework of SOC, the break timescale is associated with the "memory" of the system, since at timescales longer than $t_{\rm br}$ the properties of the emission process become uncorrelated from its past. Causality constrains the size of the emission region as $l \lesssim c t_{\rm br} \delta/(1+z) = 1.24 \times 10^{19}$ cm $= 4.0$ pc for the optical emission and 1.24×10^{18} cm $= 0.4$ pc for the $X-$ray emission.

It has been postulated that periodic modulations in blazars arise due to periodic changes of the Doppler effect. One possible reason for such a periodic modification of the Doppler effect is precession of the jet, which can arise e.g. due to the existence of a supermassive black hole (SMBH) binary system at the centre of these AGN (see e.g. Doğan et al. 2015, and references therein). However, jet precession is expected to occur on timescales that are too long ($\sim 10^6$ y, King et al. 2008; Nixon & King 2013). Another possible explanation involves magnetohydrodynamic instabilities, or the rotation of a twisted jet giving rise to different jet regions changing their orientation, and therefore their relative Doppler factors (see e.g. Raiteri et al. 2017, and references therein).

4.8 Magnetic Field Structure

The SED of the variable component is consistent with a power-law with index $\alpha = -1.13$, as is expected for synchrotron emission. Since the relative SED of the variable emission is constant, this indicates a quasi-steady state of the emission between the injection rate and radiative losses. Following Hagen-Thorn et al. 2008, the synchrotron lifetime for a given frequency ν in GHz is defined as:

$$t_{\rm sync} = 4.75 \times 10^2 \left(\frac{1+z}{\delta \nu_{\rm GHz} B_{\rm G}^3} \right)^{1/2} \text{ days}, \tag{4.5}$$

For $t_{\rm sync}$ equal to the variability timescale in the R–band (~ 5.5 days)[1], and using the Doppler factor derived for PKS 2155–304 in Peceur et al. 2020 ($\delta \sim 22.3$), Equation 4.5 yields $B = 0.09$ G for the magnetic field and an upper limit to the size of the optical emission region $l \leq ct_{\rm sync}\delta/(1+z) = 3.8 \times 10^{17}$ cm $= 0.12$ pc.

We can gain insight into the magnetic field structure by calculating the coherence length of the magnetic field at large scale $l_B = (\kappa \Pi_0/\sigma_{p_c})^{-2/3} l$, where $\Pi_0 = \dfrac{\beta+1}{\beta+\frac{5}{3}}$ is the polarization degree for a uniform field, κ is the intrinsic polarization degree of the source, σ_{p_c} is the dispersion of the constant polarization component and l is the size of the emission region. Assuming κ is the polarization degree of the stable component ($= 3.4\%$) and $\sigma_{p_c} = 3.7\%$, the dispersion of the constant component (derived in Section 4.6), we obtain $l_B = 4.8 \times 10^{17}$ cm $= 0.16$ pc, similar to the upper limit derived for the optical emission region.

This scale can be compared with shock-in-jet models (e.g. Marscher & Gear 1985; Hughes et al. 1985; Cawthorne & Cobb 1990), wherein the interday variability is linked to the distance travelled along the jet by the relativistic shock, D, during the time taken between two extrema of the light curve, Δt (Rees, 1967; Qian et al., 1991):

$$\Delta t = \left(\frac{D(1+z)}{c \beta_s \delta_s \Gamma_s} \right), \tag{4.6}$$

[1]The timescale of variability of the light curves is defined as $\tau = dt/\ln(F_1/F_2)$, where dt is the time interval between flux measurements F_1 and F_2, with $F_1 > F_2$ (Burbidge et al., 1974). The possible timescales τ_{ij} are computed for any pair of observations with $|F_i - F_j| > \sigma_{F_i} + \sigma_{F_j}$ (Hagen-Thorn et al., 2008). The minimum timescale of variability is defined as $\tau = \min\{\tau_{ij}\}$, where $i = 1...N-1$, $j = i+1, ...N$ and N is the number of observations.

where β_s is the speed of the shock, δ_s its Doppler factor and Γ_s its Lorentz factor. Using $\beta_s \sim 1$ (Giroletti et al., 2004; Piner et al., 2008, 2010; Baring et al., 2016), $\delta_s \sim 22.3$, $\Gamma_s \sim 3$ (Giroletti et al., 2004; Piner et al., 2008) and $\Delta t \sim 3$ d, the timescale between extrema for the optical polarization degree, yields $D \sim 4.7 \times 10^{17}$ cm = 0.15 pc. The distance travelled by the shock is therefore very similar to the coherence length of the magnetic field, l_B, which indicates that there might be a link between the interday changes of the polarization degree and the spatial changes in the magnetic field.

4.9 Radiative Age

The variable optical emission spectrum of PKS 2155–304 (see Fig. 4.10) shows evidence of spectral steepening at the high frequency tail of the spectrum. Inspection of the spectrum shows that it appears to curve between the V– and R–band, around 5.1×10^{14} Hz. Since the variable optical emission spectrum represents emission from all of the outbursts detected for the source over ~ 5.5 y, it can be inferred that the emission region is replenished by a continual injection of new relativistic particles with a power-law energy distribution. For the continuous injection model, the turnover frequency $\nu_{\rm br}^{\rm sy}$ is depended on the time elapsed since the source was formed (Murgia et al., 2011):

$$\tau_{\rm sync} = 1590 \frac{\sqrt{B}}{(B^2 + B_{\rm IC}^2)\sqrt{\nu_{\rm br}^{\rm sy}(1+z)}}, \tag{4.7}$$

where $B_{\rm IC} = 3.25(1+z)^2$ is the inverse Compton equivalent magnetic field representing inverse Compton losses; with the synchrotron age $\tau_{\rm sync}$ in Myr, the magnetic field in μG and the break frequency $\nu_{\rm br}^{\rm sy}$ in GHz. Using the magnetic field strength value derived from the variability timescale at optical wavelengths $B = 0.09$ G and 5.1×10^{14} Hz for the break frequency results in a radiative age $\tau_{\rm sync} = 7.4 \times 10^{-8}$ Myr $= 27.1$ d.

4.10 Summary

A multiwavelength view of the long-term behaviour of the blazar PKS 2155–304 have been presented. Radio, optical photopolarimetric, HE and VHE observations over a roughly 5 year period were studied in an effort to investigate the variability properties, cross-band correlations, spectrum and magnetic field structure of the source. The results are summarised below.

1. The variability amplitude of the source displays an increasing trend with energy, for the radio to $X-$ray regime and the HE to VHE regime, respectively. The largest variations ($F_{\rm var} \gtrsim 68\%$) are detected for the VHE flux and optical polarization.

2. Correlated variations were identified for the optical, $X-$ray and HE $\gamma-$ray light curves, while the radio light curve lagged behind the higher energy emission by $\tau \sim 46$ d. The nearly zero lag between the synchrotron (radio to X–ray) and IC (HE) emission components might be indicative of a nearly cospatial emission region, with emission from the same population of electrons, as predicted by SSC models. The large lag at radio bands was attributed to opacity effects, where radiation at lower frequencies take longer to reach the optically thin state. This conclusion is supported by the evolution of the radio spectral index during the rising and decaying phases of flares, with the radio emission becoming more optically thin during periods when the optical flux decreases and more opaque during periods when the optical flux increases.

3. The multiband structure functions of PKS 2155–304 were found to follow a power-law spectral density function, with the optical and $X-$ray SF flattening below a break frequency $\nu_{\rm br}$, at timescales corresponding to 240 d and 24 d, respectively. The characteristic power-law behaviour observed for the structure function can be interpreted as the effect of self-organised criticality (SOC), for which the break timescale is linked to the "memory" of the system. The break timescale corresponds to an upper limit of 4.0 pc for the optical emission region

size and 0.4 pc for the $X-$ray emission region size.

Indications of a 1.8 y periodicity were found at $> 99\%$ confidence, consistent with the 1.9 y periodicity detected by Chevalier et al. 2019.

4. Examination of the variable optical emission showed that it can be described by a single variable component with a constant spectral index $\alpha = -1.13$, consistent with optically thin synchrotron emission.

5. A persistent optical polarization component with a polarization degree of 3.4% and polarization angle of 76° was identified. The coherence length, l_B, of the stable polarization component was determined as 0.16 pc. This was compared to the distance travelled by a relativistic shock over 3 days, $D = 0.15$ pc. The similar values may indicate a connection between the interday variations of the polarization degree and the spatial changes in the magnetic field.

Acknowledgements

We gratefully acknowledge the support of the South African National Research Foundation (NRF) and the Department of Science and Technology Department through the South African Square Kilometre Array project.

Data Availability Statement

ATCA radio observations are available at `https://www.narrabri.atnf.csiro.au/calibrators/calibrator_database.html`. The SMARTS optical and infrared data archive can be found at `http://www.astro.yale.edu/smarts/glast/home.php`. The Steward Observatory's photopolarimetric data repository is available at `http://james.as.arizona.edu/~psmith/Fermi/`. and X–ray and high energy gamma-ray observations of PKS 2155–304 can be found at the Swift and Fermi archives at `https://www.swift.ac.uk/swift_portal/` and `https://fermi.gsfc.nasa.gov/ssc/data/access/`, respectively. Data for the source can be accessed using 2155–304 or PKS 2155–304 as the unique identifier.

5
Summary and Conclusions

In this thesis I've made use of optical polarization and multiwavelength observations of the blazar PKS 2155–304 across roughly 5.5 years to probe the variability of the source on short (intra-day to daily), intermediate (days to months) and long timescales (months to years). By studying variability on different timescales, jet regions of various scales can be probed.

The short timescale variability of the blazar was investigated by monitoring the intra-day variability of the optical polarization from 25 – 27 July in 2009 (Chapter 2, Pekeur et al. 2016). The observations revealed, for the first time, evidence for the existence of quasi-periodic oscillations in the polarization of an AGN. Two periodic components were identified at $T \sim 13$ min, detected at $> 99.7\%$ significance, and $T \sim 30$ min, detected at $> 99\%$. Overlapping gamma-ray measurements of the source showed that it was in an active state, displaying two very high energy $\gamma-$ray flares. The first contemporaneous optical polarization observations of PKS 2155–304 during an active state was recorded for the second flare. The coincidence of the QPOs with the late stage of post flare activity of the first gamma-ray flare, or the transition between the two gamma-ray flares could suggest that the QPOs are part of a longer-lived phenomenon within the AGN jet. A possible explanation for the quasi-periodic oscillations is a relativistic shock propagating down an inhomogenous jet containing quasi-helical structures in the magnetic field or electron density.

Another interpretation for such short-lived QPOs is turbulence behind the shock. The largest eddies will contribute the most to the variability, with the period depending on their turnover times. The presence of multiple turbulent cells behind the same shock could offer a possible explanation for the existence of more than one QPO in the same light curve.

The intermediate variability of PKS 2155–304 was studied by examining its optical polarization and total brightness over a roughly 4 month period in 2010 (Chapter 3, Peceur et al. 2020). During this time the source experienced its most prominent optical flare in the ~ 5.5 years of observation. Analysis of the $BVRJ$ photometric observations and R–band polarization observations showed the existence of two distinct polarization states at low and high fluxes. At low fluxes (< 18 mJy), there is no clear relation between the polarization angle and photometric flux, while a positive correlation is seen for the polarization angle and photometric flux at high fluxes (> 18 mJy). For the high flux state, the polarization angle tends to be oriented perpendicular to the jet axis when the polarization is at its highest. The variable emission during the high flux state can be explained by a variable component with high polarization degree (13.3%) and a constant power-law radiation spectrum with $\alpha = 1.12 \pm 0.07$. The spectral and polarization behaviour were modelled in the context of the shock-in-jet model, where the observed variability is attributed to a nearly edge-on shock. The model provides a good match to the data for the following parameters: $B = 0.06$ G for the magnetic field, $\delta = 22.3$ for the Doppler factor and $\Phi = 2.6^{\circ}$ for the viewing angle. The Doppler factor derived for PKS 2155–304 spans a wide range, from $\sim 6 - 58$ (e.g. Urry et al. 1997; Ghisellini & Tavecchio 2008; Gaur et al. 2017). Some of the most recent estimates are $\delta = 35$ (Chevalier et al., 2019) and $\delta = 22$ (Lucchini et al., 2019), hence in close agreement with my finding. Estimates for the magnetic field give $B = 0.01 - 0.2$ G (Urry et al., 1997; H.E.S.S. Collaboration et al., 2012; Chevalier et al., 2019). My estimate of the magnetic field falls within the range of previously estimated values.

An investigation of the long-term behaviour of the blazar was performed by studying radio, optical, optical polarization, X–ray and $\gamma-$ray observations of the

source over a roughly 5.5 year period (Peceur et al., in prep). The study found that the variability amplitude of the source increases with energy for the radio to $X-$ray regime (synchrotron SED peak) and the HE to VHE regime (Inverse Compton SED peak), respectively. The discrete correlation function between the optical light curve and the other multiband light curves showed that the optical, X-ray and HE $\gamma-$ray light curves are consistent with zero lag. However, the radio light curve was found to lag behind the higher energy emission by roughly 46 days. The lag seen between the radio and higher energy light curves can be explained by opacity effects due to synchrotron radiation. The nearly zero lag between the optical and X–ray (synchrotron SED peak) and high energy (Inverse Compton SED peak) emission components indicates that the emission can be attributed to the same electron population.

The nature of the brightness variations was studied by calculating the structure function for the time lag. The multiband structure functions follow a power-law spectral density function, with the optical and $X-$ray structure functions flattening above a break timescale of 240 days and 24 days, respectively. The index of the power-law is –1.5 for the radio structure function, –1.3 for the optical, –0.6 for X–rays and –1.0 at high energies. The power-law behaviour was interpreted as the effect of self-organised criticality (SOC). The effect of SOC is limited by the effective size of the emitting region and the power-law noise behaviour driven by SOC is expected to disappear at longer timescales. The break timescale is therefore linked to the "memory" of the system. The structure functions also show indications of a 1.8 yr periodic outburst, found at $> 99\%$ confidence.

The *BVRJ* photometric fluxes showed that the variable component of the optical emission is well-described by a power-law radiation spectrum of index -1.13, which was found to be constant over the ~ 5.5 years of observation. This behaviour implies optically thin synchrotron emission from a power law electron distribution. The optically thin synchrotron emission implies an energy spectrum with an index of -3.26.

Finally, the optical polarization shows evidence for the existence of a constant polarization component with a polarization degree of 3.4% and a polarization angle of 76°. This implies that the magnetic field of the persistent polarization component is oriented at 166°, which is nearly aligned with the jet axis seen in VLBI (oriented at $150° - 160°$). The coherence length of the magnetic field at large scale, the characteristic length over which the magnetic field is stable, is 0.16 pc. The coherence length of the magnetic field is similar to the upper limit derived for the optical emission region (0.12 pc) and for the distance travelled by a shock traversing the jet (0.15 pc). This indicates a link between the interday changes of the polarization degree and the spatial changes in the magnetic field (e.g. Barres de Almeida et al. 2010; Fraija et al. 2017).

My findings of the long term variability of the multiwavelength and optical polarization indicate the existence of a stable polarization component that is most likely associated with the large scale magnetic field of the AGN jet. The coherence length of this large scale magnetic field is comparable to the distance travelled by a shock in the jet between polarization extrema. This suggests a connection between changes in the polarization due to a shock traversing the jet and changes in the large scale magnetic field. The results of intermediate variability of the multiband optical light curves and optical polarization show that the variable emission during the high optical flux state have a high polarization degree and power-law radiation spectrum and can be explained by a nearly edge on shock. The polarized emission can therefore be explained by a two-component model. Two component models have also been successful at explaining the observed polarization in other blazars (e.g. Hagen-Thorn et al. 2008; Sorcia et al. 2013; Gaur et al. 2014; Bhatta et al. 2015). These models attribute the polarization to a constant component with a lower polarization degree, superposed with a variable component exhibiting a higher polarization degree, consistent with my findings.

The short term variability of the polarization shows that quasi-periodic variations can exist on intraday timescales, where the periodic behaviour can be explained by a shock moving through quasi-helical structures in the magnetic field or electron

density. The periods of the oscillations ($T \sim 13$ min and $T \sim 30$ min) are comparable to the 15 min periodicity observed in the optical light curve of the blazar S5 0716+714 (Rani et al., 2010). This finding further bolsters the evidence for the presence of fast QPOs in blazars.

Taken together the results of my analysis suggest that two components are responsible for the observed emission. A stable emission component with a low polarization degree and a magnetic field that lies roughly parallel to the direction of the jet, where the magnetic field has a characteristic scale of 0.16 pc, and a variable emission component with a high polarization degree and power-law radiation spectrum. The variable component can be attributed to a relativistic shock traversing the jet on timescales ranging from days to months, where intraday quasi-periodic oscillations can arise due to turbulence behind the shock or the shock encountering quasi-helical structures in the magnetic field or electron density. The structure function analysis of the long term multiband light curves demonstrates that there is power in the variable emission component on all time scales up to the break timescale, above which white noise dominates. The timing characteristics suggest that the emission is dominated by correlated noise processes. The structure function also indicates that the variable component experiences a major outburst roughly every 1.8 years. Long timescale periodicities of the order of a few years have been observed for PKS 2155–304 before (Fan & Lin, 2000; Zhang et al., 2017). However, Covino et al. 2020 and Ait Benkhali et al. 2020 found no firm evidence for year-long QPOs at gamma-ray and optical energies. A power-law radiation spectrum is observed over roughly 5.5 years for the variable optical emission. This implies that the energy distribution is the same over the ~ 5.5 year period, indicating that the mechanism for generating the population is the same in all cases and with similar energetics and initial conditions (or is not sensitive to initial conditions).

Blazars typically do not show consistent behaviour for flux correlations between different energy bands (Aleksić et al., 2015c; Acciari et al., 2020; Zhang et al., 2021; MAGIC Collaboration et al., 2023). Both correlated (H.E.S.S. Collaboration et al., 2009a,b; Rajput et al., 2021) and uncorrelated flux variations have been observed

for PKS 2155–304 (Wierzcholska et al., 2019). Here, I find that the long term light curves of PKS 2155–304 display correlated flux variations between different energy bands. The nearly zero lag observed for the optical, $X-$ray and high energy light curves suggests that the same particle population is responsible for the low and high energy emission, in agreement with Synchrotron Self Compton models.

In conclusion, the three studies paint a consistent picture of the source wherein there exists a large scale magnetic field, leading to a persistent polarization component. The variable emission of the source on intermediate timescales and short term timescales can be described by a shock moving through the jet. On timescales of days to months a nearly edge on shock explains the variable emission. On intraday timescales, quasi-periodic arises due to the shock encountering quasi-helical structures in the jet or due to turbulence behind the shock.

6
Future Work

Polarization properties of a sample of blazars

The results of my study suggests that two components exist for PKS 2155–304, which have a relationship with the geometry of the jet. More comprehensive studies of a large sample of objects would allow us to explore if this is a universal property of the blazar population.

The polarization features of blazars may be spatially resolved through Very Long Baseline Interferometry. Such studies reveal that the polarization angle of the observed blazars tend to be aligned with the local jet direction, while a minority displays a polarization angle that is orthogonal to the local jet direction (Gabuzda et al., 2000; Gabuzda & Chernetskii, 2003).

An alignment of the polarization angle with the jet direction is an indication of a transverse magnetic field. Transverse magnetic field structures are generally attributed to transverse (or oblique) shocks propagating in the jet. Shocks partially order an initially tangled magnetic field by compressing the magnetic field. For a transverse shock, the plane of compression is parallel to the shock front. The polarization angle will therefore be oriented along the jet. This scenario applied to a sample of blazars would present a large scale test of the shock-in-jet model that

was used in my analysis of the intermediate variability of the photopolarimetric light curves of PKS 2155–304.

Polarization angles that are orthogonal to the jet-axis are attributed to velocity shear between the jet and the surrounding medium.

Large-scale helical magnetic fields can also explain the bimodal distribution of the polarization angle. Depending on the viewing angle and pitch angle distribution, the net magnetic field seen by the observer can appear as either transverse or longitudinal. However, if the field strength of the transverse or toroidal component is similar to or stronger than the poloidal component in the frame of the jet, geometric aberration will enhance the emission components close to the observer's line-of-sight and it is more likely that the toroidal magnetic field component will dominate the polarized emission. The resulting polarization angle in the frame of the observer then appears to be oriented along the jet axis. A helical magnetic field therefore provides a natural explanation for the observed tendency of the polarization angle to be aligned with the jet direction; as well as the smaller percentage of sources which display a transverse offset between the polarization angle and the jet.

The long term monitoring of the polarization of a sample of blazars can help establish what the properties of the stable polarization component is for the blazar population, from which the underlying magnetic field structure can be inferred. The characteristics of the persistent polarization can then be compared to resolved radio jet (by using archival observations or through AGN monitoring programs such as MOJAVE, Lister & Homan 2005; Homan & Lister 2006) to try to ascertain if there is a preferential orientation of the polarization with respect to the jet direction. This can be achieved through a study of the statistical properties of the optical polarization of the 66 blazars from the Steward observatory's monitoring campaign of Fermi AGN. Such a study would be a follow up to this thesis to explore the relationship between quiescent components and jet geometry.

Furthermore, the existence of blazar monitoring programs such as SMARTS and the Steward observatory means that we have comprehensive multiband photopolarimetric data for a large sample of blazars. This opens the door to studies of

the polarization during flaring and quiescent blazar states. As was demonstrated by the study of the intermediate variability of PKS 2155–304, the polarization can help constrain the number of emission components contributing to the observed emission and can be used to model its origin.

The polarization observations performed by the Steward observatory include polarization spectra. This means that it is possible to study the evolution of the frequency dependent polarization (FDP) for a sample of blazars for flaring and quiescent periods and identify any trends for the blazar class. The FDP can also be used to constrain the nature of the source emission. Holmes et al. 1984 (see also Valtaoja et al. 1991) demonstrated this by attributing the observed frequency dependence of the optical polarization to a transverse shock that travels down the jet.

Finally, studying the behavior of blazars during periods of enhanced activity, when the mechanisms behind the observed radiation are intensified, offers a means to explore the source physics of these objects. Target of Opportunity optical polarization measurements (including high resolution polarization spectra) can be obtained with the South African Large Telescope (SALT), which would allow a view of the polarization during flaring states.

Technical Acknowledgements

N.W.P. expresses sincere appreciation for the generous support received from the South African National Research Foundation (NRF), the Department of Science and Technology (DST) through the South African Square Kilometre Array Office, the Science Faculty at the University of Cape Town (UCT) and the Centre for Space Physics at North-West University (NWU). Special thanks to Markus Böttcher for engaging in thought-provoking discussions. Many thanks to Stephen Potter for his collaboration on the observation and reduction of the polarization measurements from the South African Astronomical Observatory (SAAO). Thanks to the SAAO for providing telescope time. N.W.P extends her gratitude to the H.E.S.S. Collaboration for taking the TeV $\gamma-$ray measurements. In addition, data from the following observation campaigns were used: ATCA radio observations [1], the SMARTS optical and infrared data archive [2], the Steward Observatory's photopolarimetric data repository [3], Swift X–ray observations [4] and Fermi high energy gamma-ray observations [5].

[1] available at `https://www.narrabri.atnf.csiro.au/calibrators/calibrator_database.html`

[2] available at `http://www.astro.yale.edu/smarts/glast/home.php.`

[3] available at `http://james.as.arizona.edu/~psmith/Fermi/`

[4] available at `https://www.swift.ac.uk/swift_portal/`

[5] available at `https://fermi.gsfc.nasa.gov/ssc/data/access/`

References

Abdalla H., Aharonian F., Ait Benkhali F., H. E. S. S. Collaboration et al., 2019, MNRAS, 482, 3011

Abdalla H., Adam R., Aharonian F., et al., 2020, A&A, 639, A42

Abdo A. A., Ackermann M., Agudo I., et al., 2010, ApJ, 716, 30

Acciari V. A., Aliu E., Arlen T., et al., 2011a, ApJ, 738, 25

Acciari V. A., Aliu E., Arlen T., et al., 2011b, ApJ, 738, 169

Acciari V. A., Ansoldi S., Antonelli L. A., et al., 2020, ApJS, 248, 29

Aharonian F. A., 2000, , 5, 377

Aharonian F. A., 2004, Very high energy cosmic gamma radiation : a crucial window on the extreme Universe

Ahnen M. L., Ansoldi S., Antonelli L. A., et al., 2017, A&A, 603, A31

Ait Benkhali F., Hofmann W., Rieger F. M., et al., 2020, A&A, 634, A120

Ajello M., Angioni R., Axelsson M., et al., 2020, ApJ, 892, 105

Albert J., Aliu E., Anderhub H., et al., 2007, ApJ, 669, 862

Aleksić J., Alvarez E. A., Antonelli L. A., et al., 2012, A&A, 542, A100

Aleksić J., Ansoldi S., Antonelli L. A., et al., 2015a, MNRAS, 451, 739

Aleksić J., Ansoldi S., Antonelli L. A., et al., 2015b, A&A, 576, A126

Aleksić J., Ansoldi S., Antonelli L. A., et al., 2015c, A&A, 576, A126

Aleksić J., Ansoldi S., Antonelli L. A., et al., 2015d, A&A, 578, A22

Alexander T., 1997, in Maoz D., Sternberg A., Leibowitz E.-M., eds, Astronomical Time Series Vol. 218, Astrophysics and Space Science Library. p. 163

Andruchow I., Combi J. A., Muñoz-Arjonilla A. J., et al., 2011, A&A, 531, A38

Angel J. R. P., Stockman H. S., 1980, A&ARv, 18, 321

Angelakis E., Fuhrmann L., Myserlis I., et al., 2019, A&A, 626, A60

Arlen T., Aune T., Beilicke M., et al., 2013, ApJ, 762, 92

Atwood W. B., Abdo A. A., Ackermann M., et al., 2009, ApJ, 697, 1071

Bak P., Tang C., Wiesenfeld K., 1987, , 59, 381

Baring M. G., Böttcher M., Summerlin E. J., 2016, MNRAS, 464, 4875

Barres de Almeida U., Ward M. J., Dominici T. P., et al., 2010, MNRAS, 408, 1778

Begelman M. C., Fabian A. C., Rees M. J., 2008, MNRAS, 384, L19

Bhatta G., Goyal A., Ostrowski M., et al., 2015, ApJLetters, 809, L27

Blandford R. D., Rees M. J., 1974, MNRAS, 169, 395

Błażejowski M., Blaylock G., Bond I. H., et al., 2005, ApJ, 630, 130

Blinov D., Pavlidou V., Papadakis I., et al., 2015, MNRAS, 453, 1669

Blinov D., Pavlidou V., Papadakis I., et al., 2018, MNRAS, 474, 1296

Bonning E., Urry C. M., Bailyn C., et al., 2012, ApJ, 756, 13

Böttcher M., 2002, Bulletin of the Astronomical Society of India, 30, 115

Böttcher M., Reimer A., 2004, ApJ, 609, 576

Böttcher M., Basu S., Joshi M., et al., 2007, ApJ, 670, 968

Böttcher M., Harris D., Krawczynski H., 2012, Relativistic Jets from Active Galactic Nuclei

Böttcher M., Reimer A., Sweeney K., et al., 2013, ApJ, 768, 54

Burbidge G. R., Jones T. W., Odell S. L., 1974, ApJ, 193, 43

Camenzind M., Krockenberger M., 1992, A&A, 255, 59

Carnerero M. I., Raiteri C. M., Villata M., et al., 2015, MNRAS, 450, 2677

Cawthorne T. V., Cobb W. K., 1990, ApJ, 350, 536

Chatterjee R., Jorstad S. G., Marscher A. P., et al., 2008, ApJ, 689, 79

Chatterjee R., Bailyn C. D., Bonning E. W., et al., 2012, ApJ, 749, 191

Chen X., Fossati G., Böttcher M., et al., 2012, MNRAS, 424, 789

Chevalier J., Sanchez D. A., Serpico P. D., et al., 2019, Monthly Notices of the Royal Astronomical Society, 484, 749

Condon J. J., 1997, PASP, 109, 166

Covino S., Sandrinelli A., Treves A., 2019, MNRAS, 482, 1270

Covino S., Landoni M., Sandrinelli A., et al., 2020, ApJ, 895, 122

D'Arcangelo F. D., Marscher A. P., Jorstad S. G., et al., 2009, ApJ, 697, 985

Dey L., Gopakumar A., Valtonen M., et al., 2019, Universe, 5, 108

Dominici T., Abraham Z., Pereyra A., Magalhães A., 2008, in Blazar Variability across the Electromagnetic Spectrum.

Doğan S., Nixon C., King A., Price D. J., 2015, MNRAS, 449, 1251

Dulwich F., Worrall D. M., Birkinshaw M., et al., 2009, MNRAS, 398, 1207

Edelson R., Nandra K., 1999, ApJ, 514, 682

Edelson R. A., Krolik J. H., Pike G. F., 1990, ApJ, 359, 86

Falomo R., Pesce J. E., Treves A., 1993, ApJ, 411, L63

Fan J. H., Lin R. G., 2000, A&A, 355, 880

Fang Y., Chen Q., Zhang Y., et al., 2022, ApJ, 933, 224

Foschini L., Ghisellini G., Tavecchio F., et al., 2007, ApJ, 657, L81

Foschini L., Treves A., Tavecchio F., et al., 2008, A&A, 484, L35

Fossati G., Maraschi L., Celotti A., et al., 1998, MNRAS, 299, 433

Fraija N., Benítez E., Hiriart D., et al., 2017, ApJS, 232, 7

Fuhrmann L., Angelakis E., Zensus J. A., et al., 2016, A&A, 596, A45

Gabuzda D. C., Chernetskii V. A., 2003, MNRAS, 339, 669

Gabuzda D. C., Pushkarev A. B., Cawthorne T. V., 2000, MNRAS, 319, 1109

Gaur H., Gupta A. C., Wiita P. J., et al., 2014, ApJ, 781, L4

Gaur H., Chen L., Misra R., et al., 2017, ApJ, 850, 209

Ghisellini G., Madau P., 1996, MNRAS, 280, 67

Ghisellini G., Tavecchio F., 2008, MNRAS, 386, L28

Ghisellini G., Tavecchio F., Chiaberge M., 2005, A&A, 432, 401

Gierliński M., Middleton M., Ward M., Done C., 2008, Nature, 455, 369

Giroletti M., Giovannini G., Feretti L., et al., 2004, ApJ, 600, 127

Gopal-Krishna Wiita P. J., 1992, A&A, 259, 109

Gupta A. C., Agarwal A., Mishra A., et al., 2017, MNRAS, 465, 4423

H. E. S. S. Collaboration Abramowski A., Acero F., Aharonian F., et al., 2011, A&A, 533, A110

H.E.S.S. Collaboration Aharonian F., Akhperjanian A. G., Aye K.-M., et al., 2005a, A&A, 430, 865

H.E.S.S. Collaboration Aharonian F., Akhperjanian A. G., Aye K.-M., et al., 2005b, A&A, 442, 895

H.E.S.S. Collaboration Aharonian F., Akhperjanian A. G., Bazer-Bachi A. R., et al., 2007, ApJ, 664, L71

H.E.S.S. Collaboration Aharonian F., Akhperjanian A. G., Anton G., et al., 2009a, A&A, 502, 749

H.E.S.S. Collaboration Aharonian F., Akhperjanian A. G., Anton G., et al., 2009b, ApJ, 696, L150

H.E.S.S. Collaboration Aharonian F., Akhperjanian A. G., Anton G., et al., 2009c, ApJ, 696, L150

H.E.S.S. Collaboration Abramowski A., Acero F., Aharonian F., et al., 2012, A&A, 539, A149

H.E.S.S. Collaboration Abramowski A., Aharonian F., Ait Benkhali F., et al., 2014, A&A, 571, A39

H.E.S.S. Collaboration Abdalla H., Abramowski A., Aharonian F., et al., 2017, A&A, 598, A39

Hagen-Thorn V. A., Marchenko S. G., 1999, Baltic Astronomy, 8, 575

Hagen-Thorn V. A., Larionova E. G., Jorstad S. G., et al., 2002, A&A, 385, 55

Hagen-Thorn V. A., Larionov V. M., Jorstad S. G., et al., 2008, ApJ, 672, 40

Holmes P. A., Brand P. W. J. L., Impey C. D., Williams P. M., 1984, MNRAS, 210, 961

Homan D. C., Lister M. L., 2006, AJ, 131, 1262

Hughes P. A., Miller L., 1991, Beams and Jets in Astrophysics

Hughes P. A., Aller H. D., Aller M. F., 1985, ApJ, 298, 301

Hughes P. A., Aller H. D., Aller M. F., 1992, ApJ, 396, 469

Hughes P. A., Aller M. F., Aller H. D., 2011, ApJ, 735, 81

Ikejiri Y., Uemura M., Sasada M., et al., 2011, , 63, 639

Jones T. W., 1988, ApJ, 332, 678

Jones T. W., Rudnick L., Aller H. D., et al., 1985, ApJ, 290, 627

Kamaram S. R., Prince R., Pramanick S., et al., 2023, MNRAS, 520, 2024

Kastendieck M. A., Ashley M. C. B., Horns D., 2011, A&A, 531, A123

Katarzyński K., Lenain J.-P., Zech A., Boisson C., Sol H., 2008, MNRAS, 390, 371

Kaur N., Chandra S., Baliyan K. S., et al., 2017, ApJ, 846, 158

Keivani A., Murase K., Petropoulou M., others 2018, ApJ, 864, 84

Kellermann K. I., Sramek R., Schmidt M., et al., 1989, AJ, 98, 1195

Kellermann K. I., Condon J. J., Kimball A. E., et al., 2016, ApJ, 831, 168

Kidger M., Takalo L., Sillanpaa A., 1992, A&A, 264, 32

Kiehlmann S., Savolainen T., Jorstad S. G., et al., 2016, A&A, 590, A10

King A. R., Pringle J. E., Hofmann J. A., 2008, MNRAS, 385, 1621

Koay J. Y., Jauncey D. L., Hovatta T., et al., 2019, MNRAS, 489, 5365

Krawczynski H., Hughes S. B., Horan D., et al., 2004, ApJ, 601, 151

Kushwaha P., Gupta A. C., Wiita P. J., et al., 2018, MNRAS, 473, 1145

Lachowicz P., Gupta A. C., Gaur H., et al., 2009, A&A, 506, L17

Lainela M., Valtaoja E., 1993, ApJ, 416, 485

Laing R. A., 1980, MNRAS, 193, 439

Larionov V. M., Jorstad S. G., Marscher A. P., et al., 2013, ApJ, 768, 40

Lister M. L., Homan D. C., 2005, AJ, 130, 1389

Lister M. L., Smith P. S., 2000, ApJ, 541, 66

Lister M. L., Marscher A. P., Gear W. K., 1998, ApJ, 504, 702

Lucchini M., Markoff S., Crumley P., et al., 2019, MNRAS, 482, 4798

Lyutikov M., Pariev V. I., Gabuzda D. C., 2005, MNRAS, 360, 869

MAGIC Collaboration Acciari V. A., Ansoldi S., Antonelli L. A., et al., 2020a, MNRAS, 496, 3912

MAGIC Collaboration Acciari V. A., Ansoldi S., Antonelli L. A., et al., 2020b, A&A, 638, A14

MAGIC Collaboration Acciari V. A., Aniello T., Ansoldi S., et al., 2023, A&A, 670, A49

Malkov M. A., Diamond P. H., Völk H. J., 2000, ApJ, 533, L171

Mannheim K., 1993, A&A, 269, 67

Marscher A. P., 2014, ApJ, 780, 87

Marscher A. P., Gear W. K., 1985, ApJ, 298, 114

Marscher A. P., Gear W. K., Travis J. P., 1992, in Valtaoja E., Valtonen M., eds, Variability of Blazars. p. 85

Marscher A. P., Jorstad S. G., Larionov V. M., et al., 2010, ApJ, 710, L126

Mattox J. R., et al., 1996, Astrophysical Journal, 461, 396

McKinney J., 2006, MNRAS, 368, 1561

Meier D. L., Nakamura M., 2006, in Miller H. R., Marshall K., Webb J. R., Aller M. F., eds, Astronomical Society of the Pacific Conference Series Vol. 350, Blazar Variability Workshop II: Entering the GLAST Era. p. 195

Meier D. L., Koide S., Uchida Y., 2001, Science, 291, 84

Mücke A., Protheroe R. J., 2001a, Astroparticle Physics, 15, 121

Mücke A., Protheroe R. J., 2001b, Astroparticle Physics, 15, 121

Mücke A., Protheroe R. J., Engel R., et al., 2003, Astroparticle Physics, 18, 593

Murgia M., et al., 2011, A&A, 526, A148

Narayan R., Piran T., 2012, MNRAS, 420, 604

Nixon C., King A., 2013, ApJ, 765, L7

Ojha R., Kadler M., Böck M., Booth R., et al., 2010, A&A, 519, A45

Pandey A., Rajput B., Stalin C. S., 2022, MNRAS, 510, 1809

Pasierb M., Goyal A., Ostrowski M., et al., 2020, MNRAS, 492, 1295

Patiño-Álvarez V. M., Fernandes S., Chavushyan V., et al., 2018, MNRAS, 479, 2037

Peceur N. W., Taylor A. R., Kraan-Korteweg R. C., 2020, Monthly Notices of the Royal Astronomical Society, 495, 2162

Pekeur N. W., Taylor A. R., Potter S. B., Kraan-Korteweg R. C., 2016, MNRAS, 462, L80

Pica A. J., Smith A. G., Webb J. R., Leacock R. J., Clements S., Gombola P. P., 1988, AJ, 96, 1215

Piner B. G., Edwards P. G., 2004, ApJ, 600, 115

Piner B. G., Pant N., Edwards P. G., 2008, ApJ, 678, 64

Piner B. G., Pant N., Edwards P. G., 2010, ApJ, 723, 1150

Pohl M., Schlickeiser R., 2000, A&A, 354, 395

Potter S. B., Buckley D. A. H., O'Donoghue D., et al., 2010, MNRAS, 402, 1161

Prince R., Agarwal A., Gupta N., et al., 2021, A&A, 654, A38

Prince R., Khatoon R., Majumdar P., et al., 2022, MNRAS, 515, 2633

Priya S., Prince R., Agarwal A., et al., 2022, MNRAS, 513, 2239

Qian S. J., Quirrenbach A., Witzel A., et al., 1991, A&A, 241, 15

Raiteri C. M., Villata M., Ibrahimov M. A., et al., 2005, A&A, 438, 39

Raiteri C. M., Villata M., Kadler M., et al., 2006, A&A, 459, 731

Raiteri C. M., et al., 2017, Nature, 552, 374

Rajput B., Stalin C. S., Sahayanathan S., et al., 2019, MNRAS, 486, 1781

Rajput B., Shah Z., Stalin C. S., et al., 2021, MNRAS, 504, 1772

Rajput B., Pandey A., Stalin C. S., et al., 2022, MNRAS, 517, 3236

Rani B., Gupta A. C., Joshi U. C., et al., 2010, ApJ, 719, L153

Rector T. A., Perlman E. S., 2003, AJ, 126, 47

Rees M. J., 1967, MNRAS, 135, 345

Rees M. J., 1971, Nature, 229, 312

Reynoso M. M., Romero G. E., Medina M. C., 2012, A&A, 545, A125

Rieger F. M., 2004, ApJ, 615, L5

Romero G. E., 1995, Ap&SS, 234, 49

Roy A., Gupta A. C., Chitnis V. R., et al., 2023, ApJS, 265, 14

Sahayanathan S., Godambe S., 2012, MNRAS, 419, 1660

Sandrinelli A., Covino S., Treves A., 2014, ApJ, 793, L1

Sandrinelli A., Covino S., Treves A., et al., 2017, A&A, 600, A132

Schmidt G. D., Stockman H. S., Smith P. S., 1992, Astrophysical Journal, Letters, 398, L57

Schuster A., 1898, Terrestrial Magnetism (Journal of Geophysical Research), 3, 124

Schutte H. M., Britto R. J., Böttcher M., et al., 2022, ApJ, 925, 139

Siejkowski H., Wierzcholska A., 2017, MNRAS, 468, 426

Sikora M., Begelman M. C., Rees M. J., 1994, ApJ, 421, 153

Sikora M., Błażejowski M., Moderski R., et al., 2002, ApJ, 577, 78

Sillanpaa A., Haarala S., Valtonen M. J., et al., 1988, ApJ, 325, 628

Sillanpaa A., Takalo L. O., Pursimo T., et al., 1996, A&A, 305, L17

Singh K. K., Meintjes P. J., Bisschoff B., et al., 2020, Journal of High Energy Astrophysics, 26, 65

Sivron R., 1998, ApJ, 503, L57

Smith P. S., Hall P. B., Allen R. G., et al., 1992, The Astrophysical Journal, 400, 115

Smith P. S., Montiel E., Rightley S., et al., 2009, Coordinated Fermi/Optical Monitoring of Blazars and the Great 2009 September Gamma-ray Flare of 3C 454.3 (`arXiv:0912.3621`)

Sorcia M., Benítez E., Hiriart D., et al., 2013, ApJS, 206, 11

Stevens J., Edwards P. G., Ojha R., et al., 2012, preprint (`arXiv:1205.2403`)

Stroh M. C., Falcone A. D., 2013, ApJS, 207, 28

Strong A. W., Moskalenko I. V., Reimer O., Digel S., Diehl R., 2004a, A&A, 422, L47

Strong A. W., Moskalenko I. V., Reimer O., 2004b, ApJ, 613, 962

Timmer J., Koenig M., 1995, A&A, 300, 707

Tommasi L., et al., 2001, A&A, 376, 51

Urry C. M., Padovani P., 1995a, PASP, 107, 803

Urry C. M., Padovani P., 1995b, PASP, 107, 803

Urry C. M., Maraschi L., Edelson R., et al., 1993, ApJ, 411, 614

Urry C. M., Treves A., Maraschi L., et al., 1997, ApJ, 486, 799

Valtaoja L., Sillanpaa A., Valtaoja E., Shakhovskoi N. M., Efimov I. S., 1991, AJ, 101, 78

Valtonen M. J., Nilsson K., Sillanpää A., et al., 2006, ApJ, 643, L9

Vaughan S., 2005, A&A, 431, 391

Vaughan S., Edelson R., Warwick R. S., et al., 2003, MNRAS, 345, 1271

Vlahakis N., Königl A., 2004, in Richards G. T., Hall P. B., eds, Astronomical Society of the Pacific Conference Series Vol. 311, AGN Physics with the Sloan Digital Sky Survey. p. 151

Wierzcholska A., Zacharias M., Jankowsky F., Wagner S., H. E. S. S. Collaboration 2019, Galaxies, 7, 21

Zhang B.-K., Zhao X.-Y., Wang C.-X., et al., 2014, Res. Astron. & Astrophys., 14, 933

Zhang P.-f., Yan D.-h., Liao N.-h., et al., 2017, ApJ, 835, 260

Zhang B.-K., Jin M., Zhao X.-Y., et al., 2021, Research in Astronomy and Astrophysics, 21, 186